



저작자표시-비영리-변경금지 2.0 대한민국

이용자는 아래의 조건을 따르는 경우에 한하여 자유롭게

- 이 저작물을 복제, 배포, 전송, 전시, 공연 및 방송할 수 있습니다.

다음과 같은 조건을 따라야 합니다:



저작자표시. 귀하는 원저작자를 표시하여야 합니다.



비영리. 귀하는 이 저작물을 영리 목적으로 이용할 수 없습니다.



변경금지. 귀하는 이 저작물을 개작, 변형 또는 가공할 수 없습니다.

- 귀하는, 이 저작물의 재이용이나 배포의 경우, 이 저작물에 적용된 이용허락조건을 명확하게 나타내어야 합니다.
- 저작권자로부터 별도의 허가를 받으면 이러한 조건들은 적용되지 않습니다.

저작권법에 따른 이용자의 권리는 위의 내용에 의하여 영향을 받지 않습니다.

이것은 [이용허락규약\(Legal Code\)](#)을 이해하기 쉽게 요약한 것입니다.

[Disclaimer](#)

공학박사 학위논문

높은 험지 극복 성능과 조종성을 위한
네 개의 틸팅 트랙을 갖는 험지 주행 로봇

A Mobile Robot with Tilting Quad-tracks for
High Terrainability and Maneuverability on
Rough Terrain

2018년 8월

서울대학교 대학원
기계항공공학부

김 지 훈

높은 험지 극복 성능과 조종성을 위한 네 개의 틸팅 트랙을 갖는 험지 주행 로봇

A Mobile Robot with Tilting Quad-tracks for
High Terrainability and Maneuverability on
Rough Terrain

지도 교수 김 종 원

이 논문을 공학박사 학위논문으로 제출함
2018 년 4 월

서울대학교 대학원
기계항공공학부
김 지 훈

김지훈의 공학박사 학위논문을 인준함
2018 년 6 월

위 원 장 박 희 재 (인)

부위원장 김 종 원 (인)

위 원 안 성 훈 (인)

위 원 차 석 원 (인)

위 원 이 동 훈 (인)

Abstract

This paper is about the development of PATRo (Passively Articulated Tracked Mobile Robot) which is a new mobile robot mechanism for rough terrain driving. PATRo mechanism consists of four drive tracks, two rocker links, and a main body. The rockers are connected to the main body via a differential joint, and each drive track is connected to the rocker via 2 degrees-of-freedom (DOF) passive joints. Thus, with 9 DOFs in total, the four drive tracks can be independently positioned and oriented to maximize the contact area with the ground on a random ground shape. There are two main advantages of the proposed PATRo mechanism. First, the loss of traction force due to imperfect contact is minimized by securing the contact area between the track and the ground. Second, it is possible to know the ground contact angle of each four drive tracks on the ground without prior information, and it is possible to observe the terrain around the robot. And the surrounding terrain information can be used in the rough terrain driving control to improve the reference trajectory tracking performance.

Therefore, PATRo is a new mobile robot platform with improved maneuverability which is the disadvantage of the conventional track-typed mobile robots, and improved terrainability which is the disadvantage of the conventional wheeled mobile robots. In this study, rough terrain driving performance of PATRo was confirmed by both simulation and experiment. First, through 3D dynamics simulation, driving performance of PATRo is compared to those of seven existing mobile robot mechanisms. The same control algorithm was applied to verify only the influence of the mechanical characteristics of each platform purely, and the comparison test was repeated in the three different driving environments to prevent the biased result by selecting the driving environment. As a result, the PATRo platform showed the most superior performances in both terrainability and maneuverability among the total of 8 platforms. Compared to seven other platforms, PATRo showed

25.5% improved terrainability and 44.7% improved maneuverability, in average.

Also, the design parameter optimization of the PATRo platform was performed. In order to improve the terrainability and maneuverability at the same time, the objective function of optimization was selected as the maximum value of the required friction coefficient. The length of the rocker and the length of the drive track were selected as the design variables through the sensitivity analysis using the orthogonal array and level average analysis. The optimal torque distribution based on kinetostatic analysis was used to calculate the required friction coefficient during the optimization process. Taguchi methodology is used for the optimization. Based on the initial and optimal values of the design variables, the rockers and drive tracks of the PATRo prototype were each produced in two versions.

There are mainly four issues to be validated through rough terrain driving experiment of PATRo prototype. The first is the relative superiority compared to the existing mobile robots, which were confirmed through simulation. In the experiment, this can be confirmed by comparing the driving performance of PATRo when the nine passive joints are fixed, and when they are not. Second is to verify the effect of the proposed PATRo kinematic model. The third is the verification of the design parameter optimization results. Experimental results show that the terrainability and maneuverability are improved by 10.1% and 26.8%, respectively. Finally, rough terrain driving experiment in the real circumstance is carried out and the result proved the effectiveness of the mechanism.

Keyword : mobile robot, locomotion mechanism, design optimization, rough terrain, kinetostatic analysis, terrainability, maneuverability

Student Number : 2012-20659

Table of Contents

Chapter 1. Introduction	1
1.1 Motivation.....	1
1.2 Performance indices for mobile robot mechanisms.....	3
1.2.1 Terrainability	5
1.2.2 Maneuverability.....	5
1.2.3 Test terrain: unsymmetric wavy bump	6
1.3 Research objective and scope.....	8
Chapter 2. New mobile robot mechanism PATRo	10
2.1 Mechanical configuration of PATRo	10
2.2 Order of DOFs in the passive joints	12
2.3 Shape of drive tracks.....	14
2.4 Other mechanical features of PATRo	14
Chapter 3. Performance verification of PATRo by dynamics simulation ...	15
3.1 Various locomotion mechanisms to be compared.....	15
3.2 Rough terrain driving scenarios.....	17
3.3 Simulation configuration	19
3.4 Simulation results and discussions	22
3.4.1 Comparison of mechanisms A and B: effect of pitch-roll 2-DOF passive joints on TA and MA	23
3.4.2 Comparison of mechanisms A and C: effect of 1-DOF for rocker pitching on TA and MA	24
3.4.3 Comparison of PATRo and all wheeled platforms.....	25
3.4.4 Overall simulation results	27
Chapter 4. Mobile robot kinematics	30
4.1 Necessity of PATRo kinematic model	30
4.2 Mobile robot kinematics of PATRo.....	30
4.3 Verification through dynamics simulation	32
Chapter 5. Optimal design of PATRo based on kinetostatic analysis	34
5.1 Previous researches for optimal design of mobile robots	34
5.2 Optimization problem definition	35
5.2.1 Cascaded optimization problem definition	35
5.2.2 Objective function: required friction coefficient.....	37
5.2.3 Design variables.....	38
5.2.3.1 Design variables: PATRo dimension parameters	38
5.2.3.2 Need for optimal torque distribution.....	39
5.3 Kinetostatic analysis of PATRo	40

5.3.1 Kinematic synthesis of PATRo for kinetostatic analysis.....	40
5.3.1.1 Generation of pointwise contour of driving track and test terrain	41
5.3.1.2 2D trajectory generation of a single track	42
5.3.1.3 2D trajectory generation of the half-PATRo.....	44
5.3.1.4 3D trajectory generation of the full PATRo	45
5.3.2 Kinetostatic analysis and optimal torque distribution.....	48
5.3.2.1 Force and moment equilibrium equations for PATRo	48
5.3.2.2 Optimal torque distribution.....	51
5.4 Design parameter optimization	52
5.4.1 Sensitivity analysis	52
5.4.2 Design parameter optimization based on Taguchi methodology.....	54
5.4.3 Verification of the optimization result.....	57
Chapter 6. Manufacturing of PATRo prototype	61
6.1 Mechanical configuration of PATRo	61
6.1.1 Driving tracks.....	61
6.1.2 2-DOF passive joints	62
6.1.3 Rocker links with differential joint	63
6.1.4 Lidar module for PATRo localization	63
6.1.5 Control box and battery.....	64
6.2 Electrical configuration of PATRo and operation software.....	65
Chapter 7. Experiment and result.....	67
7.1 Experimental setup	67
7.1.1 Fabrication of unsymmetric wavy bump	67
7.1.2 Localization based on 2D Lidar module and the walls.....	68
7.1.2.1. 2-DOF 2D Lidar module for orientation stabilization.....	69
7.1.2.2. PATRo localization algorithm.....	76
7.2 Experimental results.....	78
7.2.1 Reference posture tracking control on the rough terrain.....	78
7.2.2 Effect of passive joints: PATRo vs partially locked PATRo	80
7.2.3 Effect of passive joints: applying PATRo kinematics vs applying planar kinematics	82
7.2.4 Effect of design parameter optimization: initial design vs optimal design of PATRo.....	83
7.2.5 Field test on mountainous rough terrain.....	84
Chapter 8. Conclusion	86
Bibliography	88
Abstract in Korean.....	90

List of the Tables

Table 1.1 Three general types of locomotion mechanisms for rough terrain mobile robots	1
Table 1.2 Actively articulated tracks in previous works	2
Table 1.3 Evaluation methods for performance indices	4
Table 3.1 Mass and dimensions for various locomotion mechanisms in simulation environment	17
Table 3.2 Configurations of three scenarios: shape of reference trajectory, reference velocity, and simulation time.....	19
Table 3.3 Contact conditions for tracked vehicles in simulation	21
Table 3.4 Values of TA and MA of all mechanisms in three scenarios ...	29
Table 5.1 Descriptions for design variables.....	39
Table 5.2 Two cases of torque distribution at the same state	40
Table 5.3 Result of sensitivity analysis.....	47
Table 5.4 Result of design optimization.....	50
Table 7.1 Articulation structure of the four platforms.....	80
Table 7.2 Terrainability and maneuverability values of the four platforms	81

List of the Figures

Fig. 1.1 Test terrains used in previous research: (a) step obstacle [23], (b) random rough terrain [24], (c) Martian terrain model [25] ..	6
Fig. 1.2 Specification of the standard rough terrain: unsymmetric wavy bump	7
Fig. 1.3 Profiles of the reference linear velocity and angular velocity.....	8
Fig. 2.1 Design inspiration for the new mechanism: The orientations of the feet of a human keep changing according to the shape of the terrain.....	10
Fig. 2.2 Mechanical configuration of PATRo mechanism.....	11
Fig. 2.3 PATRo mechanism: (a) manufactured prototype, (b) track adaptation by passive pitching, (c) track adaptation by passive rolling	12
Fig. 2.4 Comparison of order of placement of passive revolute joints: (a) pitch–pitch–roll, (b) pitch–roll–pitch	13
Fig. 2.5 Comparison of flat track and triangular shaped track when encountering a step obstacle.....	14
Fig. 3.1 Various subject locomotion mechanisms to be evaluated and compared: (a) PATRO, (b) articulated quad–tracks with rockers, (c) articulated quad–tracks with passive 2–DOF joints, (d) articulated quad–tracks with central pitch joint (with Robhaz [23]), (e) non–articulated quad–tracks (with Packbot [7]), (f) rocker–bogie (with Curiosity [1–4]), (g) CRAB [12], (h) RCL–E [12]	15
Fig. 3.2 Unification of kinematic parameters of mobile robots.....	16
Fig. 3.3 Test terrain and reference velocity in three scenarios: dimensions of terrain model in (a) scenario 1, (b) scenario 2, and (c) scenario 3; reference linear and angular velocities in (d) scenario 1, (e) scenario 2, and (f) scenario 3.....	18
Fig. 3.4 Block diagram of overall simulation architecture based on MATLAB/Simulink and DAFUL	19
Fig. 3.5 Description on the reference posture, current posture, and error posture	20
Fig. 3.6 Mechanical structure of driving tracks in simulation environment	21
Fig. 3.7 Snapshot of dynamics simulation (PATRO on scenario 1)	22
Fig. 3.8 Comparison of mechanisms A and B: (a) standard deviation of ground reaction forces of four tracks, (b) total required torque, and (c) trajectory tracking error (in driving scenario 1)	23
Fig. 3.9 Snapshot of dynamics simulation when a track of mechanism C is tilted unnaturally in (a) scenario 1 and (b) scenario 2	24
Fig. 3.10 Comparison of pitch angle profiles of four tracks in mechanism A	

and C on scenario 1: (a) front left track, (b) front right track, (c) rear left track, (d) rear right track.....	25
Fig. 3.11 Comparison of contact under the same conditions: (a) surface contact of mechanism A, (b) edge contact of mechanism B, (c) point contact of mechanism F	25
Fig. 3.12 (a) trajectory tracking error of mechanisms A, B, F, G, and H, (b) time derivative of longitudinal error, (c) ground slope of the terrain model (all in scenario 1)	26
Fig. 3.13 Comparison of eight mobile robot mechanisms on TA–MA plane, in (a) driving scenario 1, (b) driving scenario 2, and (c) driving scenario 3	28
Fig. 3.14 Raw data profiles of simulation results: (a) TA in scenarios 1, (b) TA in scenario 2, (c) TA in scenario 3, (d) MA in scenarios 1, (e) MA in scenario 2, (f) MA in scenario 3.....	28
Fig. 4.1 Mobile robot kinematic analysis: (a) velocity of the driving track, (b) coordinate frames and axes of rotation for kinematic analysis	31
Fig. 4.2 Verification of the proposed PATRo kinematics through dynamics simulation	33
Fig. 5.1 Overall configuration for the cascaded optimization problem	36
Fig. 5.2 Normal forces and traction forces acting on four drive tracks...	38
Fig. 5.3 Design variables of PATRo mechanism for design optimization	39
Fig. 5.4 Pointwise contour of a drive track	41
Fig. 5.5 Pointwise contour of the test terrain	41
Fig. 5.6 2D trajectory generation of a single track.....	43
Fig. 5.7 2D trajectory of the half–PATRo model	44
Fig. 5.8 3D trajectory of the full PATRo model.....	45
Fig. 5.9 Comparison of PATRo orientation between 3D dynamics simulation result (DAFUL) and kinematic synthesis result (MATLAB)	46
Fig. 5.10 Comparison of PATRo configuration between 3D dynamics simulation result (DAFUL) and kinematic synthesis result (MATLAB)	47
Fig. 5.11 Forces acting on the links of PATRo	48
Fig. 5.12 Free body diagram of half–PATRo model (left)	49
Fig. 5.13 Example of a result of optimal torque distribution (at initial values of design variables)	52
Fig. 5.14 Sensitivity analysis of the design variables	53
Fig. 5.15 Change of slip ratio profile according to the change of x_1	54
Fig. 5.16 Moments when the peak slip ratio occurs	55
Fig. 5.17 Results of three times of Taguchi optimization	56

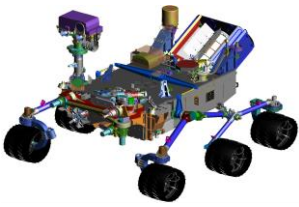
Fig. 5.18	Verification of optimization results using dynamics simulation	57
Fig. 5.19	Change of terrainability before and after optimization	58
Fig. 5.20	Change of maneuverability before and after optimization	59
Fig. 5.21	Initial and optimal versions of PATRo prototype	60
Fig. 6.1	Mechanical configuration of PATRo prototype	61
Fig. 6.2	Track assemblies in the PATRo prototype	62
Fig. 6.3	2-DOF passive joint in the PATRo prototype	62
Fig. 6.4	Rockers and differential joint in PATRo prototype	63
Fig. 6.5	(a) Lidar module in the PATRo prototype, (b) orientation stabilization of the Lidar module	64
Fig. 6.6	(a) Control box and (b) battery in the PATRo prototype	64
Fig. 6.7	Electrical configuration of the PATRo prototype	66
Fig. 6.8	Control front panel and user interface of PATRo	66
Fig. 7.1	Experimental setup	67
Fig. 7.2	Fabrication process of the unsymmetric wavy bump	67
Fig. 7.3	Overall system configuration for the experimental methods of the evaluation	68
Fig. 7.4	Mechanical structure of the 2-DOF Lidar module and the coordinate frames, orientation matrices assigned to the system	70
Fig. 7.5	Block diagram for the Lidar orientation control	75
Fig. 7.6	Flow chart of the platform localization process	76
Fig. 7.7	Snapshot of reference posture tracking control experiment of PATRo	78
Fig. 7.8	Result of experiment: (a) terrainability, (b) maneuverability, (c) angular position of passive joints	79
Fig. 7.9	Reproducibility of the terrainability and maneuverability	79
Fig. 7.10	Comparison of experimental result and simulation result in the same condition	80
Fig. 7.11	Raw data of experiments for validation of effect of PATRo articulation	81
Fig. 7.12	Terrainability–maneuverability 2D plot: effect of PATRo articulation	81
Fig. 7.13	Comparison of maneuverability: using planar kinematics vs PATRo kinematics	82
Fig. 7.14	Specification of PATRo platforms: initial design and optimal design	83
Fig. 7.15	Raw data of experiments for validation of effect of design optimization	83
Fig. 7.16	Various rough terrain features in the experiment site	84
Fig. 7.17	PATRo overcoming various obstacles during rough terrain driving	85

Chapter 1. Introduction

1.1 Motivation

The ability to overcome obstacles and navigating on rough terrain is one of the important core technologies for mobile robots in various fields such as planetary exploration [1–4], military [5–7], disaster relief [8–9], etc. Unlike mobile robots for flat ground, rough terrain mobile robots require higher performance in various aspects such as overcoming obstacles and avoiding obstacles, posture stability on poor road surface, maintaining straightness and steerability in irregular situations, etc. Therefore, various studies have been carried out on mobile robot mechanism to improve mobility on rough terrain. These studies can be classified into three groups, as shown in Table 1.1: wheel–linkage type [1–4], tracked type [7–8], and legged type [5,9].

Table 1.1 Three general types of locomotion mechanisms for rough terrain mobile robots

Wheel–linkage type	Tracked type	Legged type
		
Curiosity (2011), NASA	Packbot (2004), iRobot	LS3 (2012), Boston Dynamics

The wheel–linkage type mechanism is the basic option for rough terrain mobile robots due to its structural simplicity; various mechanisms have been studied such as rocker–bogie [2,10,11], CRAB [12], RCL–E [13], etc. The legged type locomotion mechanism shows superior performance on overcoming obstacles based on advanced intelligence and control technology. The legged type locomotion mechanism has recently been rapidly developed, including a series of quadruped robotic platforms by Boston

Dynamics [5].

On the other hand, compared to the wheeled and legged platforms, the tracked type mobile robots are well-known to be advantageous as they constantly produce enough tractive power, negotiating diverse forms of discrete obstacles such as wider gaps or higher steps [14], and have better floatation and traction on loose soil [15].

However, in the case of a terrain with more severe curvature, (such as when the size of the track is relatively large compared to the curvature of the ground), only part of the bottom surface of the track is able to come into contact with the ground and the other large part of the track may not. This leads to a limitation in the rough terrain driving of the mobile robot. First, incomplete contact between the driving track and the ground reduces the transfer efficiency of the motor traction, and increases the amount of energy required to travel the same distance. Second, incomplete contact renders the direction of the traction force unstable, which may cause an error between the desired trajectory and the actual trajectory of the mobile robot.

Table 1.2 Actively articulated tracks in previous works

		
<p>Chaos, Lewis et al. [16]</p>	<p>Kenaf, Ohno et al. [17]</p>	<p>Packbot, iRobot [7]</p>

In order to overcome this, researchers have presented articulated tracks in various configurations; instead of using two large tracks, they combined several small tracks and controlled the posture of each track to achieve stable contact on irregular ground. As shown in Table 1.2, Lewis et al. controlled the pitch angle of each of the four driving tracks independently to overcome more

difficult obstacles [16]. Similarly, Ohno et al. controlled the pitch angle of four of the six driving tracks [17], and iRobot’s Packbot added two smaller pitch-controlled driving tracks in front of the two existing driving tracks [7].

However, the above-mentioned mobile robots [7,16,17] have *actively* articulated tracks. In order to utilize these tracks, in addition to the driving motors, additional motors for track pitch control are required. Also, in order to control the track configuration properly, information on the surrounding environment and appropriate control strategies are required; otherwise, the operator should directly control the track configuration in real time.

Therefore, this paper presents a new rough terrain locomotion mechanism with *passively* articulated tracks in which the orientation of the track independently adapts according to the ground shape. The new mechanism has four driving tracks, each of which can adapt to the terrain by a rocker link and a 2-degrees-of-freedom (2-DOF) pitch-roll passive joint, ensuring maximum contact with the irregular terrain without additional actuators.

1.2 Performance indices for mobile robot mechanisms

It is always controversial to quantitatively evaluate a rough terrain mobile robot mechanism, because the ‘rough terrain’ inevitably requires irregularity or randomness and is hard to be specified. Generally, the performance evaluation of mobile robots in the most previous research, is based on terrainability (TA), maneuverability (MA), and trafficability, as proposed by D. Apostopoulos [18]. The three performance indices in the literature is listed in Table 1.3.

Table 1.3 Evaluation methods for performance indices

Terrainability	Maneuverability	Trafficability
Torque/power for downhill/crosshill grade negotiation	Turning radius	Drawbar pull
Torque/power for discrete obstacle negotiation	Steering resolution	Sinkage ground pressure
Tipover/rollover resistance	Lateral resistance	Immobilization resistance
Wedging avoidance	Steering geometry	Motion resistance

First, TA refers to the ability to negotiate rough terrain features without compromising the stability and forward progress of the robot. According to the purpose and characteristics of mobile robot performance evaluation in each study, TA can be quantified according to various indices such as maximum gradeable slope, required friction force and torque, static stability and tipover stability. Second, MA is a performance index that addresses the ability to navigate through an environment, and can be quantified by various indices such as turning radius, tracking error, etc. Lastly, based on Bekker’s theory [20], trafficability is the ability to generate traction and move the robot, assuming deformable ground and deformable wheels.

In this study, we evaluated various locomotion mechanisms with two performance indices of TA measured from the magnitude of the required torque, and MA measured from the magnitude of the trajectory tracking error. Among the three general indicators proposed in [18], trafficability is excluded because it is mainly used for wheel shape design and actuator selection, rather than the evaluation of locomotion mechanisms [21–22]; and also mainly used in the Mars rover study where influence of soil deformation is not negligible.

1.2.1 Terrainability

In this study, TA is measured as the required torque when driving on a given trajectory on a given rough terrain, and can be expressed as follows.

$$TA = \sum_{j=1}^M \sqrt{\frac{1}{N} \sum_{i=1}^N (\tau_{req,j}(i))^2} \quad (1.1)$$

where $\tau_{req,j}(i)$ denotes the required torque of the j -th driving motor in the i -th simulation step. N is the number of total simulation steps and M is the number of driving motors. For example, M is 4 for the PATRo mechanism and M is 6 for the rocker-bogie mechanism. Therefore, the TA value is the sum of the root-mean-square (RMS) values of the required torque of each driving motor.

As the value of TA decreases, the locomotion mechanism improves. This is because the less torque needed to travel the same terrain means that the mobile robot can have a larger payload and can run on slippery surfaces; also a smaller drive motor can be selected and better energy efficiency and longer operation time can be achieved.

1.2.2 Maneuverability

MA in this study was measured as the magnitude of the trajectory tracking error that occurs during the running of the given trajectory on a given terrain, and can be expressed as follows.

$$MA = \sqrt{\frac{1}{N} \sum_{i=1}^N \left(\{x(i) - x_{des}(i)\}^2 + \{y(i) - y_{des}(i)\}^2 \right)} \quad (1.2)$$

where $x(i)$ and $y(i)$ are the current position of the robot, and $x_{des}(i)$ and $y_{des}(i)$ are the desired position. Therefore, the MA value is the RMS value of the distance error between the desired position and the current position. Similar to TA, as MA value decreases, the rough terrain locomotion mechanism improves. This is because,

since the robot is better able to follow a given trajectory on an irregular terrain, it can be used for a greater number of applications that require high positional accuracy.

1.2.3 Test terrain: unsymmetric wavy bump

The above terrainability and maneuverability are determined by not only the mechanical characteristics of the mobile robots but also the experimental conditions. Here, the experimental conditions include the shape of the terrain, the shape of the reference trajectory, and the traveling speed of the robot. Therefore, it is necessary to select representative conditions that can evaluate the rough terrain driving performance of the mobile robot mechanism. For example, Thueer et al. used a step obstacle with a height equal to the diameter of the wheel as a test terrain to evaluate the performance of the rocker-bogie mechanism [23], Krebs et al. used a random terrain as shown in Figure 1.1 (a) for torque control of CRAB mechanism [24], and Ellery et al. used a real Martian terrain model to evaluate the mobility of the planetary rover [25].

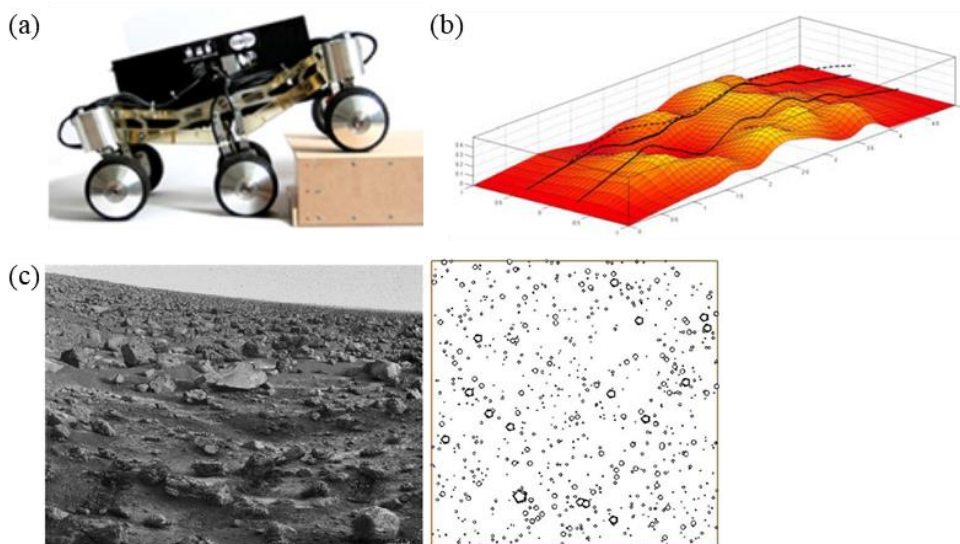


Fig. 1.1 Test terrains used in previous research: (a) step obstacle [23], (b) random rough terrain [24], (c) Martian terrain model [25]

In this study, an unsymmetric wavy bump in Fig. 1.1 was used as a test terrain to evaluate terrainability and maneuverability. This unsymmetric wavy bump has been used for kinematics modeling and analysis of articulated rovers in a study by Tarokh et al. [26]. As shown in Fig. 1.2, the running speed is set to 0.4 m/s, and the total running time and acceleration/deceleration time are 12 sec and 1.5 sec, respectively, and the total length of the reference trajectory is 4.2 m. Since the height and slope of the ground along which the four drive tracks (or drive wheels) pass while continuously driving the unsymmetric wavy bump change continuously, the terrain is selected as a representative test terrain in the development of a new rough terrain mobile robot in this study.

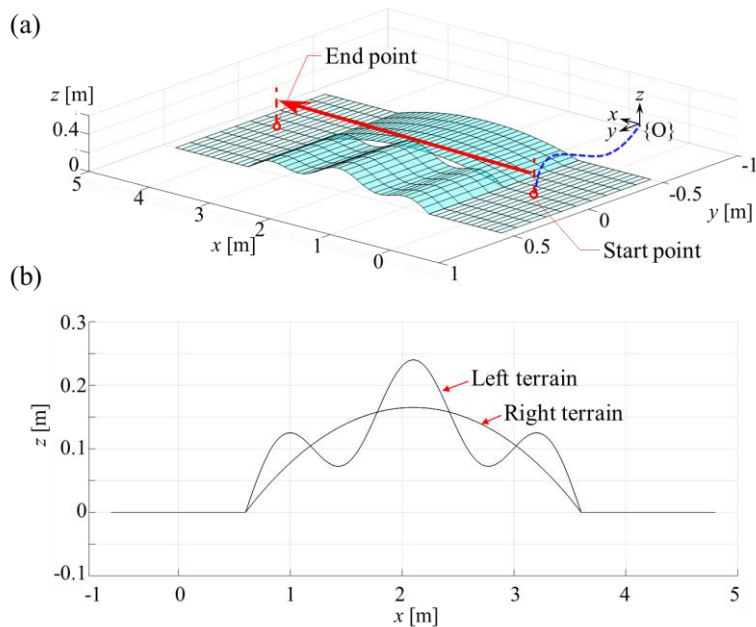


Fig. 1.2 Specification of the standard rough terrain: unsymmetric wavy bump

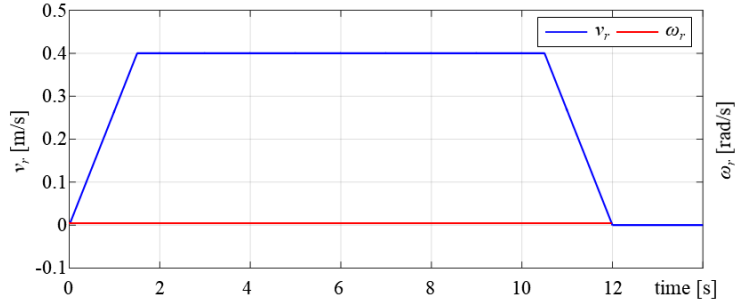


Fig. 1.3 Profiles of the reference linear velocity and angular velocity

This evaluation method can be used in the process of developing a mobile robot platform, both in conceptual design process and detailed design process. In the conceptual design stage, it can be used to compare the locomotion mechanism of the robot with other mechanisms, and to analyze the pros and cons and the characteristics of the mechanism. In the detailed design stage, it can be used to measure the performance in every design iteration step in the process of design optimization.

1.3 Research objective and scope

This paper is about the development of a new mobile platform PATRo (which will be introduced in the next chapter). The proposed PATRo mechanism has superior terrainability and maneuverability compared to other mobile robot mechanisms. Thus, the goal of this study is to demonstrate the rough terrain driving performance of the proposed PATRo mechanism, and this research goal can be divided into mainly two sub-objectives. The first goal is to identify and analyze the performance of the proposed PATRo mechanism, relative to other hull driving. This can be confirmed by creating various rough terrain mobile robot models in 3d dynamics simulation environment and comparing the driving performance. In addition, the performance of some mobile robots is compared through actual experiments. The second goal is to perform the design optimization to improve the performance of the PATRo, and

to verify the optimization results through experiments. In addition, kinetostatic analysis of the PATRo mechanism was performed to calculate the performance at various design variables in the optimization process, and PATRo localization using the Lidar sensor was implemented for the reference trajectory tracking experiment.

The remaining paper is organized as follows. Chapter 2 introduces the mechanism of PATRo and explains the process of deriving the mechanism. In Chapter 3, PATRo platform is compared to the existing rough terrain driving platforms, and the result is discussed. Chapter 4 explains the kinematic and kinetostatic synthesis of PATRo on test terrain for optimal design of PATRo, and performs design parameter optimization using Taguchi methodology. Chapter 5 explains the fabrication of the PATRo prototype, and Chapter 6 discusses the experimental results. Finally, the conclusions are presented in Chapter 7.

Chapter 2. New mobile robot mechanism PATRo

2.1 Mechanical configuration of PATRo

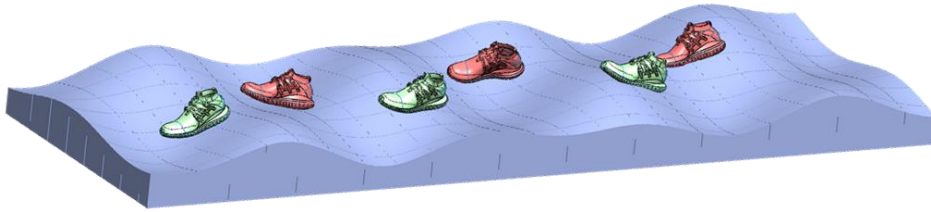


Fig. 2.1 Design inspiration for the new mechanism: The orientations of the feet of a human keep changing according to the shape of the terrain

As a design inspiration of new locomotion mechanism, we would like to talk about the case of humans. When human is walking on a rough terrain, the orientation of the feet always change according to the irregular ground shape, as in the Fig. 2.1. There are two reasons why orientations of the feet keep changing. First is to make the person stand well on the ground. Second is to generate reaction force in the right direction to propel the person in the desired direction. If feet orientations are constant (i.e. if human does not have ankle joints), then the feet would not make good contact to the ground. Then the person needs more power to walk, because the redundancy of the body system is reduced, and the torque cannot be distributed well. Also, if ankles are fixed, it gets hard to walk in desired direction. This example became a strong hint for achieving the research goal, which was developing a new locomotion mechanism with smaller torque and smaller tracking error on rough terrain.

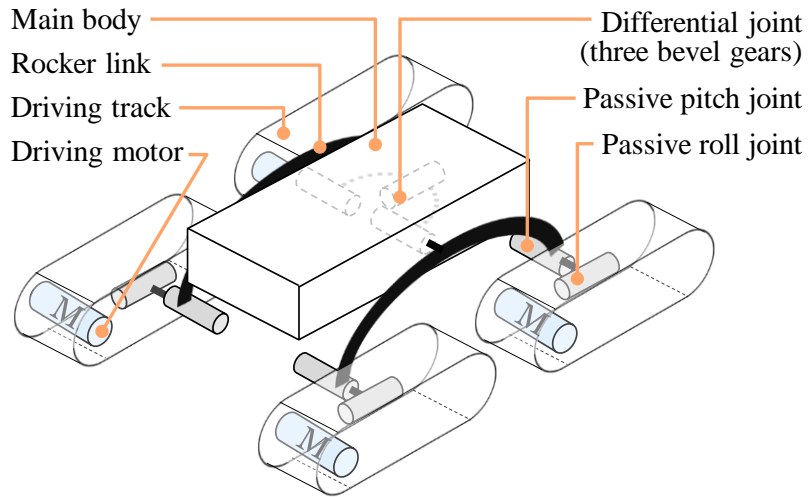


Fig. 2.2 Mechanical configuration of PATRo mechanism

As shown in Fig. 2.2, the PATRo mechanism consists of four driving tracks, two rocker links to which the tracks are connected, and a main body to which the rockers are connected. Each track is provided with an actuator for driving torque generation, and the tracks are connected to the rockers via passive joints of pitch–roll 2–DOF. Fig. 2.3(a) shows the prototype of the PATRo mechanism. As shown in Figs. 2.3(b) and 2.3(c), the passive joint structure and rockers allow the posture of the track to adapt to the terrain and to ensure a large contact area at all times. This is especially advantageous as any additional actuators, sensors, or control algorithms are not required. Although the passively articulated tracked mechanism itself is not entirely new, a mechanism having both the ‘2–DOF passive joints in each driving track’ and the ‘rocker DOF’ has not been proposed yet.

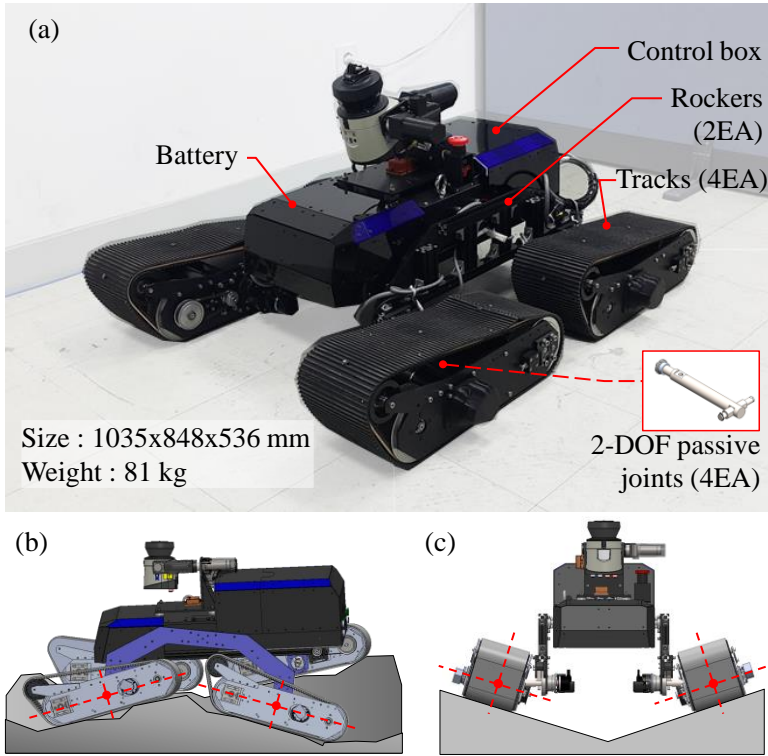


Fig. 2.3 PATRo mechanism: (a) manufactured prototype, (b) track adaptation by passive pitching, (c) track adaptation by passive rolling

2.2 Order of DOFs in the passive joints

The 2-DOF passive joint of each track is connected to the main body in the order of pitch- roll , not in the order of roll-pitch. Thus, the heading direction of the track can always stay inside the sagittal plane of the main body ($x_B z_B$ -plane in Fig. 2.4), regardless of the kinematic configuration. The kinematic structure of each case is compared in Fig. 2.4. $\{B\}$ is the coordinate frame attached to the main body of the robot platform; $\{T_a\}$ and $\{T_b\}$ are the coordinate frames attached to the track in the two cases. Since the rocker link rotates along the y -axis of the robot body (y_B), the PATRo structure can be considered as four kinematic chains of pitch-pitch- roll (Fig. 2.4(a)) or pitch- roll -pitch (Fig. 2.4(b)), both starting from $\{B\}$. Here, the end-effector of the kinematic chain is attached to each driving track. The notable difference between the

two cases is the direction of the traction force generated by the track. Since the axis of the driving motor is aligned with the y -axis of each track (y_{Ta} or y_{Tb}), the direction of the traction force becomes x_{Ta} or x_{Tb} . Through the kinematic analysis of the product-of-exponential (POE) model [19], x_{Ta} and x_{Tb} expressed in $\{B\}$ are expressed by Eqs. (1) and (2), respectively.

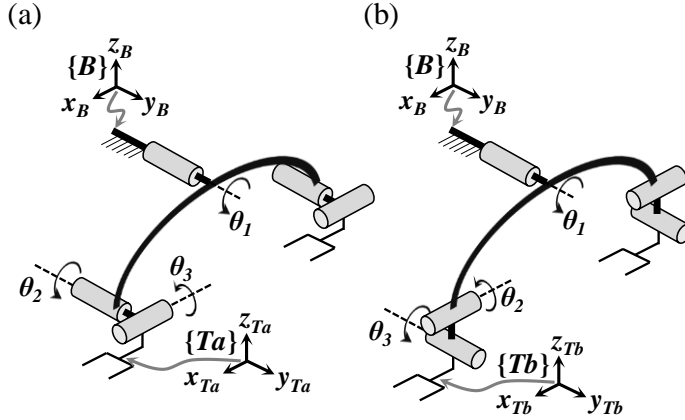


Fig. 2.4 Comparison of order of placement of passive revolute joints: (a) pitch-pitch-roll, (b) pitch-roll-pitch

$$x_{Ta}^B = (e^{\hat{y}\theta_1} e^{\hat{y}\theta_2} e^{\hat{x}\theta_3}) [1 \ 0 \ 0]^T = [c_{12} \ 0 \ -s_{12}]^T \quad (2.1)$$

$$x_{Tb}^B = (e^{\hat{y}\theta_1} e^{\hat{x}\theta_2} e^{\hat{y}\theta_3}) [1 \ 0 \ 0]^T = [c_1 c_3 - s_1 c_2 s_3 \quad s_2 s_3 \quad -s_1 c_3 - c_1 c_2 s_3]^T \quad (2.2)$$

where $\hat{x}, \hat{y} \in \mathbb{R}^{3 \times 3}$ is the skew-symmetric matrix of $x, y \in \mathbb{R}^3$, θ_i is the angle of rotation of the rocker joint and 2-DOF passive joints, c_i and s_i denote $\cos(\theta_i)$ and $\sin(\theta_i)$, respectively, and c_{ij} and s_{ij} denote $\cos(\theta_i + \theta_j)$ and $\sin(\theta_i + \theta_j)$, respectively. Thus, it is shown that the direction of traction force does not deviate from the heading direction of the robot in the pitch-pitch-roll case; that is, while the y component of x_{Ta}^B is zero, it is not zero in the case of x_{Tb}^B .

2.3 Shape of drive tracks

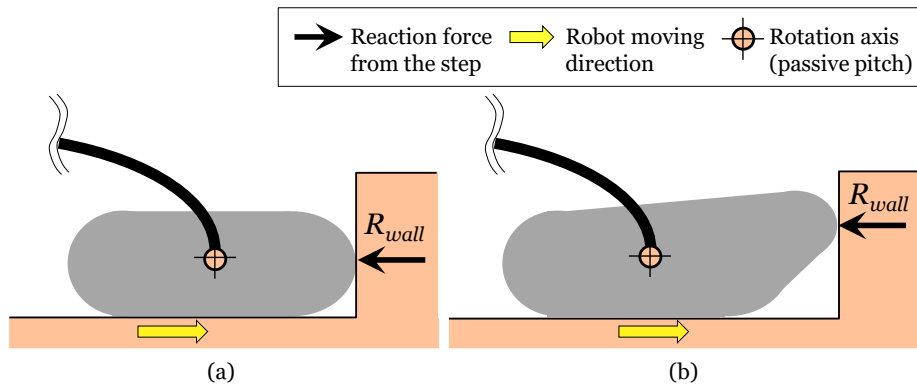


Fig. 2.5 Comparison of flat track and triangular shaped track when encountering a step obstacle

The track is designed to have a triangular shape rather than a flat ellipse. Fig. 2.5 shows the PATRo mechanism with flat tracks and the PATRO mechanism with triangular tracks meeting a step obstacle. In the case of the flat track in Fig. 2.5(a), the step obstacle higher than the track radius cannot be overcome. However, in the case of the triangular shaped track in Fig. 2.5(b), the reaction force from the vertical wall of the step acts as a moment for lifting the track upward so that the track can overcome the step.

2.4 Other mechanical features of PATRo

Each passive pitch and roll joint has a joint limit, which prevents the failure mode in which the posture of the track is tilted more than necessary in severely sloped terrain, thereby impairing the posture stability of the mobile robot. Also, the left and right rocker links are connected through a differential gear in the main body, so that the pitch of the main body is the median value of the slope of the left and right rockers.

Chapter 3. Performance evaluation of PATRo by dynamics simulation

In order to verify the structural validity of the proposed PATRo mechanism, simulations of various locomotion mechanisms for rough terrain driving were carried out under the same conditions, and the results were compared. In this chapter, the subject locomotion mechanisms to be compared with, the simulation configuration, and the simulation results are discussed.

3.1. Various locomotion mechanisms to be compared

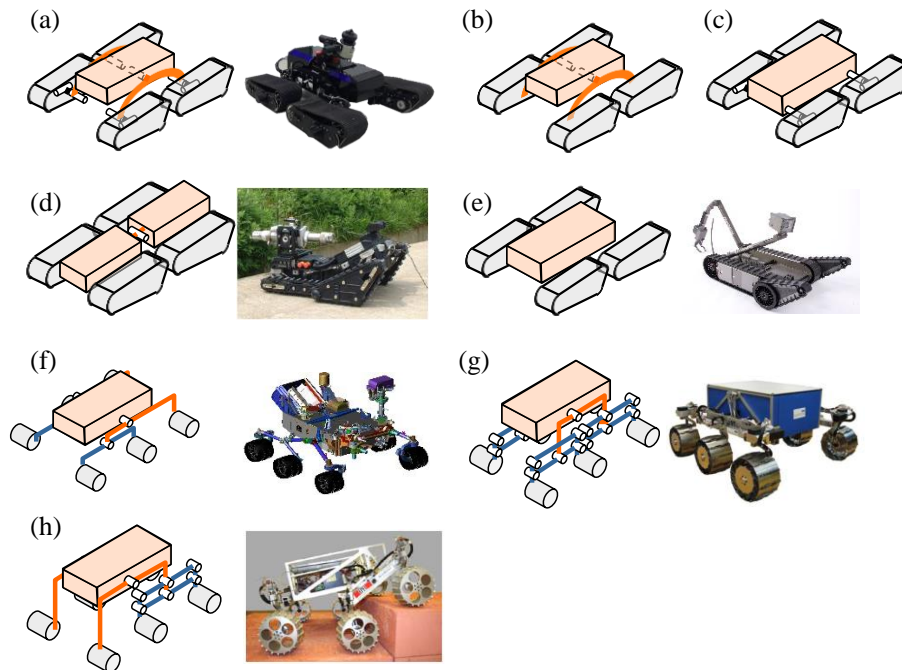


Fig. 3.1 Various subject locomotion mechanisms to be evaluated and compared: (a) PATRo, (b) articulated quad-tracks with rockers, (c) articulated quad-tracks with passive 2-DOF joints, (d) articulated quad-tracks with central pitch joint (with Robhaz [27]), (e) non-articulated quad-tracks (with Packbot [7]), (f) rocker-bogie (with Curiosity [1-4]), (g) CRAB [12], (h) RCL-E [12]

Simulations of a total of eight rough terrain locomotion mechanisms were performed, and the structure of each mechanism

is shown in Fig. 3.1. First, four articulated tracked type mobile robots are represented in Fig. 3.1(a)–(d). The PATRo mechanism is depicted in Fig. 3.1(a); and Fig. 3.1(b) shows an articulated track with rocker links and no pitch–roll passive joints. Fig. 3.1(c), on the other hand, is a track–type mobile robot with pitch–roll passive joints and no rocker joints. Fig. 3.1(d) shows a structure in which the two front tracks and the two rear tracks are connected by a central passive pitch joint. This structure has been adopted in Robhaz from KIST [27], as well as in a number of commercial offroad tracked vehicles [28], and is also the basis for snake–like mobile robots for rough terrain [29]. In addition, the non–articulated tracked type robot shown in Fig. 3.1(e) was also simulated. Packbot from iRobot [7] is an example of this mechanism. Finally, Fig. 3.1(f), 3.1(g), and 3.1(h) show 3 wheel–linkage type mobile robots, including the rocker–bogie [1–4], CRAB [12], and RCL–E [12] mechanisms, respectively.

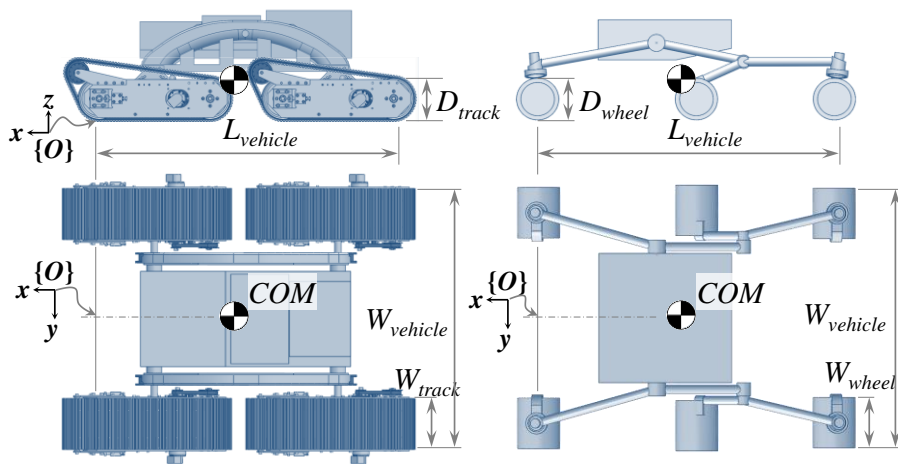


Fig. 3.2 Unification of kinematic parameters of mobile robots

Table 3.1 Mass and dimensions for various locomotion mechanisms in simulation environment

$L_{vehicle}$	875 mm
$W_{vehicle}$	775 mm
W_{track} and W_{wheel}	150 mm
D_{track} and D_{wheel}	124.5 mm
Total mass of four tracks / six wheels	48.5 kg
Total mass of linkages (rockers and bogies)	10.2 kg
Mass of main body	23.0 kg
Position of COM (w.r.t. $\{O\}$ in Fig. 3.2)	x : -426 mm, y : 0 mm z : 124 mm

For a fair comparison of the locomotion mechanisms, the size, total mass, and mass distribution of the eight mechanisms are all unified as shown in Fig. 3.2 and Table 3.1. The design, size, and mass of the PATRO mechanism are set based on those of the prototype shown in Fig. 2.2(a).

3.2. Rough terrain driving scenarios

Three different types of rough terrain, incorporated to compare the performances of PATRO relative to the other mobile mechanisms, are introduced in this section. In each scenario, the geometric characteristics of the terrain and reference trajectory are set differently. That is, the three different types of terrain are incorporated in this study in order to prevent some undesired biases due to specific geometric components of the terrain in comparing the mobile mechanism performances. The 3 scenarios are described in Fig. 3.3 and Table 3.2. The dotted lines in Fig. 3.3 indicate the desired trajectory of the left and right wheels or tracks.

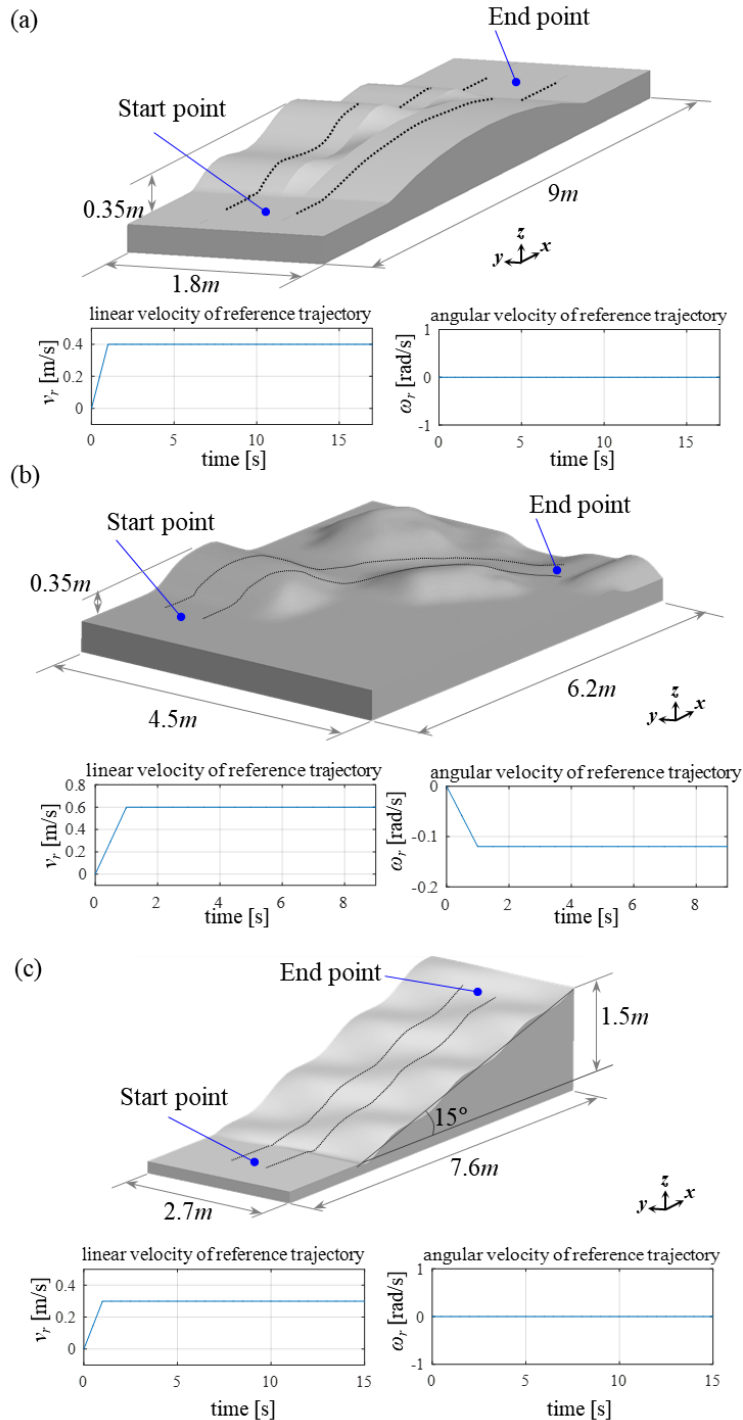


Fig. 3.3 Test terrain and reference velocity in three scenarios: dimensions of terrain model in (a) scenario 1, (b) scenario 2, and (c) scenario 3; reference linear and angular velocities in (d) scenario 1, (e) scenario 2, and (f) scenario 3

Table 3.2 Configurations of three scenarios: shape of reference trajectory, reference velocity, and simulation time

	Scenario 1 (unsymmetric wavy bump)	Scenario 2 (irregular wavy bump)	Scenario 3 (2D sine wave on ramp)
Shape of reference trajectory	Straight line	1/4 arc of circle (radius: 5m)	Straight line
Reference velocity	v_r : 0.4 m/s; ω_r : 0 rad/s	v_r : 0.6 m/s; ω_r : -0.12 rad/s	v_r : 0.3 m/s; ω_r : 0 rad/s
Total simulation time	17 seconds	9 seconds	15 seconds
Notes	- Used as a test terrain in Mars Rover development [26]	- Irregular hills and pits	- Sine magnitude: 96mm, - - Sine wavelength: 4m - Ramp slope: 15°

3.3. Simulation configuration

The block diagram of the overall simulation architecture in this study is shown in Fig. 3.4. It is composed of both a reference posture tracking controller and a dynamics simulator in a cascaded way. First, the reference posture tracking controller is based on the control rule presented by Kanayama et al. [31], as expressed in Eqs. (3.1) and (3.2).

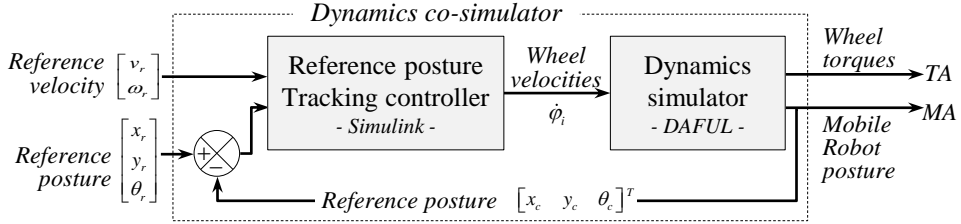


Fig. 3.4 Block diagram of overall simulation architecture based on MATLAB/Simulink and DAFUL

$$v_t = v_r \cos \theta_e + K_x x_e \quad (3.1)$$

$$\omega_t = \omega_r + v_r (K_y y_e + K_\theta \sin \theta_e) \quad (3.2)$$

where v_r and ω_r are the linear and angular reference velocities, respectively. The error posture (x_e, y_e, θ_e) is the difference between the reference posture (x_r, y_r, θ_r) of the given trajectory and the mobile robot current posture (x_c, y_c, θ_c) . As depicted in Fig. 3.5, The error posture is expressed with respect to the local frame fixed to

the mobile robot body, and can be expressed as in Eq. (3.3).

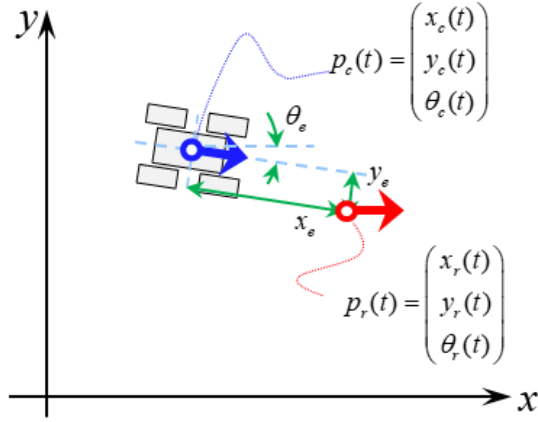


Fig. 3.5 Description on the reference posture, current posture, and error posture

$$\begin{pmatrix} x_e \\ y_e \\ \theta_e \end{pmatrix} = Rot(\hat{z}, -\theta_c) \begin{pmatrix} x_r - x_c \\ y_r - y_c \\ \theta_r - \theta_c \end{pmatrix} \quad (3.3)$$

The target velocities v_r and ω_r obtained from Eqs. (3.1) and (3.2) are converted to the angular speed of each driving wheel or track based on the skid-steer kinematic model of each mobile robot. The obtained angular speeds of the driving wheels or tracks are then transmitted to DAFUL, the multibody dynamics simulation software, for every iteration step. That is, this simulation configuration can be thought of as Software-in-the-Loop (SIL). Finally, TA and MA can be obtained from this dynamics simulation results. DAFUL is a reliable simulation software specialized in the analysis of tracked systems and car systems.

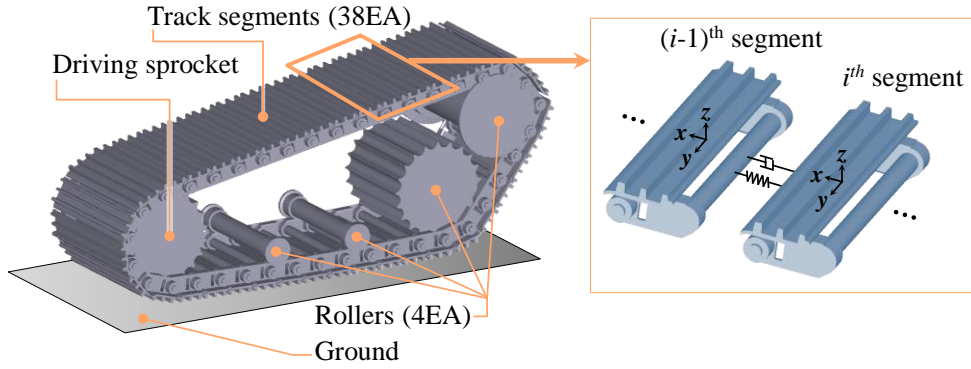


Fig. 3.6 Mechanical structure of driving tracks in simulation environment

Table 3.3 Contact conditions for tracked vehicles in simulation

	k [N/mm]	c [N·s/mm]
Driving sprocket – track segment	1e7	1e4
Roller – track segment		
Ground – track segment		
Track segment – track segment (translational)	1e7	1e5
Track segment – track segment (rotational)	5e8 (x, y) 1e6 (z)	1e5

In the simulation, the driving track consists of one driving sprocket which is the source of traction, four rollers, and 38 track segments as shown in Fig. 3.6. In order to ensure a natural track behavior, it is important to accurately set the contact conditions between the sprocket and track segments, between the roller and track segments, and between the adjacent track segments. The contact conditions between the parts can be represented by the values of virtual stiffness and virtual damping, as summarized in Table. 3.3. The values are obtained by trial and error.

The other setting values used in the simulation are as follows. The maximum static friction coefficient μ_s of 0.7 and the kinetic friction coefficient μ_k of 0.5 were used between the track and the ground. The mesh size of the contact surface was set so that the surface angular tolerance is 7 degrees. The control gain of the mobile robot posture tracking controller is selected through several preliminary simulations. As a result, K_y and K_θ are set as $32m^{-2}$ and

$8m^{-1}$, respectively, and K_x is set at $0.1s^{-1}$ in scenario 1, and $0.3s^{-1}$ in scenarios 2 and 3. It is important to note here that, while the control algorithm and the control gain definitely affect the simulation results, they are not selected to be advantageous for the performance of the proposed PATRO structure. The control algorithm and the gain values are unified to eliminate the effects of the controller and to compare only the performances of the mechanisms.

3.4. Simulation results and discussions

This section presents the results of a total of 24 simulations from 8 mechanisms and 3 scenarios. As an example, the simulation result of the PATRO in scenario 1 is represented in Fig. 3.7. Please refer to the supplementary video [32] for all simulation results. In this paper, for convenience, we abbreviate the names of the eight mechanisms in Fig. 3.1 to A, B, C, D, E, F, G, and H, representing the PATRO, articulated quad-tracks with rockers, articulated quad-tracks with passive 2-DOF joints, articulated quad-tracks with central pitch joint, non-articulated quad-tracks, rocker-bogie, CRAB, and RCL-E, respectively. In this section, the structural validity of the PATRO mechanism is discussed in terms of three structural features of the PATRO mechanism: ‘2-DOF passive joints’, ‘a rocker DOF’, and ‘tracked mechanisms versus wheeled mechanisms’.

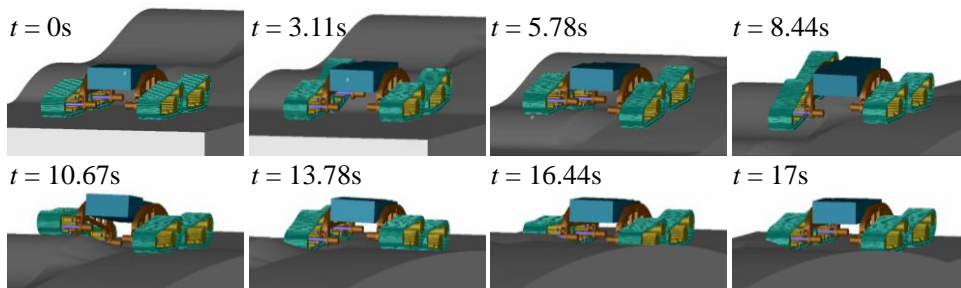


Fig. 3.7 Snapshot of dynamics simulation (PATRO on scenario 1)

3.4.1. Comparison of mechanisms A and B: effect of pitch-roll 2-DOF passive joints on TA and MA

The difference between mechanisms A and B is the presence or absence of the pitch-roll 2-DOF between the rocker links and the tracks. Therefore, we can confirm the need for the 2-DOF passive joint by comparing mechanisms A and B. Fig. 3.7(a) shows the standard deviation of the four track-ground reaction forces of mechanisms A and B. The mean values of the standard deviation profile of mechanisms A and B are 12.67N and 23.78N, respectively. That is, according to the simulation result in Fig. 3.7(a), the better contact between driving tracks and ground through the 2-DOF passive joint results in better load distribution, which is closer to the uniform distribution on the four driving tracks.

The values of TA and MA of mechanisms A and B in the three driving scenarios are shown in Fig. 3.8 and Table 3.4. It can be seen that the TA and MA are lower in mechanism A than in B in all driving scenarios, and this proves that passive pitch-roll 2-DOF actually plays the intended role of achieving good contact condition, and finally reduces the TA and MA of the mobile robot mechanism.

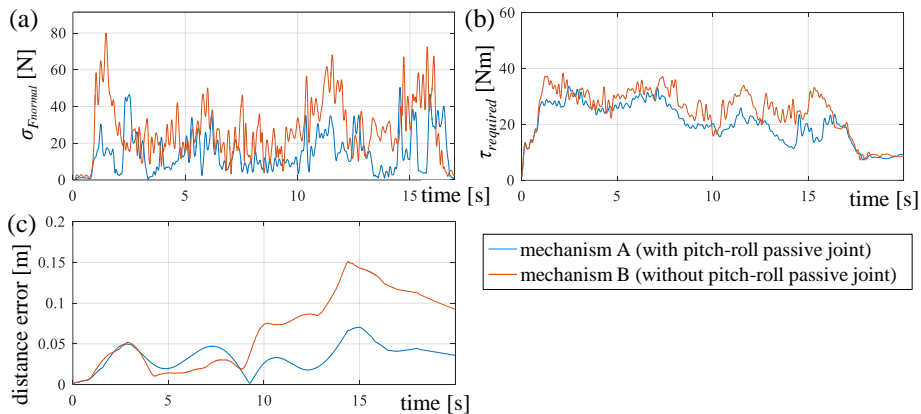


Fig. 3.8 Comparison of mechanisms A and B: (a) standard deviation of ground reaction forces of four tracks, (b) total required torque, and (c) trajectory tracking error (in driving scenario 1)

3.4.2. Comparison of mechanisms A and C: effect of 1-DOF for rocker pitching on TA and MA

Similarly, the expected role of the pitching motion of the rocker link can be verified by comparing the dynamic behavior of mechanism A with that of mechanism C.

As can be seen in Fig. 3.9, Fig. 3.10 and in the supplementary video [32], in the case of mechanism C, the four tracks are sometimes tilted in unnatural ways. This can be explained by the concept of velocity constraint violation (VCV) proposed by Thuerer et al. [23]. If a mobile robot is running on a plane and the same speed is set for all wheels or tracks, no slip will occur under ideal conditions. However, in rough terrain, kinematic constraints require every wheel or track to run at individual speeds; thus, deviation from the ideal velocity is more frequent and the slip level increases. Especially, in the simulation environment of this study, the ground-track friction is not small; the tracks thus did not overcome the frictional force and adapt to the ground by slipping. However, it is worth noting that this phenomenon does not occur in mechanism A, which has a greater DOF than mechanism C. This is because the variation of the position and pose of each of the four tracks is broadened by the rocker's DOF, thereby helping to mitigate the velocity violation. Therefore, although the passive 2-DOF joints (as mechanism C) are sufficiently redundant for instantaneous full contact of the four tracks, to compensate for the difference in speed between the front and rear tracks, the additional rocker DOF (as mechanism A) is required for continuous full contact while driving.

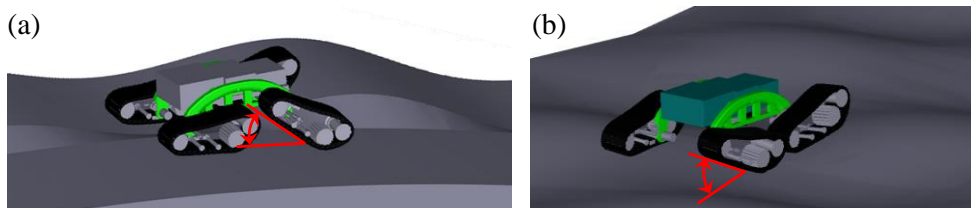


Fig. 3.9 Snapshot of dynamics simulation when a track of mechanism C is tilted unnaturally in (a) scenario 1 and (b) scenario 2

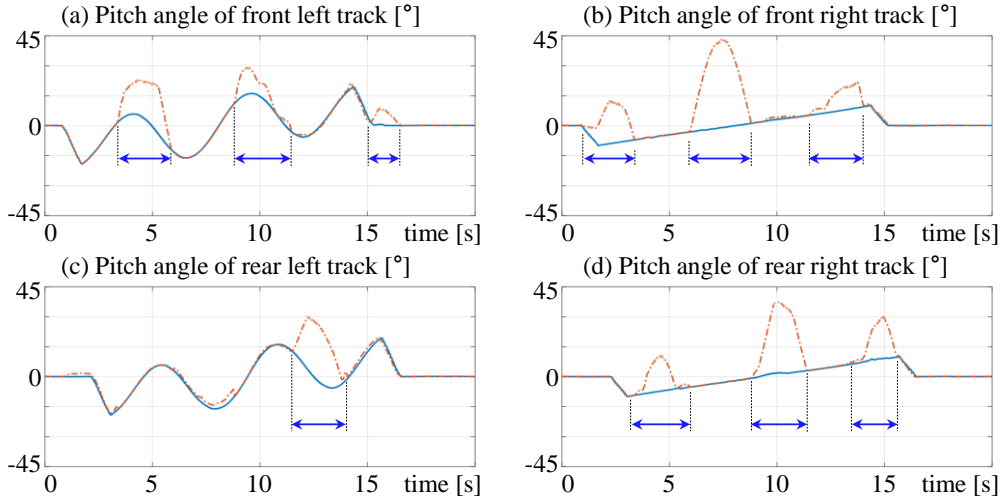
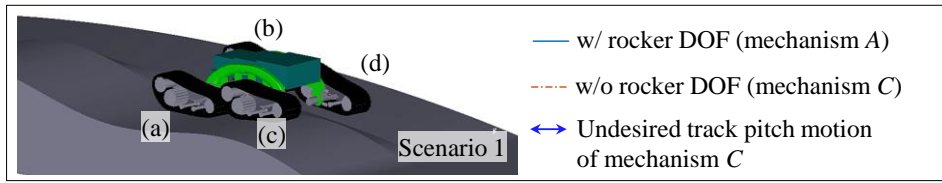


Fig. 3.10 Comparison of pitch angle profiles of four tracks in mechanism A and C on scenario 1: (a) front left track, (b) front right track, (c) rear left track, (d) rear right track

3.4.3. Comparison of PATRO and all wheeled platforms

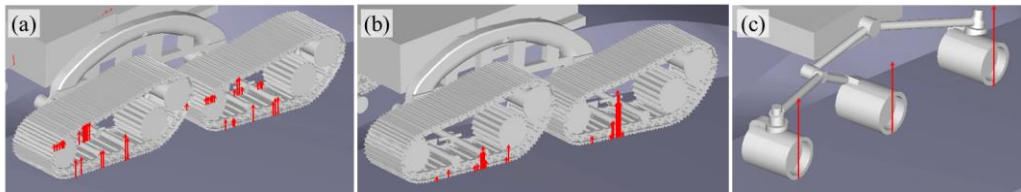


Fig. 3.11 Comparison of contact under the same conditions: (a) surface contact of mechanism A, (b) edge contact of mechanism B, (c) point contact of mechanism F

According to the simulation results in Fig. 3.13, Fig. 3.14 and Table 3.4, the TA and MA of the PATRO are better than those of the wheeled mechanisms. This can be explained by the differences in the contact conditions between the driving track/wheel and the ground. Fig. 3.11 compares the ground reaction forces of mechanisms A, B, and F, measured at exactly the same time in

scenario 1. The ground reaction forces are represented by red arrows. In Fig. 3.11(a), each track of PATRO has surface contact with the ground and the reaction force is distributed to various points on the bottom surface of the track. In contrast, in the case of mechanism B shown in Fig. 3.11(b), the ground reaction forces are concentrated at the right end edge rather than being dispersed on the track bottom. Moreover, in mechanism C shown in Fig. 3.11(c), the ground reaction force occurs intensively at one point at each driving wheel.

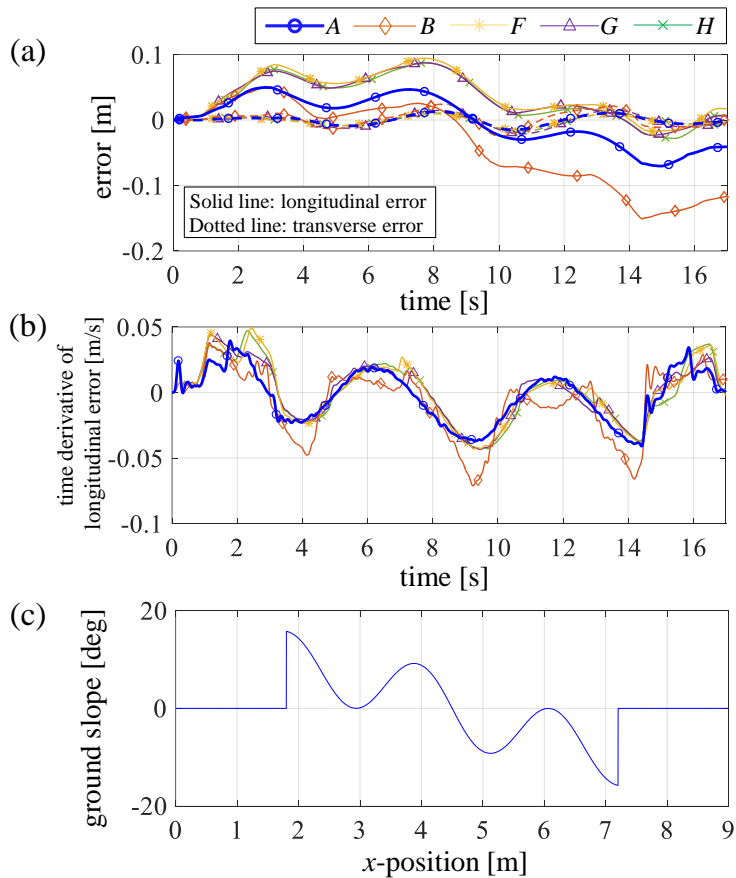


Fig. 3.12 (a) trajectory tracking error of mechanisms A, B, F, G, and H, (b) time derivative of longitudinal error, (c) ground slope of the terrain model (all in scenario 1)

Fig. 3.12(a) shows the longitudinal and transverse error of the five mechanisms. The longitudinal error is the tracking error component in the mobile robots' heading direction, and the

transverse error is the tracking error component which is perpendicular to the heading direction. According to the figure, the MA of mechanism A is smaller than that of the wheeled mechanisms F, G, and H, but MA of the wheeled mechanisms is smaller than that of mechanism B throughout all simulation periods. This confirms that, if the DOF of each driving track is not sufficient, the MA of the tracked type mechanism is larger than that of the wheel type mechanisms, yet by providing additional passive DOFs, the MA value can be reduced to lower than that of the wheel type mechanisms by improving the contact conditions from the edge contact to the surface contact. Figs. 3.13 and 3.14 show further simulation results of scenarios 2 and 3.

Also, a comparison of the tracking error with the ground slope demonstrates that the slip between the robot and the ground affects the size of the trajectory tracking error. Fig. 3.12(b) shows the time derivative of the longitudinal error of each mechanism in scenario 1. Fig. 3.12(c) shows the median value of the ground slope of the left part and the right part of the terrain in scenario 1. Here, we can see that Fig. 3.12(b) and 3.12(c) show similar graph shapes, which means that the longitudinal error increases in uphill and decreases in downhill.

3.4.4. Overall simulation results

Figs. 3.13 shows the performance of the eight driving mechanisms in each driving scenario in terms of TA and MA. Among the 24 simulations, mechanism D failed to overcome the terrain of scenario 1; a total of 23 points are therefore plotted in Fig. 18. The simulation failure image can be found in the supplementary video [32]. Also, the eight mechanisms are categorized into three groups (articulated tracked mechanism, non-articulated tracked mechanism, and wheel-linkage mechanism), and the distribution regions of each group are shown in Fig. 3.13. Note that in Fig. 3.13(b), the point of mechanism D is regarded as an outlier and is not included in the region of the articulated tracked mechanism

group. As shown in the supplementary video [32] the behavior of the mobile robot diverged nonlinearly while overcoming obstacles, so it was determined that the simulation result could not represent the performance of the mechanism. The raw data profiles of total required torque and trajectory tracking error of all the simulations are given in Fig. 3.14 and Table 3.4. Note that a 6th-order low pass Butterworth filter was used in the torque profiles, and the sampling frequency and cutoff frequency of the filter are 100Hz and 5Hz, respectively.

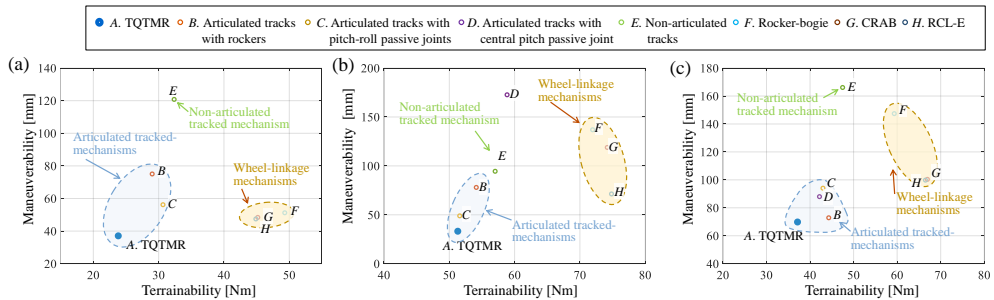


Fig. 3.13 Comparison of eight mobile robot mechanisms on TA-MA plane, in (a) driving scenario 1, (b) driving scenario 2, and (c) driving scenario 3

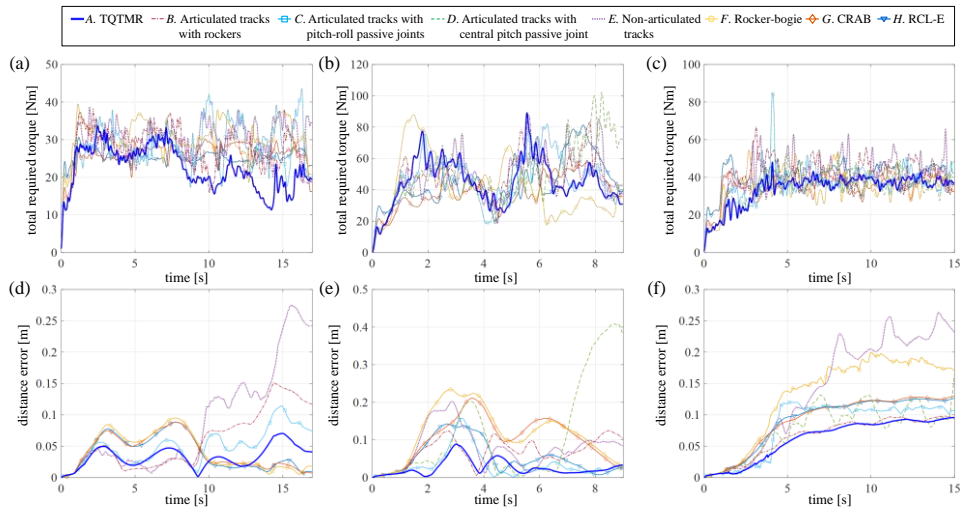


Fig. 3.14 Raw data profiles of simulation results: (a) TA in scenarios 1, (b) TA in scenario 2, (c) TA in scenario 3, (d) MA in scenarios 1, (e) MA in scenario 2, (f) MA in scenario 3

Table 3.4 Values of TA and MA of all mechanisms in three scenarios

		Mechanism							
	Scenario	A	B	C	D	E	F	G	H
TA [Nm]	1	23.80	28.98	30.66	-	32.38	49.32	45.17	44.89
	2	51.30	54.16	51.57	58.87	57.01	71.97	74.19	74.83
	3	37.09	44.25	42.96	42.18	47.46	59.37	66.95	66.49
<i>TA ratio of mechanism A over each mechanisms (average in three scenarios)</i>		-	0.87	0.88	0.88	0.81	0.61	0.59	0.59
MA [mm]	1	37.19	74.96	56.19	-	120.82	51.16	48.31	47.44
	2	33.13	77.82	49.02	172.80	94.67	136.90	118.79	71.21
	3	69.84	72.96	93.94	87.92	165.99	147.54	100.33	99.78
<i>MA ratio of mechanism A over each mechanisms (average in three scenarios)</i>		-	0.63	0.69	0.49	0.36	0.48	0.58	0.65

Chapter 4. Mobile robot kinematics of PATRo

4.1. Necessity of kinematic analysis of PATRo

A mobile robot with a skid–steer steering system controls the linear velocity and angular velocity of the mobile robot with respect to the global coordinate system on the assumption that all the driving wheels and track contact are in the same plane on the ground. However, due to the complexity of the ground, the movements of the mobile robot on the rough terrain have an arbitrary orientations of the wheels or tracks, compared to the main body. Tarokh [26] proposed a kinematic model for evaluating the contact angle of the drive wheel and the ground by considering the motion of a 6–DOF rocker–bogie suspension. However, since this study focuses on reducing the effect of slip on a given evaluation map by compensating for the difference in wheel–to–ground contact points, satisfactory trajectory tracking performance can not be expected in the case of insufficient information about the environment. Thus, we propose a new suspension kinematics based on velocity propagation which can successfully calculate contact angle between the tracks and the ground, in arbitrary rough terrain without any prior information.

4.2. Mobile robot kinematics of PATRo

In the case of a robot with four tracks, a skid–steering kinematics such as Eq. (4.1) is generally used to move at the target linear velocity and angular velocity (v_{des}, ω_{des}) .

$$\begin{aligned}\dot{\phi}_{FL} = \dot{\phi}_{RL} &= (v_{des} - \omega_{des}l) / r \\ \dot{\phi}_{FR} = \dot{\phi}_{RR} &= (v_{des} + \omega_{des}l) / r\end{aligned}\tag{4.1}$$

However, since the orientation of each drive track of PATRo changes independently according to the shape of terrain, the kinematics in Eq. (4.1) that does not take this into consideration is

degrades the position control performance.

In this study, the track velocity compensation algorithm considering the articulation of the robot which changes randomly in the rough environment is presented. As shown in Fig. 4.1(a), the velocity of the drive track can be obtained as the sum of the driving velocity (v_{drive}) and the relative velocity of the track relative to the main body (v_{rel}). The driving velocity v_{drive} is made by the rotation of the driving motor, and the v_{rel} is the relative velocity of each track with respect to the main body caused by the change of the PATRo articulation.

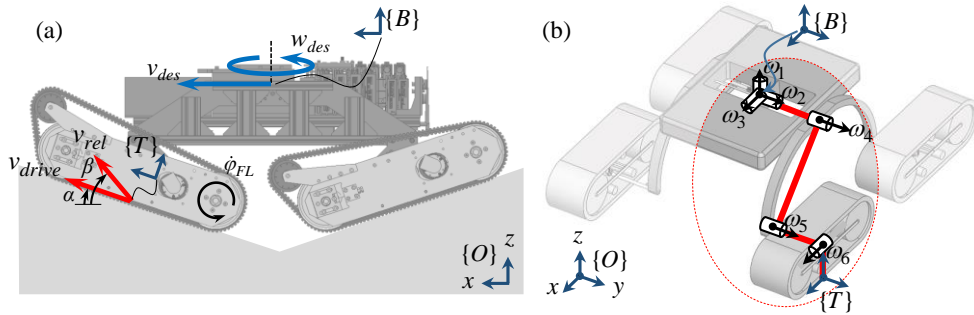


Fig. 4.1 Mobile robot kinematic analysis: (a) velocity of the driving track, (b) coordinate frames and axes of rotation for kinematic analysis

Since the z -component and the y -component of the robot velocity are not uncontrollable, the equation for the x -component of the robot velocity is as follows.

$$v_{drive} \cos \alpha + v_{rel} \cos \beta = v_{des} \pm \omega_{des} l \quad (4.2)$$

The left side of Eq. (4.2) is the actual velocity of each track as the sum of the x -components of v_{drive} and v_{rel} , and the right side is the target velocity of each track to have the desired linear velocity and angular velocity, as shown in Eq. (4.1). Therefore, the speed of the drive motor is determined as follows.

$$\dot{\varphi} = \frac{v_{des} \pm \omega_{des} l - v_{rel} \cos \beta}{r \cos \alpha} \quad (4.3)$$

In Eq. (4.3), v_{des} and ω_{des} are determined by the posture tracking controller, and v_{rel} , α , β are obtained by solving the kinematic model of the mobile robot. First, the relative position of the coordinate system {B} to the coordinate system {T} is expressed by the form of POE (product of exponentials) as shown in Eq. (4.4). As shown in Fig. 4.1 (b), {B} is a coordinate system located at the center of the robot and having the orientation of $I_{3 \times 3}$, and {T} is a coordinate system attached to the center point of the bottom surface of the track. Then, the spatial velocity of {T} expressed in {B} can be expressed as Eq. (4.5) using Jacobian matrix can be obtained. Therefore, the moving speed v_{rel} of the center point of the track bottom can be obtained as in Eq. (4.6).

$$g_{BT}(\theta) = e^{\hat{z}_1 \theta_1} e^{\hat{z}_2 \theta_2} e^{\hat{z}_3 \theta_3} e^{\hat{z}_4 \theta_4} e^{\hat{z}_5 \theta_5} e^{\hat{z}_6 \theta_6} g_{BT}(0) \quad (4.4)$$

$$V_{BT}^B = J_{BT}^B(\theta) \dot{\theta} = \begin{bmatrix} v_{BT}^B \\ \omega_{BT}^B \end{bmatrix} = \begin{bmatrix} -\dot{R}_{BT} (R_{BT})^T P_{BT} + \dot{P}_{BT} \\ \left(\dot{R}_{BT} (R_{BT})^T \right)^\vee \end{bmatrix} \quad (4.5)$$

$$v_{rel} = \dot{P}_{BT} = v_{BT}^B + \dot{R}_{BT} (R_{BT})^T P_{BT} \quad (4.6)$$

4.3 Verification through dynamics simulation

Through the dynamics simulation, we compared the effect of the new skid-steering kinematics and the proposed kinematics reflecting the mechanism of the platform on the unsymmetric wavy bump. The distance error is shown in Fig. 4.2 (b). Each RMS error was 45.6mm and 37.4mm, respectively, thus the trajectory tracking error was reduced by 17.9% using the proposed kinematics. The result of experimental verification is in Ch. 7.2.3.

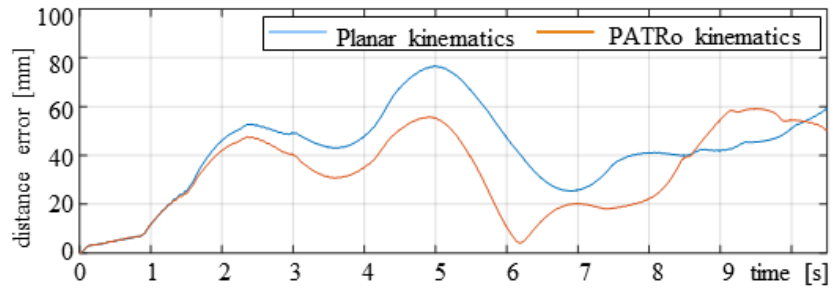


Fig. 4.2 Verification of the proposed PATRo kinematics through dynamics simulation

Chapter 5. Optimal design of PATRo based on kinetostatic analysis

5.1. Previous researches for optimal design of mobile robots

The followings are the previous studies on the optimal design of the mobile robot mechanisms. Alamdari et al [33] minimized the risk of slippage (μ) of the leg-wheel system overcoming the step obstacle through kinetostatic analysis. Meghdari et al [34] also minimized the maximum instantaneous power of the shrimp platform climbing the stairs through the kinematic analysis and genetic algorithm. Kim et al [35] maximized the posture stability of the rocker-bogie mechanism during stair climbing using the kinematic analysis and the Taguchi methodology. Choi et al [36] improved the step-climbing capability of RHyMo platform by kinetostatic analysis.

There have been a lot of studies on the design and development of mobile robots, while the research on optimization of robotic mechanisms has not been relatively studied. The first reason for this is because the operation environment for mobile robots is hard to be specified, and the second is because there is no performance index used in common. Especially, as can be inferred from the word 'rough terrain', it is ambiguous and controversial to specify the features of the operation environment in case of rough terrain mobile robots. Unstructured user conditions make it difficult to clearly specify the required functions of the robot and make it difficult to define the optimization problem. Also, there are various performance indices that define the performance of the mobile robot, such as maneuverability indices, terrainability indices, and trafficability indices. However, the performance index that is used as the objective function of the optimization depends on the purpose of development and the intention of the user. As an opposite case, industrial manipulators used in the factories are also applied to various tasks such as welding, painting, and assembly. However, the application environment is strictly limited and several key indices such as manipulability, workspace, payload, are commonly used by

all the users, so the manipulators are relatively easy to be optimized.

5.2. Optimization problem definition

5.2.1. Cascaded optimization problem definition

As mentioned in Chapter 1.2, the performance indices used in this study are terrainability (magnitude of required torque) and maneuverability (magnitude of trajectory tracking error). However, it is not desirable to perform multi-objective optimization with terrainability and maneuverability as objective functions for PATRo's mechanical optimization. First, terrainability and maneuverability are not completely independent to each other. That is, since the shape of the ground varies according to the movement path of the mobile robot, the robot's motion changes and the torque required thereby changes. Therefore, both terrainability and maneuverability are affected by the actual trajectory of the mobile robot, so they are not independent variables. In this case, when multi-objective optimization is performed to minimize two indices, it is difficult to interpret the optimization result and to give a physical meaning because the result is affected by both objective functions at the same time. Second, optimization of maneuverability is eventually dependent to the control algorithm and control gains. Then, it is difficult to obtain a good optimization result that maximize the own advantages of the PATRo mechanism. Third, in order to optimize terrainability and maneuverability as objective functions, we must run a very large number of 3D dynamics simulations as in Chapter 3.3 in the optimization process, which is a very time-consuming process. (It takes 24 hours for one set of simulation, at i7-6500U 2.5GHz CPU, 16GB RAM)

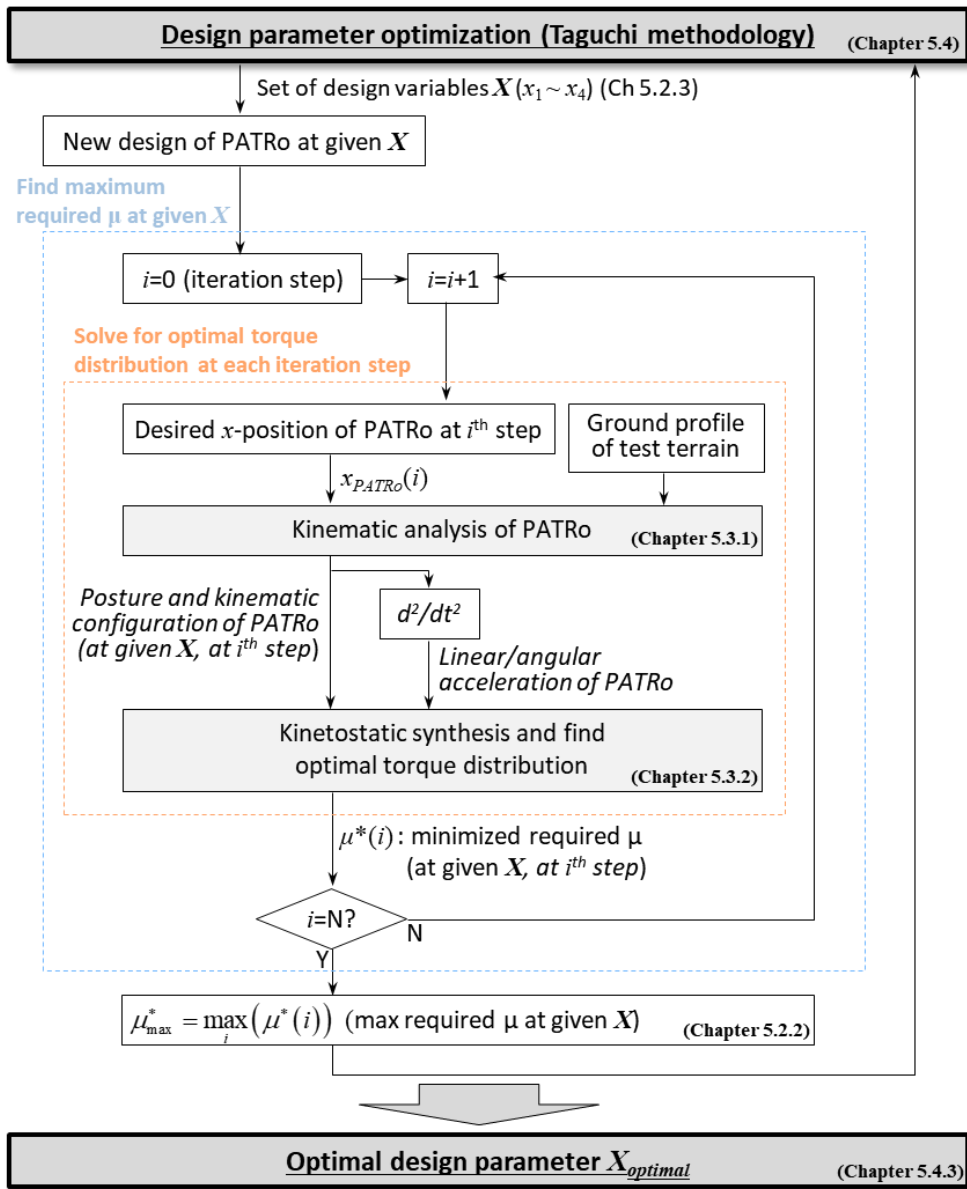


Fig. 5.1 Overall configuration for the cascaded optimization problem

Therefore, I have performed kinestatic analysis to evaluate the performance of PATRo, without using 3d dynamics simulation. The overall optimization process is depicted in Fig. 5.1. In order to calculate the objective function (maximum required friction coefficient, this will be introduced in Ch. 5.2.2) at the given design variables (X , this will be introduced in Ch. 5.2.3) changed by the optimization algorithm, first, we analyze the kinematic configuration

of PATRo while running on the test terrain through (this will be introduced in Ch. 5.3.1). Next, kinetostatic analysis is used to analyze the instantaneous optimal torque distribution at the moment of travel (this will be introduced in Ch. 5.3.2). By kinematic and kinetostatic analysis, it is possible to obtain the necessary friction coefficient while PATRo is running on the test terrain, at the given PATRo design variable. Then finally, the optimal design parameters can be obtained by changing the PATRo design parameter and repeating the kinetostatic analysis. Each process of optimization will be described in detail in next chapters.

5.2.2. Objective function: required friction coefficient

As the objective function, the required friction coefficient μ is minimized to reduce both terrainability and maneuverability. Required friction coefficient μ is an objective function widely used for design optimization of mobile robots [37,38]. If the mobile robot requires smaller μ , then the robot has the following advantages.

- Traction force required to overcome the same obstacle is small.
- The robot can overcome more slippery terrain and obstacles.
- The robot can overcome more challenging obstacles with same driving force.
- The robot is able to have large payload.
- The risk of slip is smaller.

For these reasons, we used μ as an objective function to improve both terrainability and maneuverability at the same time. More specifically, the objective function in this study to minimize ‘the maximum value of the maximum friction coefficient for each of the four driving tracks while driving the unsymmetric wavy bump’. This can be stated as follows.

$$\arg.\min_X \mu_{\max}^* (X) \tag{5.1}$$

$$\mu_{\max}^*(X) = \max_i \left(\max_{FL,FR,RL,RR} (\mu_{FL}(t), \mu_{FR}(t), \mu_{RL}(t), \mu_{RR}(t)) \right) \quad (5.2)$$

$$\mu(t) = \frac{|T(t)|}{N(t)} \quad (5.3)$$

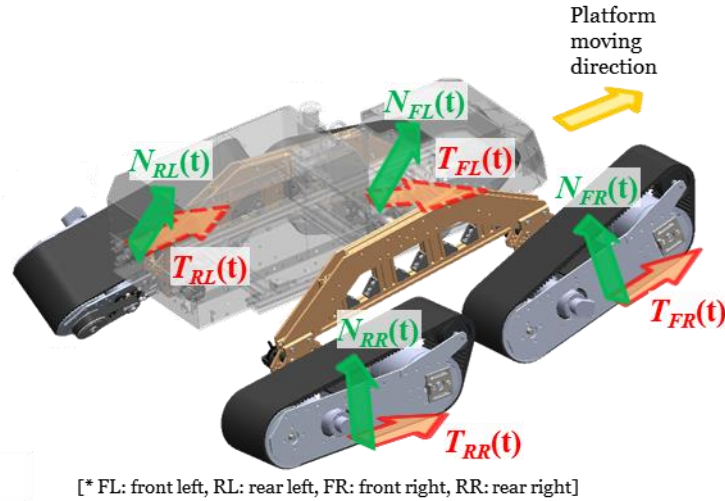


Fig. 5.2 Normal forces and traction forces acting on four drive tracks

5.2.3. Design variables

5.2.3.1. Design variables: PATRo dimension parameters

So what are the factors that affect $\mu_{\max}^*(X)$? The first is the dimension parameters or design parameters, i.e. size of the rockers and the tracks as shown in Fig. 5.3 and Table 5.1. As the dimension parameters X changes, the trajectory of the robot COM and the posture of the robot changes in the rough terrain, so the required μ changes.

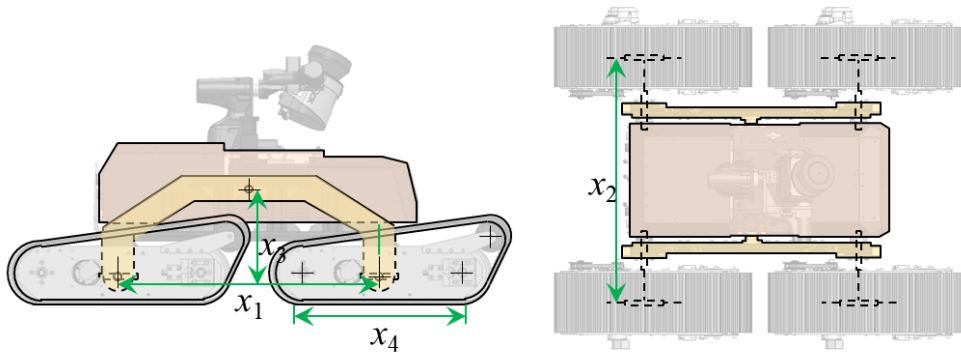


Fig. 5.3 Design variables of PATRo mechanism for design optimization

Table 5.1 Descriptions for design variables

x_1	Longitudinal length of rocker link
x_2	Lateral width of the platform
x_3	Vertical length of rocker link
x_4	Track length (contact length)

5.2.3.2. Need for optimal torque distribution

In addition to the dimension parameters of PATRo, the torque distribution between the four tracks also changes the required μ of PATRo. The following is a simplified half-PATRo model for illustrative purposes. For example, when climbing a ramp having a slope of θ as shown in Fig. Table 5.2, the value of the required friction coefficient changes depending on the distribution of the driving force between the front track and the rear track. Therefore, even when the robot takes the same motion, the required friction coefficient value can be changed depending on how torque distribution is performed.

Table 5.2 Two cases of torque distribution at the same state

	Case 1 ($\tau_R=0$)	Case 2 ($\tau_L=\tau_R$)
N_F	$mg / 2\cos\theta$	$mg / 2\cos\theta$
N_R	$mg / 2\cos\theta$	$mg / 2\cos\theta$
τ_F	$mg / r\sin\theta$	$mg / 2r\sin\theta$
τ_R	0	$mg / 2r\sin\theta$
$\max(\mu_F, \mu_R)$	$2\tan\theta$	$\tan\theta$

Therefore, in order to find the optimal design parameters \mathbf{X} that minimize μ , the torque optimization between the four tracks should be performed at every each set of design variables in the process of optimization.

5.3. Kinetostatic analysis of PATRo

The purpose of this chapter is to determine the magnitude of the required friction coefficient corresponding to the given set of design variables ($x_1 \sim x_4$), in the optimization process. This is done through the following two steps: (1) At the given set of design variables, generate the motion of four tracks, two rockers, and body while the PATRo travels the test terrain. (2) Inverse dynamics analysis to generate the PATRo motion from (1), by kinetostatic analysis. This two-step process is described in detail in the sub-chapters below.

5.3.1. Kinematic synthesis of PATRo for kinetostatic analysis

The goal of this chapter is to generation the 3D motion of PATRo running on the test terrain. The process is subdivided into four steps as in from 5.3.1.1 to 5.3.1.4.

5.3.1.1. Generation of pointwise contour of driving track and test terrain

First, create a 2D pointwise contour along the outline of the drive track as shown in Fig. 5.4. The shape of the track depends on x_4 of the design variables. r is a constant value of 65.9 mm. Next, create a pointwise profile of the left terrain and the right terrain of the unsymmetric wavy bump, which is a test terrain as shown in Fig. 5.5.

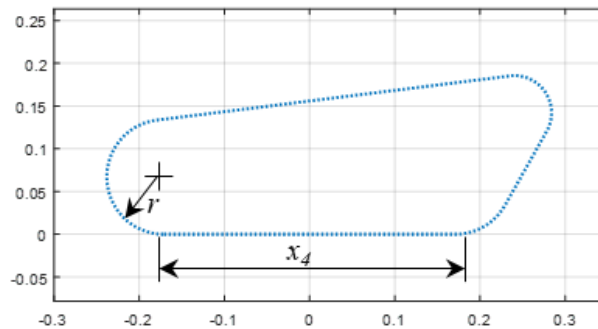


Fig. 5.4 Pointwise contour of a drive track

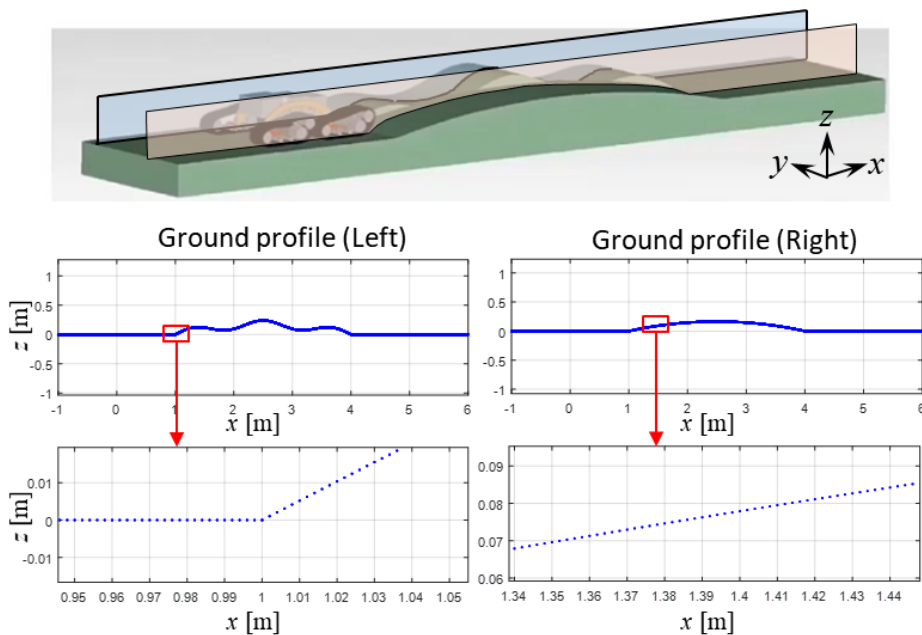


Fig. 5.5 Pointwise contour of the test terrain

5.3.1.2. 2D trajectory generation of a single track

Using the ground contour and track contour generated in Section 5.3.1.1., create the trajectory of a single track that runs on the ground. At this time, the contact analysis of track and ground is conducted. Figure 5.6(a) shows the motion of the driving track (in blue) and the contact area (in red) with the ground while driving the left part of the test terrain (in black). Figure 5.6(b) shows the trajectory of the pitching point to which the rocker is connected in the driving track. This red line is necessary for creating the rocker trajectory in 5.3.1.3. Fig. 5.6(c) and (d) show the motion of the track running on the right side of the test terrain in the same way as above.

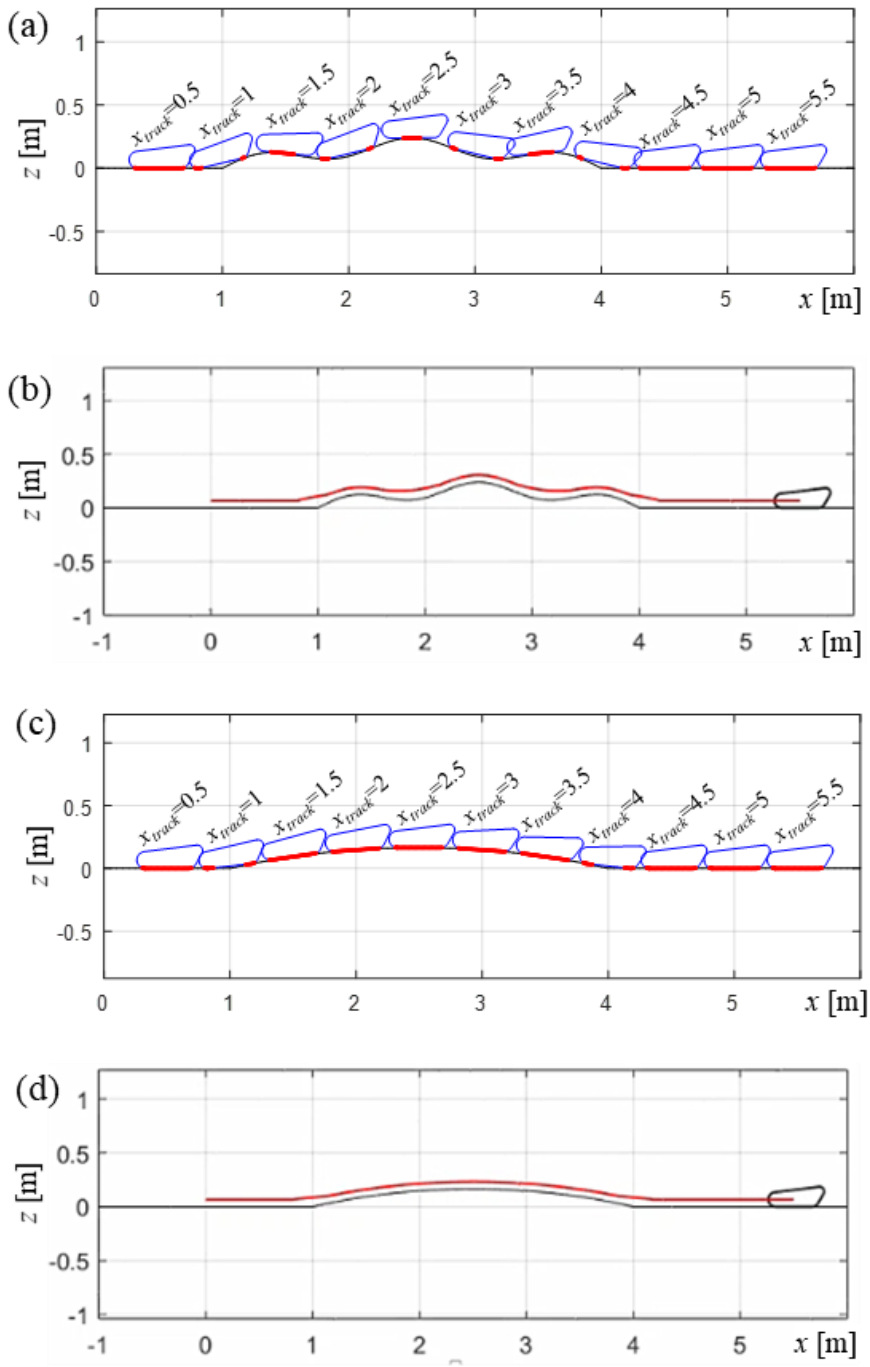


Fig. 5.6 2D trajectory generation of a single track

5.3.1.3. 2D trajectory generation of the half-PATRo

Using the single track trajectory generated in Chapter 5.3.1.2., create the trajectory of the half-PATRo running on the terrain. Half-PATRo consists of three parts: a front track and a rear track, and a rocker link, and they are all constrained to the sagittal plane. Generating the trajectory of half-PATRo means that the whole trajectory of three parts are found during the course of the terrain, which is done in the following way. When the desired x -position of the PATRo body is given at the i -th simulation step, find a couple of two points in the track's pitching point trajectory (the red line in Fig. 5.6(b) and 5.6(d)), which satisfies the following conditions.

- distance between the two pitching joints of the two tracks is x_l (length of rocker link).
- when the rocker is positioned so that the pitching joint of both tracks is at both ends, the pitching joint of the rocker is lying on the desired x -position of the PATRo.

The trajectory of the half-PATRo obtained by this method is shown in Fig. 5.7. The configuration of the half-PATRo is shown in five different iteration steps. The red line shows the trajectory of the track pitching joint obtained in Chapter 5.3.1.2., and the blue line is the trajectory of the rocker pitching joint.

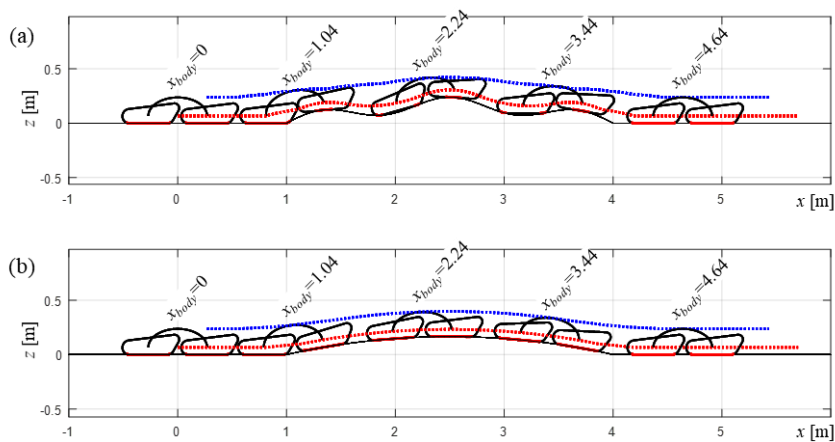


Fig. 5.7 2D trajectory of the half-PATRo model

5.3.1.4. 3D trajectory generation of the full PATRo

The final task is to generate a 3D trajectory of the full PATRo running on the test terrain, combining the left and right trajectories of the half-PATRo obtained in Chapter 5.3.1.3. By adjusting the y position and roll orientation of each parts that were constrained in sagittal plane so far, the 3D trajectory of the full PATRo can be obtained. All of the four design variables $x_1 \sim x_4$ are reflected in this process. The simulation results of the kinematic analysis are shown in Fig. 5.8. Finally, in order to verify the kinematic analysis results of Chapter 3.5.1., the orientation of the PATRo, and the joint positions of the 9-DOF passive joints calculated from the kinematic analysis are compared to those from the dynamics simulation software. Fig. 5.9 is a graph comparing roll, pitch, and yaw of the body according to x position of PATRo on test terrain. Also, Fig. 5.10 is a graph comparing the 9-DOF passive joint angles of PATRo according to the x position of PATRo.

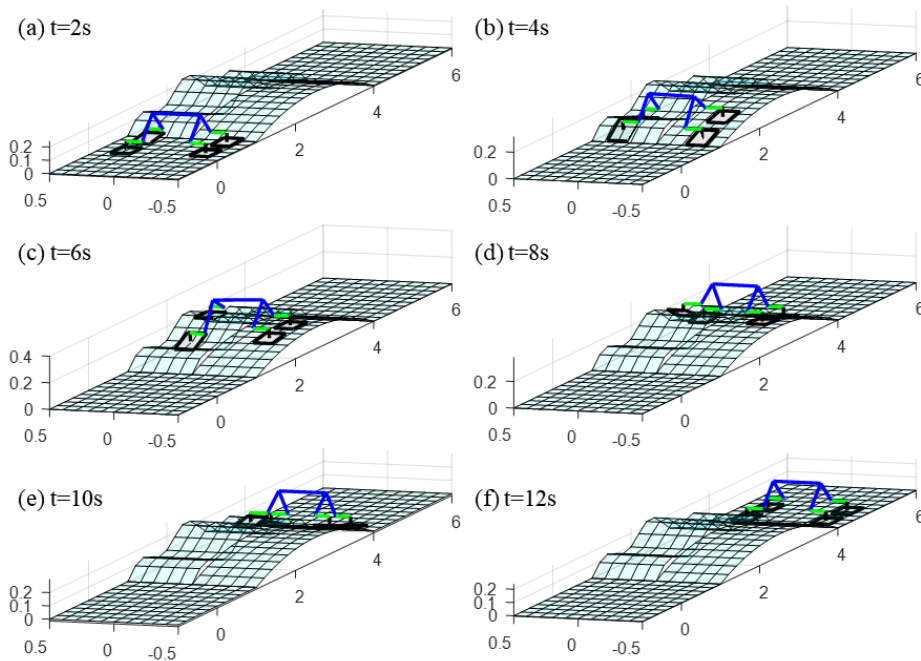


Fig. 5.8 3D trajectory of the full PATRo model

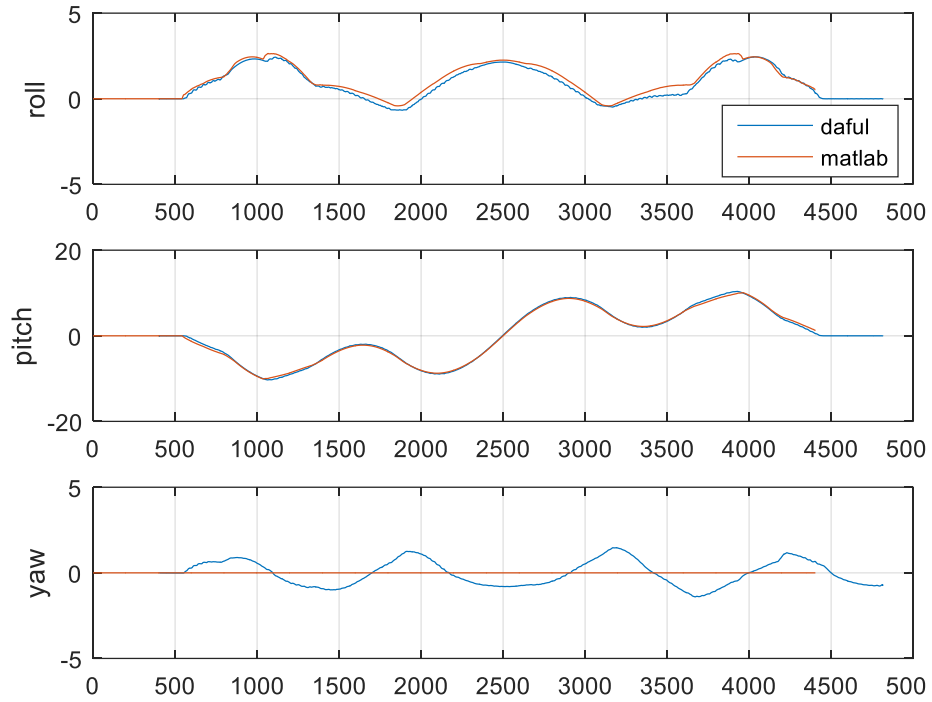


Fig. 5.9 Comparison of PATRo orientation between 3D dynamics simulation result (DAFUL) and kinematic synthesis result (MATLAB)

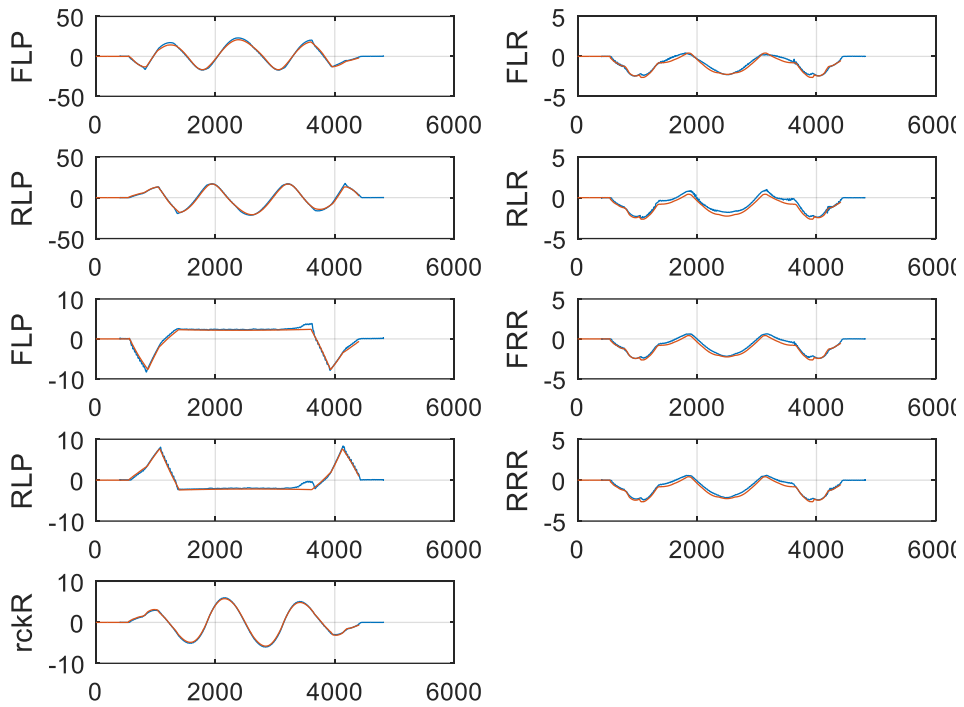


Fig. 5.10 Comparison of PATRo configuration between 3D dynamics simulation result (DAFUL) and kinematic synthesis result (MATLAB)

5.3.2. Kinetostatic analysis and optimal torque distribution

5.3.2.1. Force and moment equilibrium equations for PATRo

All the forces acting on PATRo are shown in Fig. 5.11. The forces are traction forces by the drive motor, ground normal force, gravity forces, and the internal forces between the links.

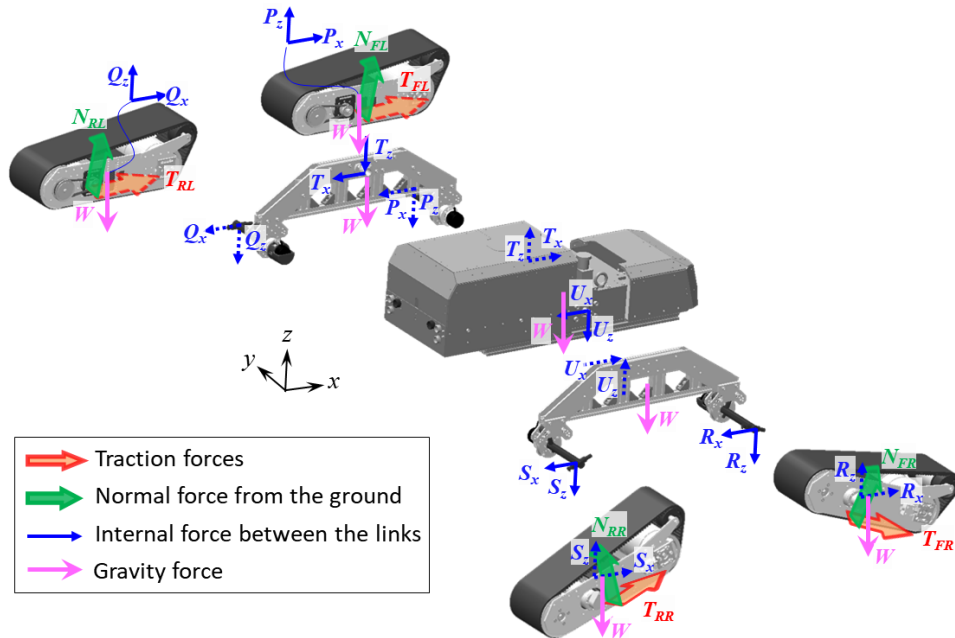


Fig. 5.11 Forces acting on the links of PATRo

Fig. 5.12 depicts the free body diagram of half-PATRo in xz -plane. The following conditions are assumed.

- The heading (yaw) of PATRo is zero while driving the terrain
- The roll of the four drive tracks are zero while driving the terrain. (because the test terrain has curvature only in the direction of travel)

In the terms of Fig. 5.12, FL, RL, FR, RR of subscripts refer to front left, rear left, front right and rear right track, respectively. T is the driving force by the driving motor, N is the reaction force from the ground, and P , Q , R , S , T , and U are the reaction forces between the links. Each reaction force is divided into x and z components, and y is omitted. (T is duplicated, but T is driving

force if the subscript is two letters, and T is link reaction force if the subscript is one letter. For example, T_{RL} is the ground reaction force at the rear left track, and T_x is the x component of the reaction force between the front left track and the left rocker.) Finally, W represents the gravity of each link.

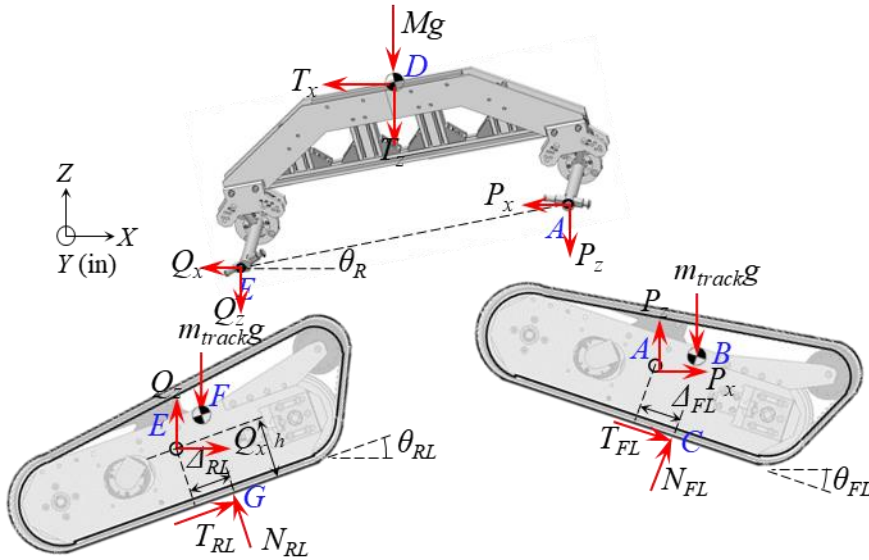


Fig. 5.12 Free body diagram of half-PATRo model (left)

Then the equations for force equilibrium and moment equilibrium are as follows. The notations used in the equation are as follows. First, A, E, H, and L are the points in the track at which the tracks are connected to the rockers (the end of the 2-DOF passive joint). B, F, I, and M are the centers of gravity of the four drive tracks. D and K are positions of points at which the rockers are connected to the main body. And C, G, J, and N are the action point where the traction force and the ground reaction force act on each drive track. Δ represents the distance between two points. For example, Δ_{EA}^x is the magnitude of the x component of the position vector connecting point E and point A in the left rocker. In the case of Δ without a superscript, it represents the distance between the action point of the ground reaction force from the center of the track bottom. Finally, h is the height of the track pitching joint from

the bottom of the track. θ_{FL} is the pitch angle of the front left track, and c_{FL} and s_{FL} represents $\cos(\theta_{FL})$ and $\sin(\theta_{FL})$, respectively (taken FL as an example of four tracks). θ_L and θ_R represent the pitch angles of the left and right rockers.

$$\begin{aligned}
\Sigma F_{x,FL} &= T_{FL}c_{FL} - N_{FL}s_{FL} + P_x = m_{track}\ddot{x}_{FL} \\
\Sigma F_{z,FL} &= T_{FL}s_{FL} + N_{FL}c_{FL} + P_z - m_{track}g = m_{track}\ddot{z}_{FL} \\
\Sigma M_{FL} &= -\Delta_{FL}N_{FL} + hT_{FL} + m_{track}g\Delta_{AB}^x = I_{track}\ddot{\theta}_{FL} \\
\Sigma F_{x,RL} &= T_{RL}c_{RL} - N_{RL}s_{RL} + Q_x = m_{track}\ddot{x}_{RL} \\
\Sigma F_{z,RL} &= T_{RL}s_{RL} + N_{RL}c_{RL} + Q_z - m_{track}g = m_{track}\ddot{z}_{RL} \\
\Sigma M_{RL} &= -\Delta_{RL}N_{RL} + hT_{RL} + m_{track}g\Delta_{EF}^x = I_{track}\ddot{\theta}_{RL} \\
\Sigma F_{x,rockerL} &= -P_x - Q_x + T_x = m_{rocker}\ddot{x}_{rockerL} \\
\Sigma F_{z,rockerL} &= -P_z - Q_z + T_z = m_{rocker}\ddot{z}_{rockerL} + m_{rocker}g \\
\Sigma M &= -\Delta_{EA}^zP_x + \Delta_{EA}^xP_z - \Delta_{ED}^zT_x + \Delta_{ED}^xT_z + Mg\Delta_{ED}^x = I_R'\ddot{\theta}_L
\end{aligned} \tag{5.4}$$

And when Eq. 5.4 is extended to the whole PATRo model, we can get a linear equation in the form of $Ax=b$ as follows. A matrix is a matrix determined by instantaneous kinematic configuration of the four tracks, which can be obtained from the kinematic analysis results of Chapter 5.3.1. Zero elements in the matrix A are omitted in Eq. 5.5. x is the unknown vector with 18 elements consisting of four traction forces, four normal forces, and 10 internal forces between the links. b vector includes the linear and angular acceleration terms of the links, which can be obtained by numerical differentiating the position and posture of each links.

Therefore, the optimal torque distribution problem (to minimize the maximum value of the required friction coefficient) can be formulated as follows.

$$\arg. \min_{N_{RL}, N_{RR}} . \max \left(\frac{\tilde{x}_{(1)}}{\tilde{x}_{(5)}} \quad \frac{\tilde{x}_{(2)}}{N_{RL}} \quad \frac{\tilde{x}_{(3)}}{\tilde{x}_{(6)}} \quad \frac{\tilde{x}_{(4)}}{N_{RR}} \right) \quad (5.8)$$

Now, it is finally ready to calculate the objective function $\mu_{\max}^*(X)$ when X is given. For example, at the initial value of the design variables (X_0), $\mu^*(i)$, which is the profile of minimized required friction coefficient is depicted in Fig. 5.13 That is, at the initial design variable, the objective function μ_{\max}^* is 0.24, and our next goal is to find design variables X that minimize this μ_{\max}^* .

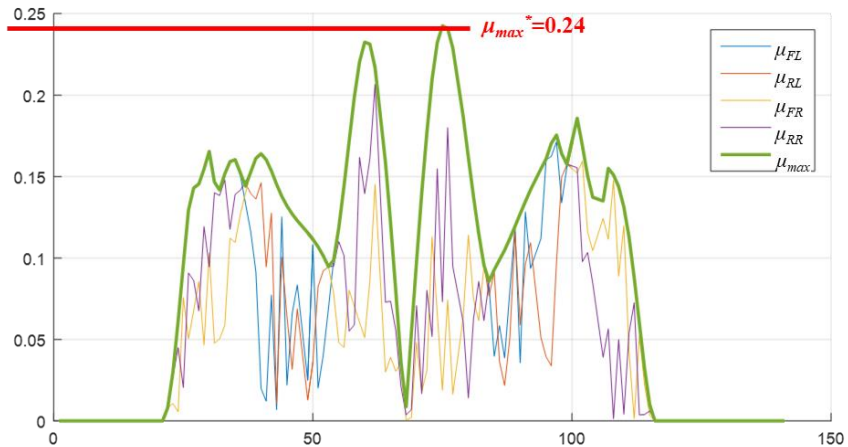


Fig. 5.13 Example of a result of optimal torque distribution (at initial values of design variables)

5.4. Design parameter optimization

5.4.1. Sensitivity analysis

Prior to optimization, sensitivity analysis is performed using level average analysis. The results are shown in Figure 5.14 and Table 5.3. The results show that x_2 and x_3 have little sensitivity, compared to x_1 and x_4 . x_1 and x_4 with large sensitivity are length

parameters corresponding to the longitudinal direction (moving direction) of PATRo. On the other hand, x_2 and x_3 are length variables that are not longitudinal length parameters of PATRo. (x_2 is the lateral direction, and x_3 is the height direction.) This is because the test terrain and the driving scenario used in this study are purely straight trajectories. If the driving scenario included more curves and steering, x_2 and x_3 would have relatively large sensitivity. However, this study limited the driving scenarios to the straight trajectory on the unsymmetric wavy bump, since the structural characteristics and effectiveness can be shown well on the terrain. Therefore, based on the results of this sensitivity analysis, the two design variables of x_1 and x_4 are actually used as the final design variables.

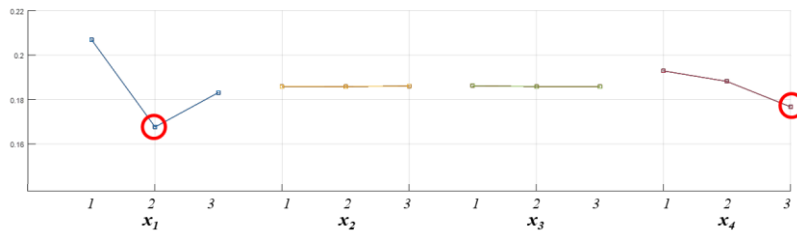


Fig. 5.14 Sensitivity analysis of the design variables

Table 5.3 Result of sensitivity analysis

y (μ)	x_1	x_2	x_3	x_4
Level 1	0.2069	0.1859	0.1862	0.1929
Level 2	0.1676	0.1858	0.1858	0.1881
Level 3	0.1832	0.1861	0.1857	0.1767
Maximum difference	0.0393	0.0003	0.0005	0.0162

5.4.2. Design parameter optimization with Taguchi methodology

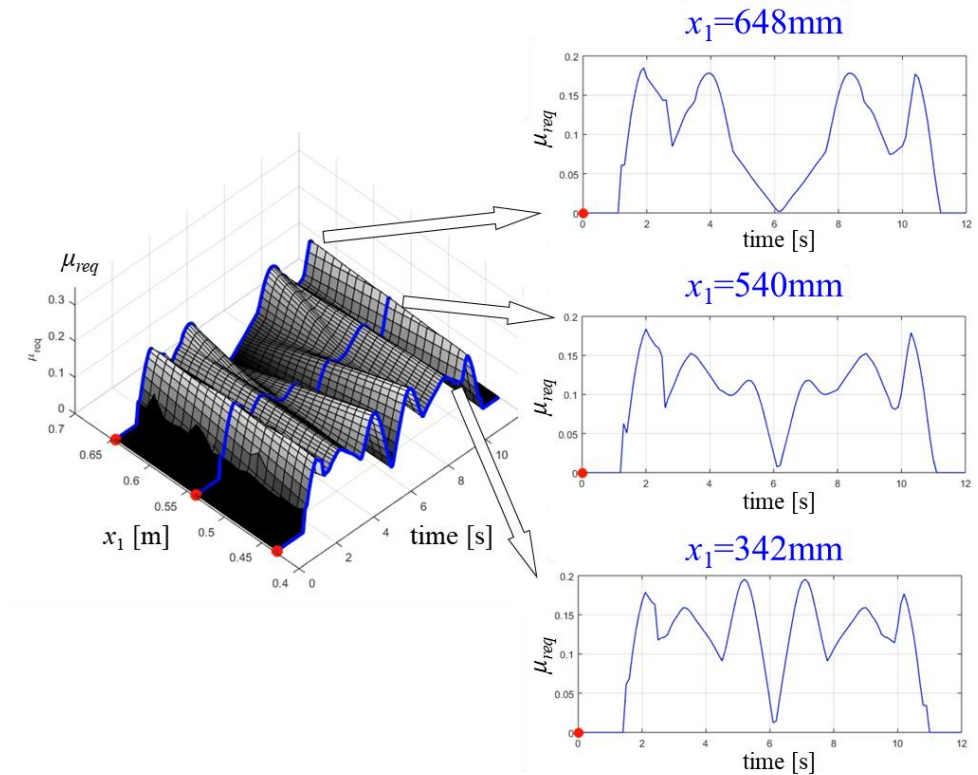


Fig. 5.15 Change of slip ratio profile according to the change of x_1

Prior to the design parameter optimization, a 3D graph in Fig. 5.15. is drawn in order to better understand the sensitivity analysis results. The x -axis of the 3D graph is the time axis, and the y -axis is the length of x_1 . And the z -axis is the value of the required friction coefficient at the corresponding x_1 length at the corresponding simulation time. PATRo models corresponding to total 21 discrete values of x_1 from 432 mm to 648 mm are generated, and the 21 different PATRo models were run on the test terrain. Then the 21 profiles of max. required friction coefficients obtained by kinetostatic analysis are merged 3D all together.

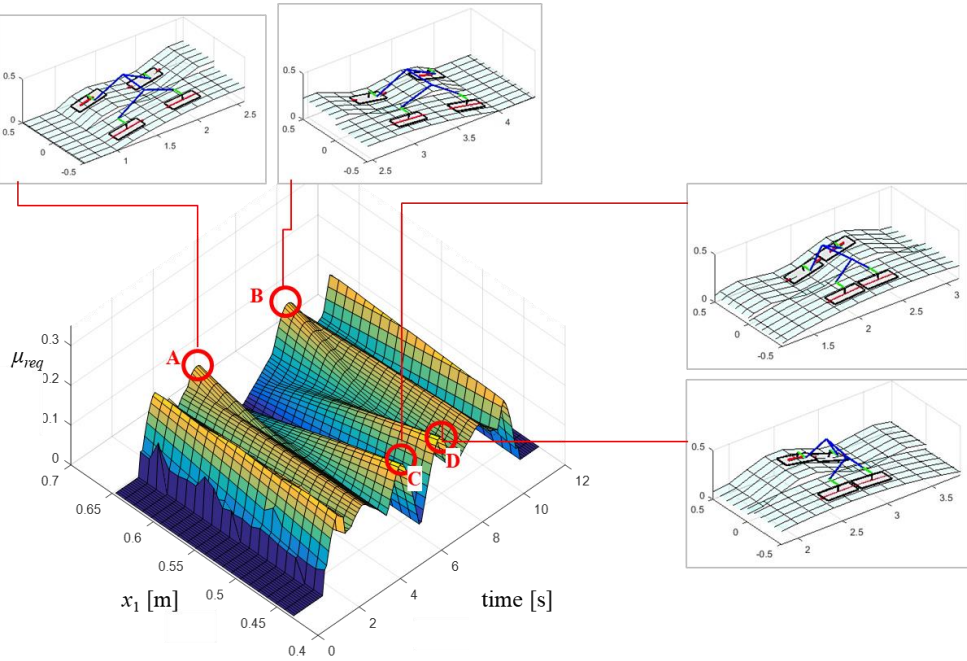


Fig. 5.16 Moments when the peak slip ratio occurs

On the other hand, A, B, C, and D in Fig. 5.16 are some of the moments when the max. required friction coefficient is peaking. If you look at the configuration of PATRo at these four moments, you can see that these four are the moment when the pitch angles of the four tracks become similar to each other. Also, it is trivial that the smaller the slope of the four tracks, the smaller the magnitude of the required friction coefficient. Therefore, a characteristic of required friction coefficient can be stated as follows.

- As the slopes of each drive track are similar to each other, the larger the required friction coefficient.
- The larger the slope at that time, the larger the required friction coefficient.

Therefore, in order to reduce the required friction coefficient, the slope of each track should not be similar, and the slope at the most similar moment should be small. If the terrain has the shape of a sinusoidal function graph like the test terrain of this study, it can be expected that x_l should have a length corresponding to half the length of the terrain wavelength. This is because in this condition, the front track and the rear track always have opposite phases and

therefore have a slope with the opposite sign. It can also be predicted that the larger x_4 is, the better. This is because the drive tracks will not be too sensitive to the local roughness of the terrain, at the larger size of x_4 .

Now let's move on to the design optimization stage. Taguchi methodology is used for the design parameter optimization. Total three times of Taguchi optimization were conducted. L_{27} , L_{25} , and L_{25} orthogonal arrays are used for the first, second, and third Taguchi analysis, respectively. Considering the constraints, the optimization results are as follows.

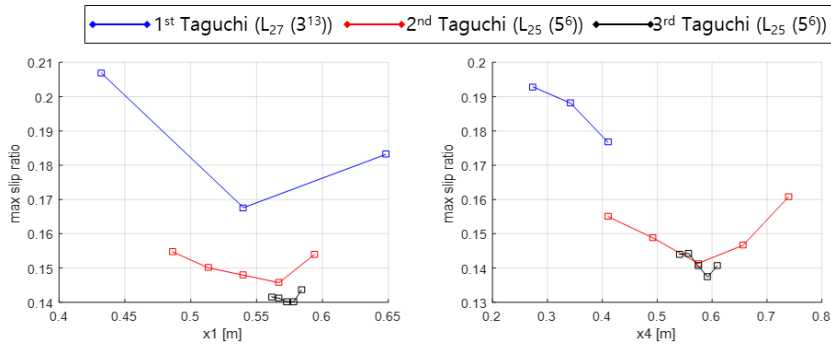


Fig. 5.17 Results of three times of Taguchi optimization

Table 5.4 Result of design optimization

description		initial value	optimal value
x_1	Distance between lateral center lines of front tracks and rear tracks	540 mm	594 mm (10% ▲)
x_2	Distance between longitudinal center lines of left tracks and right tracks	-	-
x_3	Vertical length of rocker link	-	-
x_4	Track length (contact length)	342 mm	445 mm (30% ▲)
objective function R_{max}		0.174	0.136 (21.77% ▼)

5.4.3. Verification of the optimization result

The optimization result is confirmed by 3D dynamics simulation. In other words, we checked whether the optimal design through kinetostatic analysis is actually leads to an improvement in terrainability and maneuverability as intended. Below is an illustration of the initial and optimal design of the PATRo, implemented in DAFUL.

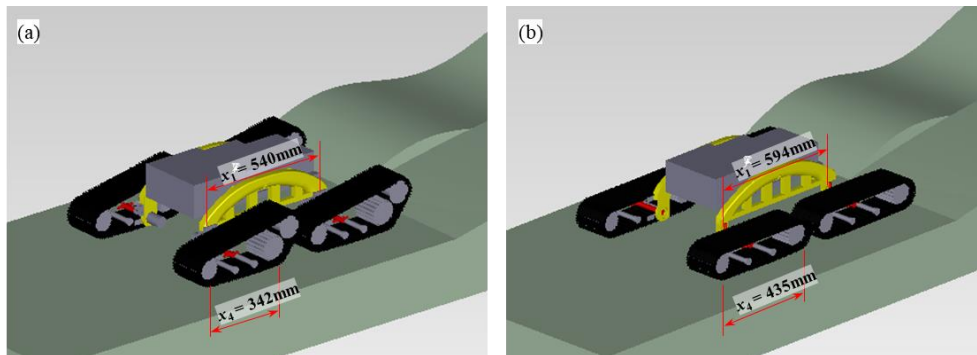


Fig. 5.18 Verification of optimization results using dynamics simulation

As the result of simulation, required torques at initial design and optimal design are compared in Fig. 5.19, and trajectory tracking error are compared in Fig. 5.20. Terrainability values were 13.06Nm and 11.32Nm at initial design and optimal design, respectively. The required torque is reduced by 13.3% by the optimization. Also, maneuverability values were 27.1mm and 25.5mm in initial design and optimal design, respectively, so the magnitude of trajectory tracking error is decreased by 5.9% through optimization.

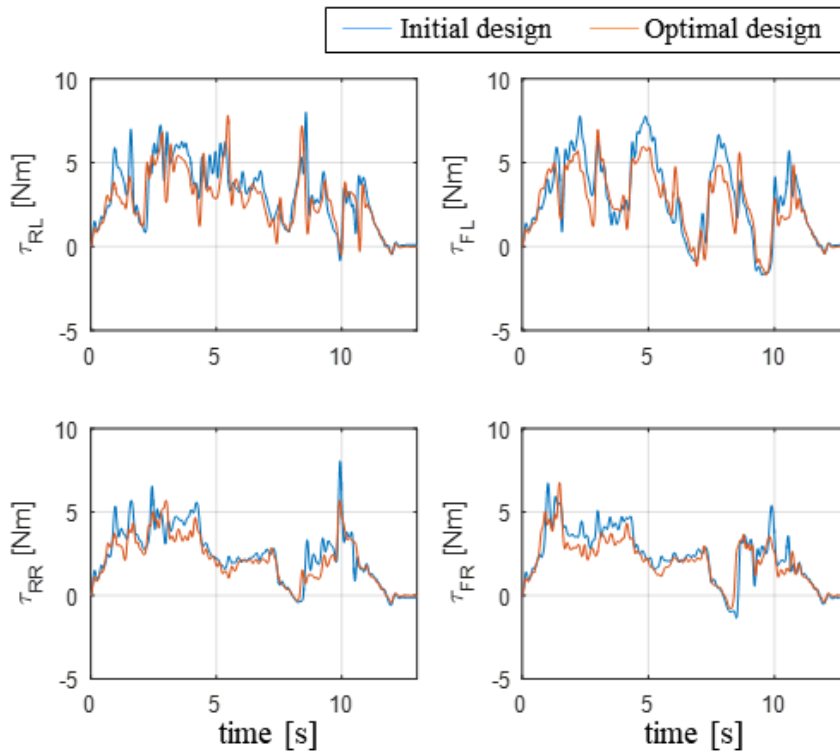


Fig. 5.19 Change of terrainability before and after optimization

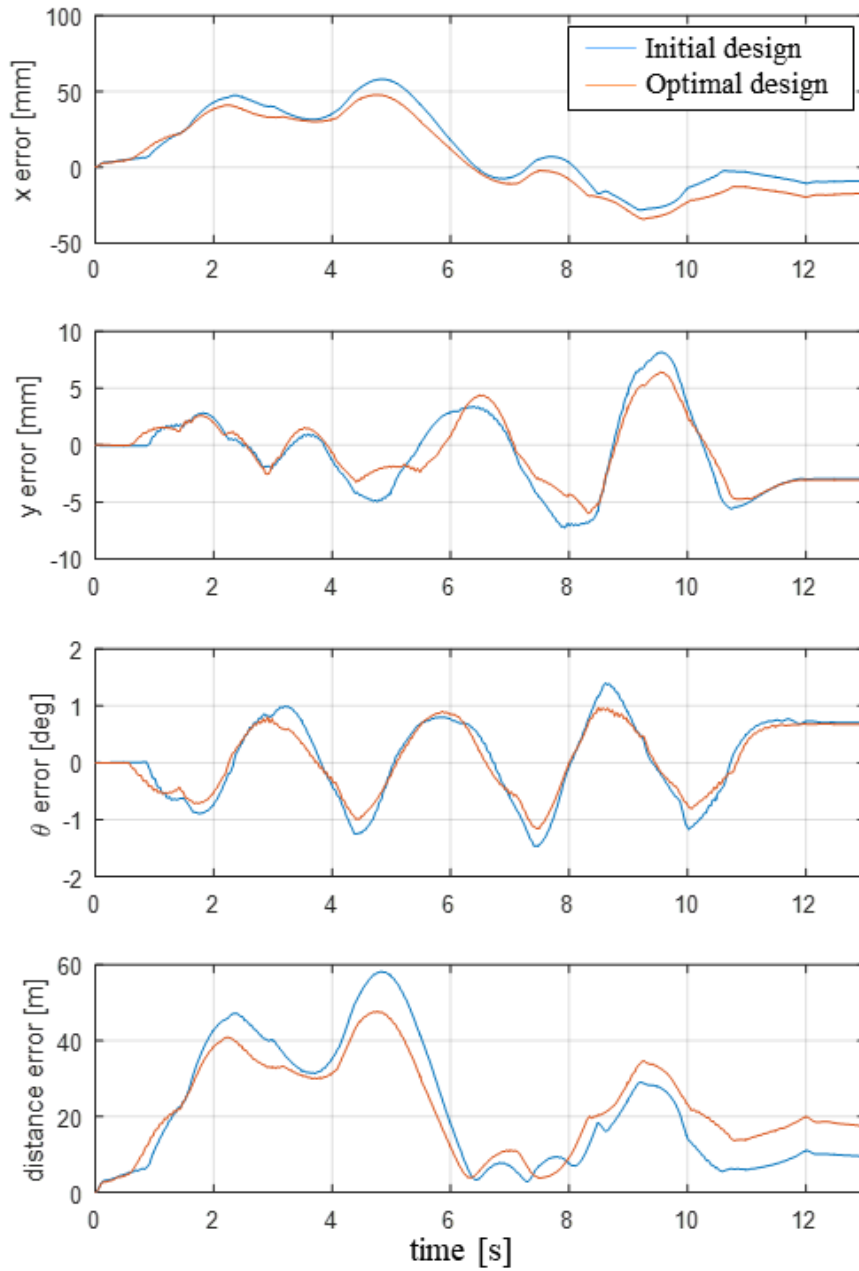


Fig. 5.20 Change of maneuverability before and after optimization

Based on the simulation result, the optimal version of the prototype was designed as in Fig. 5.21, with the changed length of rocker and changed length of the track.

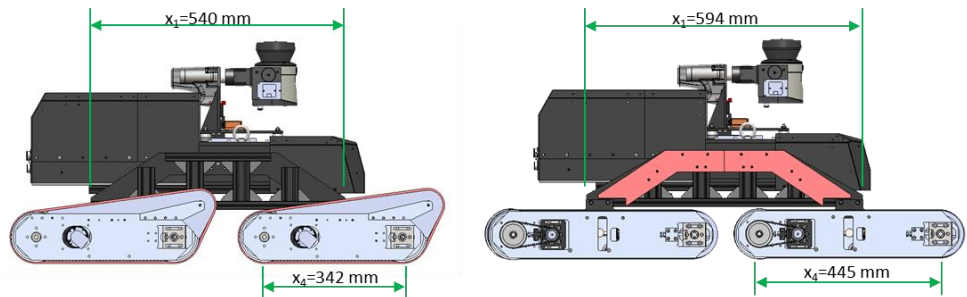


Fig. 5.21 Initial and optimal versions of PATRo prototype

Chapter 6. Manufacturing of PATRo prototype

6.1. Mechanical configuration of PATRo

This chapter introduces the specific mechanical structure of the prototype of PATRo. Fig. 6.1 shows which subsystems the PATRo prototype consists of and where the major component parts are located. As described above, PATRo consists of four drive tracks, two lockers, and a body. And as in figure, the main body consists of a base frame, a differential gear box module, a battery module, an electronic parts module, and a Lidar module. How each subsystem is configured is described in the following sub-chapters.

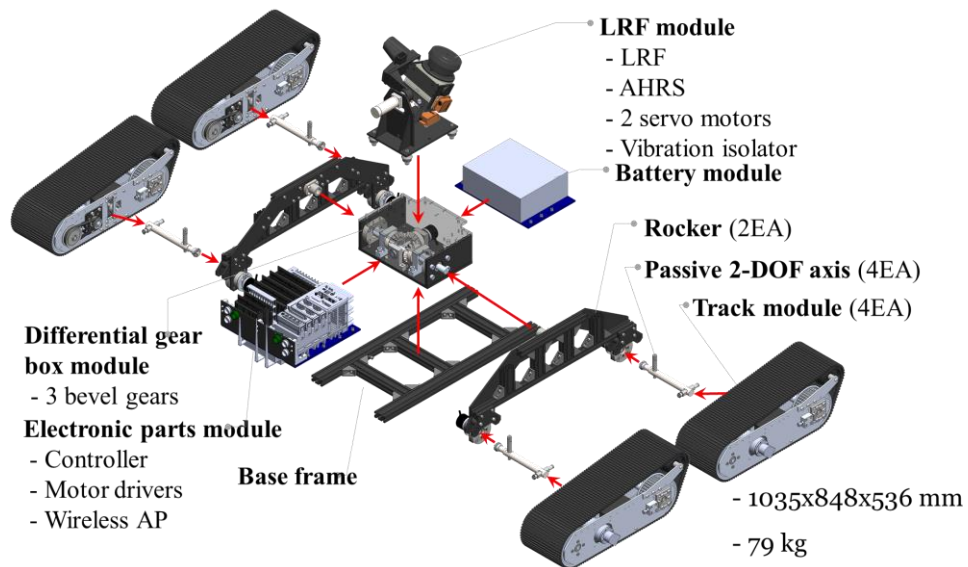


Fig. 6.1 Mechanical configuration of PATRo prototype

6.1.1. Driving tracks

Driving tracks are produced as shown in Fig. 6.2(a). The reason why I did not use off-the-shelf tracks, was that it was difficult add roll degree-of-freedom to the commercially available tracks. Empty space for the roll shaft and bearing holders were required inside the track, so the driving tracks for PATRo were designed as in Fig. 6.2(b). As shown in Fig. 6.2(c), a super torque timing belt (S8M) was used as the caterpillar track. A stretchable 5mm thick latex was bonded to the outer surface of the timing belt,

to make the outermost surface of the drive track more protruding than the sprocket flange. The drive motor torque is transmitted to the drive track through another timing belt (S5M). To adjust the tension of the two timing belts, two tensioners are used, respectively.

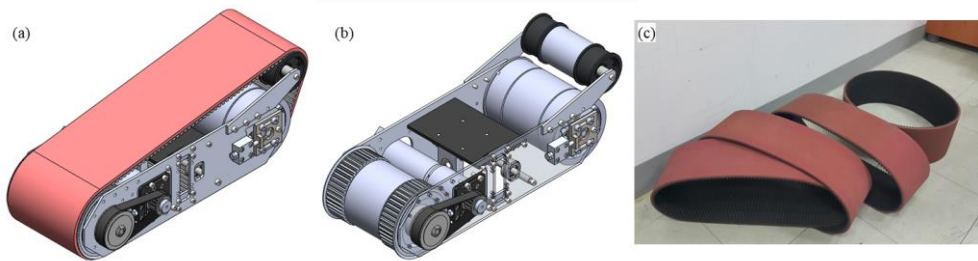


Fig. 6.2 Track assemblies in the PATRo prototype

6.1.2. 2-DOF passive joints

As shown in the Fig. 6.3, 2-DOF passive joints for pitch-roll motion of each drive track were produced. At the passive joints, pitch axis is connected to the rocker, and roll axis is connected to the inside of the track. Also, rubber stoppers are installed on rockers and tracks for the joint limits. These joint limits are designed to allow several options for the magnitude of joint limits to be chosen according to the operating environment of PATRo. There are three roll limit options: 10, 15, and 20 degrees. The pitch limit has 8 options: ranges from 5 to 40 degrees at 5 degree intervals.

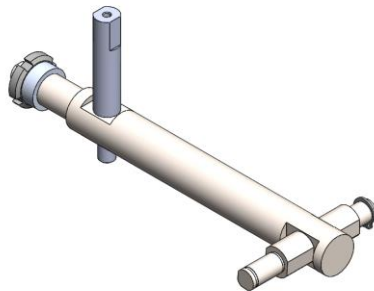


Fig. 6.3 2-DOF passive joint in the PATRo prototype

6.1.3. Rocker links with differential joint

As in Fig. 6.4(c), the two rockers (Fig. 6.4(a)) are connected to the body via differential gears (3 bevel gears, Fig. 6.4(b)). Thus, as in Fig. 6.4(d), the pitch angle of the body takes a median value of the pitch angles of the two rockers. In other words, the angular positions of left rocker joint and right rocker joint are equal in magnitude and opposite in sign. In the differential joint gearbox module, an encoder is installed for measuring the angular displacement of the rocker joint.

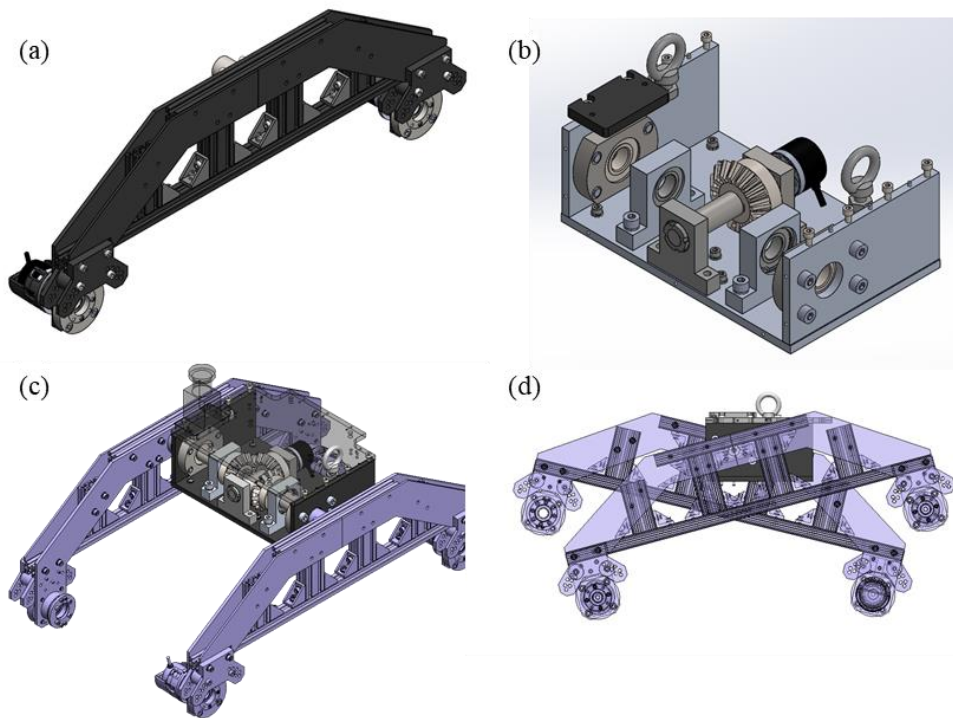


Fig. 6.4 Rockers and differential joint in PATRo prototype

6.1.4. Lidar module for PATRo localization

The lidar module is used for localization of the platform during trajectory tracking experiments, and the module consists of a 2D lidar, an AHRS, and two servo motors. While PATRo is running on a rough terrain, the orientation of the lidar sensor can be stabilized by two servo motors, using the orientation data of the platform

obtained by the AHRS. This makes it possible to estimate the instantaneous posture of the platform, by reading the wall profiles around the experimental environment. Lidar orientation control, and localization algorithm will be discussed in detail in Chapter 6.

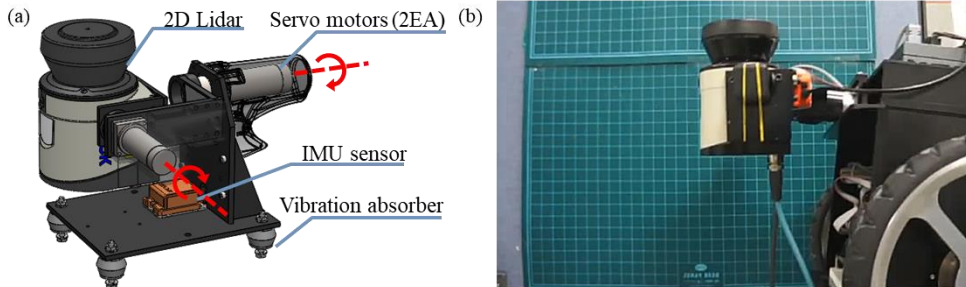


Fig. 6.5 (a) Lidar module in the PATRo prototype, (b) orientation stabilization of the Lidar module

6.1.5. Control box and battery

PATRo is equipped with a battery and a control box, so it can be operated completely wirelessly. The control box includes a real-time controller, motor drivers, power stabilizer, emergency stop switch, and mobile AP for communication with the host PC. The battery requires max. Considering the required power of the track drive motors, a 24V 41.6Ah lithium ion battery was used so that PATRo can be operated for 1 hour under the condition of maximum continuous current (10.8A) flowing to four drive motors.

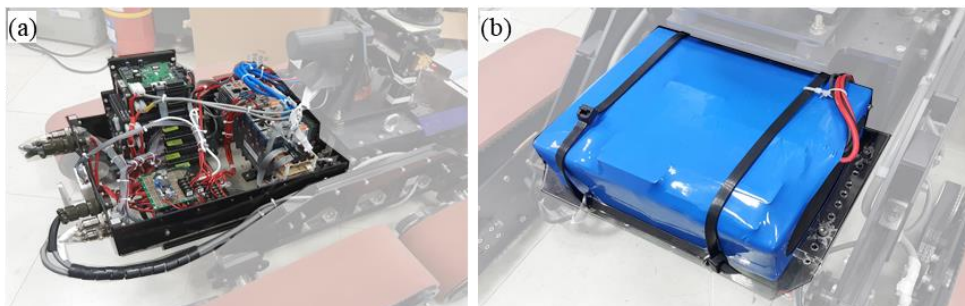


Fig. 6.6 (a) Control box and (b) battery in the PATRo prototype

6.2. Electrical configuration of PATRo and operation software

The controller, sensors, and actuators used in PATRo and their connections are shown in Fig. 6.7. First, National Instruments' CompactRIO 9033, a real-time controller, is a high-performance industrial embedded controller, featuring a 1.33GHz dual-core CPU and programmed with LabVIEW FPGA. This allows PATRo to drive actuators with no time delay using sensor feedback data such as 2D Lidar, AHRS, and encoders. The control period of PATRo is 20 ms.

Two inertial sensors were used. One inertial sensor is installed on the PATRo body to measure the instantaneous orientation of the body, which is used for Lidar orientation stabilization. Another inertial sensor is not required but is additionally installed, which is attached to the Lidar sensor. This was used to verify Lidar's orientation control performance. Two inertial sensors provide Euler angle and angular velocity to the controller using RS232 communication.

There are a total of 11 encoders. The A/B phase signals of each of the eleven encoders are input to the controller via the digital input module. The 2D lidar data is also input to the controller via TCP/IP protocols.

Also, there are a total of six motor drivers for four track drive motors and two lidar module motors, which control the position and velocity of the motors in accordance with commands from the host controller, which is done by CAN communication.

Finally, a wireless AP (access point) is installed in the Ethernet port of the controller. The host PC (laptop) can access the Wi-Fi created by the wireless AP, enabling the operator to manually control the PATRo or respond to an emergency situation.

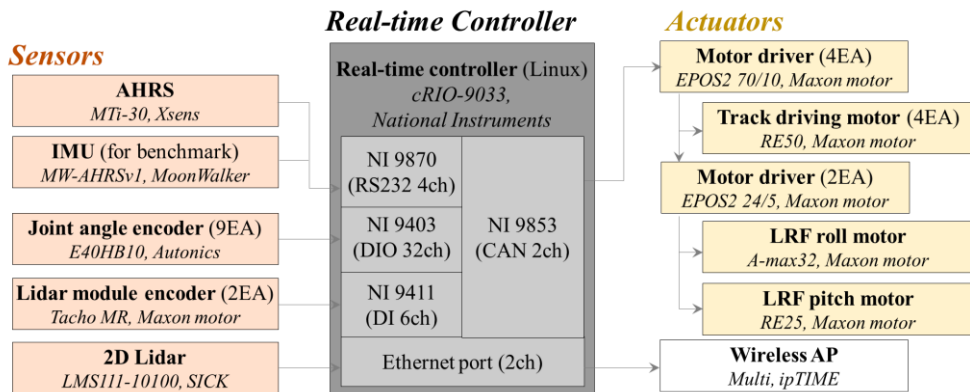


Fig. 6.7 Electrical configuration of the PATRo prototype

Fig. 6.8 shows the snapshot of the user interface of the control front panel, which is programmed by using Labview from National Instrument.

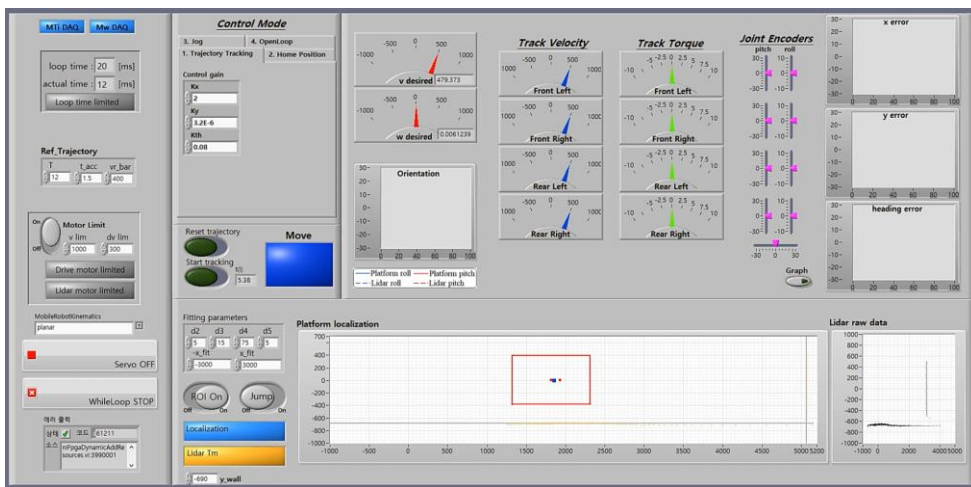


Fig. 6.8 Control front panel and user interface of PATRo.

Chapter 7. Experiment and result

7.1. Experimental setup

Fig. 7.1 shows the experimental environment for reference trajectory tracking control of the PATRo platform. As shown in figure, the experimental environment consists of not only PATRo platform and the terrain, but also 2-DOF Lidar module and the walls, which are required for real-time localization of the platform. In this chapter, experimental environment and experimental methods are introduced in detail.

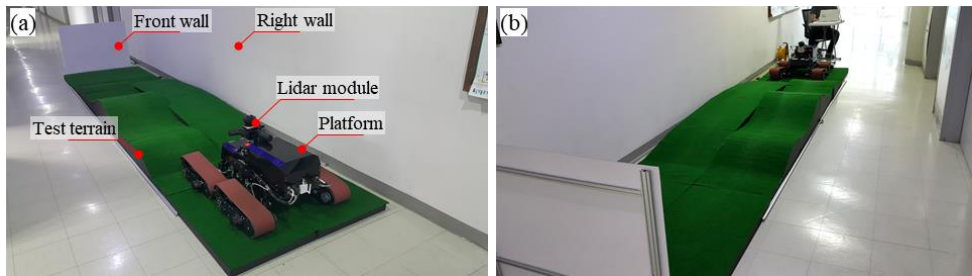


Fig. 7.1 Experimental setup for the reference trajectory tracking control of a platform on the rough terrain

7.1.1. Fabrication of unsymmetric wavy bump

Unsymmetric wavy bump, the test terrain, is fabricated as shown in Fig. 7.2. The unsymmetric wavy bump can be separated into 12 pieces for easy installation, disassembly, movements and storage. Each piece was made by processing high density styrofoam. In order to assemble the 12 blocks, aluminum profile frame is used to connect all the blocks. Tartan turf and masking tape were used to protect the surface of the blocks from repeated experiments.

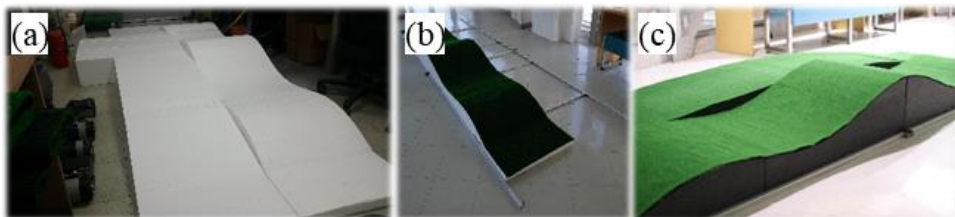


Fig. 7.2 Fabrication process of the unsymmetric wavy bump

7.1.2. Localization based on 2D Lidar module and the walls

In this study, we solved this localization problem by using 2D Lidar sensor installed on a 2-DOF module. 2D Lidar is a two-dimensional laser sensor capable of obtaining distance data of objects placed on the horizontal plane of the sensor. It is widely used in the field of autonomous vehicles and mobile robots with SLAM function. Especially, when the platform runs over rough terrain, then the orientation of the mobile robot is not stable, but the 2D Lidar sensor should keep stable orientation for the localization. Thus, the proposed 2-DOF 2D Lidar module is able to stabilize the orientation of the Lidar so that it always maintains horizontal orientation. As shown in Fig. 7.2, the 2D Lidar sensor on the platform recognizes the specific stationary objects (the front wall and the right wall in this system). Then the platform is able to measure its relative posture from the specific objects.

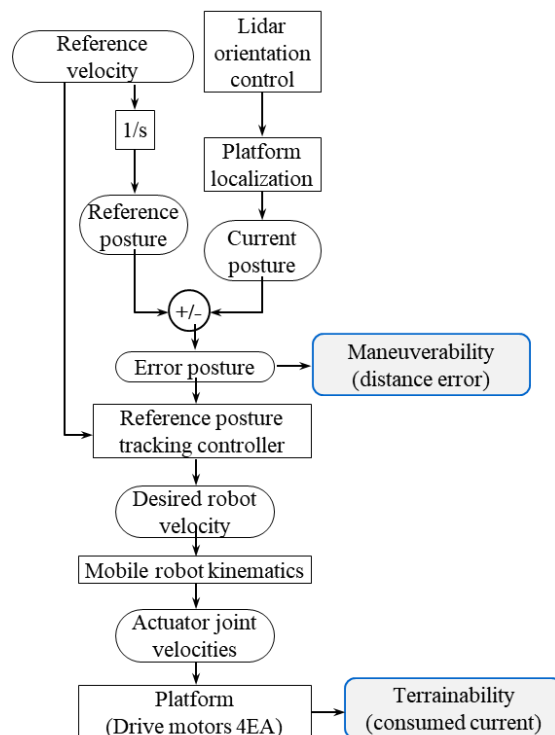


Fig. 7.3 Overall system configuration for the experimental methods of the evaluation

Fig. 7.3 shows the system configuration diagram for realizing the evaluation method of Ch. 3 in the experimental environment. The experimental evaluation method is described in the following sub-chapters. Ch. 7.1.2.1 presents a 2-DOF 2D Lidar module for orientation stabilization, and Ch. 7.1.2.2 presents a platform localization algorithm using the Lidar data.

7.1.2.1. 2-DOF 2D Lidar module for orientation stabilization

The Lidar module is used for localization of the platform during trajectory tracking experiments, and the module consists of a 2D Lidar, an AHRS, and two servo motors. While the platform is running on a rough terrain, the orientation of the Lidar sensor can be stabilized by two servo motors, using the orientation data of the platform obtained by the AHRS. This makes it possible to estimate the instantaneous posture of the platform, by reading the wall profiles around the experimental environment.

In order to maintain the desired orientation of the Lidar at all times, the roll and pitch axis of the module should be manipulated to counteract the effects of the disturbances such as the variations of the slope and roughness of driving terrains. Since the orientation output from an AHRS is generally known to have sensor drifts, the reference input is set to be the instantaneous angular velocity, not the orientation. For example, according to the technical document [39] of the AHRS used in this system, the AHRS contains the orientation drifts of 2.0-deg in roll and pitch and 1.0-deg in yaw (heading) over a period of 60-min. Thus, the angular velocity-based orientation controller is designed as below. The desired angular velocities of the roll and pitch motors, are obtained by mapping the desired angular velocity and current angular velocity difference of the Lidar, onto the joint velocities of the roll and pitch motors. In addition, in order to deal with the tracking error of the motors, the resultant angular positions are fed back for comparison with the desired angular positions; the angular position tracking errors in the roll and pitch motors will then be calculated.

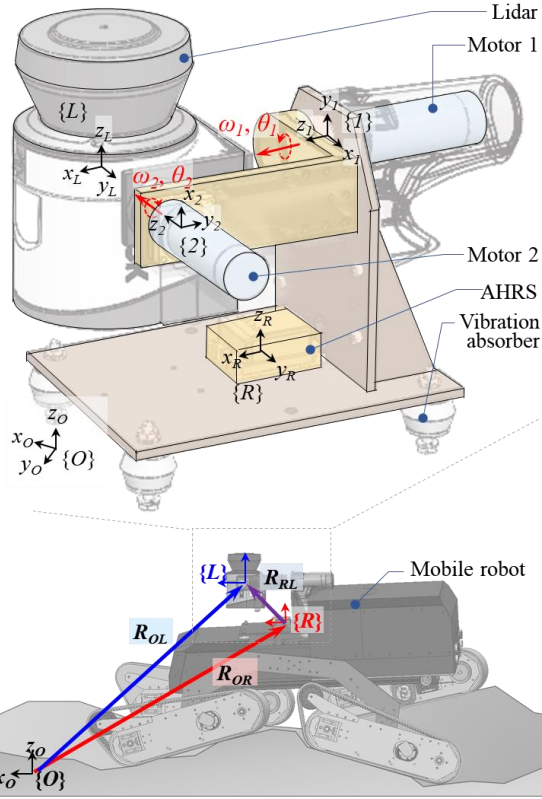


Fig. 7.4 Mechanical structure of the 2-DOF Lidar module and the coordinate frames, orientation matrices assigned to the system

Fig. 7.4 shows the coordinate frames and orientation matrices assigned to the Lidar module system. Let $\{O\}$ be the spatial coordinate frame which is the same as the inertial coordinate frame. The body coordinate frame denoted as $\{R\}$ is attached to the origin of the AHRS installed on the mobile robot. The orientation output of the AHRS is measured with respect to $\{L\}$ and expressed in terms of the ZYX Euler convention. RRL describes the orientation of $\{L\}$ relative to $\{R\}$. In this research, RRL is represented in the form of the POE formula as follows:

$$R_{OR}(\theta_1, \theta_2, \theta_3) = e^{\hat{\omega}_1 \theta_1} e^{\hat{\omega}_2 \theta_2} e^{\hat{\omega}_3 \theta_3} R_{OR}(0) \quad (7.1)$$

where $\omega_i \in \mathbb{R}^3$ is a unit vector specifying the rotation axis expressed in $\{S\}$, $\hat{\omega}_i \in \mathbb{R}^{3 \times 3}$ is the skew-symmetric matrix of $\omega_i \in \mathbb{R}^3$,

and θ_i is the angle of each rotation in radians. According to the ZYX Euler convention, ω_1 , ω_2 , and ω_3 represent the z-axis, y-axis, and x-axis, respectively, and θ_1 , θ_2 , and θ_3 represent yaw (α_R), pitch (β_R), and roll (γ_R) angles, respectively. In this paper, the term ‘heading’ is sometimes used as the meaning of ‘yaw’. In this case, the home position $R_{OR}(0)$ is set to be identical to identity matrix $I_{3 \times 3}$. $\{L\}$ denotes the coordinate frame attached to the origin of the Lidar. R_{RL} refers to the orientation of $\{L\}$ relative to $\{R\}$. Then, the rigid motion associated with rotating about the axis of rotation ω_i is given by the following equation.

$$R_{RL}(\theta_4, \theta_5) = e^{\hat{\omega}_4 \theta_4} e^{\hat{\omega}_5 \theta_5} R_{RL}(0) \quad (7.2)$$

where ω_4 and ω_5 denote unit vectors specifying the first and second axes of the rotations of the 2-DOF module at its home positions. The 2-DOF module is designed so that the roll and pitch axes coincide with the x-axis and negative y-axis of $\{R\}$, respectively, so it can be stated that $\omega_4 = [1 \ 0 \ 0]^T$, $\omega_5 = [0 \ -1 \ 0]^T$. Since $R_{RL}(0)$ is equal to the identity matrix $I_{3 \times 3}$, the function of R_{OL} can be obtained as follows:

$$\begin{aligned} R_{OL}(\theta_1, \theta_2, \theta_3, \theta_4, \theta_5) &= R_{OR}(\theta_1, \theta_2, \theta_3) R_{RL}(\theta_4, \theta_5) \\ &= e^{\hat{\omega}_1 \theta_1} e^{\hat{\omega}_2 \theta_2} e^{\hat{\omega}_3 \theta_3} e^{\hat{\omega}_4 \theta_4} e^{\hat{\omega}_5 \theta_5} \end{aligned} \quad (7.3)$$

In other words, Eq. (7.3) represents the relationship between the Lidar’s orientation and other sensor outputs: AHRS outputs (α_B , β_B , and γ_B) and motor encoder outputs (θ_4 , θ_5).

Also, the AHRS describes how the mobile robot is rotating in space by reporting the instantaneous angular velocity denoted as $\omega_{OR}^R \in \mathbb{R}^3$. In this case, the body angular velocity $\omega_{OR}^R \in \mathbb{R}^3$ describes the instantaneous angular velocity of $\{B\}$ with respect to the instantaneous $\{B\}$.

In order to derive the control rule, it is necessary to find the

relationship between the orientation matrix and the angular velocity. The instantaneous angular velocities ω_{st}^s can be represented as in the following Eq. (7.4).

$$\hat{\omega}_{OL}^o = \dot{R}_{OL}(t)R_{OL}^T(t) \quad (7.4)$$

Substituting R_{OL} from Eq. (7.3), we get Eq. (7.5), which is the skew-symmetric form of the instantaneous $\{L\}$ relative to $\{O\}$.

$$\hat{\omega}_{OL}^o = \dot{R}_{OL}R_{OL}^T = \sum_{i=1}^5 \left(e^{\hat{\alpha}_i \theta_i} \dots e^{\hat{\alpha}_{i-1} \theta_{i-1}} (\hat{\omega}_i) e^{-\hat{\alpha}_{i-1} \theta_{i-1}} \dots e^{-\hat{\alpha}_i \theta_i} \dot{\theta}_i \right) \quad (7.5)$$

Removing the skew-symmetric operator from both sides of Eq. (7.5), we get Eq. (7.6), in the general form of expressing the relationship between the end-effector velocity and the joint velocities using the Jacobian matrix.

$$\omega_{OL}^o = J_{OL}^o(\theta) \cdot [\dot{\alpha}_B \quad \dot{\beta}_B \quad \dot{\gamma}_B \quad \dot{\theta}_4 \quad \dot{\theta}_5]^T \quad (7.6)$$

where $J_{OL}^o(\theta): \mathbb{R}^5 \rightarrow \mathbb{R}^3$ is a configuration-dependent matrix that maps the joint velocities to end-effector velocities, and is expressed as follows:

$$J_{OL}^o = \begin{bmatrix} z & e^{\hat{z}\alpha_R} y & e^{\hat{z}\alpha_R} e^{\hat{y}\beta_R} x & e^{\hat{z}\alpha_R} e^{\hat{y}\beta_R} e^{\hat{x}\gamma_R} x & -e^{\hat{z}\alpha_R} e^{\hat{y}\beta_R} e^{\hat{x}\gamma_R} e^{\hat{x}\theta_4} y \end{bmatrix} \quad (7.7)$$

However, this equation contains the time derivatives of Euler angles of the mobile robot ($\dot{\alpha}, \dot{\beta}, \dot{\gamma}$). Since these time derivatives are not provided by the AHRS, numerical differentiation of the Euler angles can be considered, but this method accompanies the possibility of numerical errors accumulation. Thus Eq. (7.7) is rearranged as follows to avoid this problem.

First, the right hand side of Eq. (7.7) can be divided into two

parts as follows: angular velocity occurred by mobile robot orientation change, and angular velocity occurred by the 2-dof module motor movements.

$$\begin{aligned} \omega_{OL}^O = & \begin{bmatrix} z & e^{\hat{z}\alpha_R} y & e^{\hat{z}\alpha_R} e^{y\beta_R} x \end{bmatrix} \cdot \begin{bmatrix} \dot{\alpha}_R \\ \dot{\beta}_R \\ \dot{\gamma}_R \end{bmatrix} \\ & + e^{\hat{z}\alpha_R} e^{y\beta_R} e^{x\gamma_R} \begin{bmatrix} x & -e^{x\theta_4} y \end{bmatrix} \cdot \begin{bmatrix} \dot{\theta}_4 \\ \dot{\theta}_5 \end{bmatrix} \end{aligned} \quad (7.8)$$

In Eq. (7.8), we can find that the first part of the right hand side represents the instantaneous angular velocity of base coordinate frame {R} expressed in spatial coordinate frame {O}. Thus we can replace this part with angular velocity term ω_{OR}^O , or $R_{OR}\omega_{OR}^R$, which is given by the AHRS. It is better to use this raw output data instead of using numerical time derivatives of Euler angles since it can avoid numerical differentiation errors. The second part of the right hand side in Eq. (7.8) is a multiplication of rotation matrix of {R} relative to {O}, and angular velocity of tool coordinate frame {L} expressed in {R}. Thus Eq. (7.8) can be represented as follows.

$$\omega_{ST,c}^S = R_{SB}\omega_{SB}^B + R_{SB}J_{BT}(\theta_4) \begin{bmatrix} \dot{\theta}_4 \\ \dot{\theta}_5 \end{bmatrix} \quad (7.9)$$

Except motor control inputs $(\dot{\theta}_4, \dot{\theta}_5)$, all other variables in right hand side of Eq. (7.9) are known values which can be obtained from the sensors; R_{SB} and ω_{SB}^B from AHRS and θ_4 from motor encoder. Therefore, Eq. (7.9) represents the relationship between the Lidar's angular velocity and the motor speeds at certain configuration of mobile robot and the Lidar module. The letter c in the subscript of left hand side stands for *current*.

For orientation control of the Lidar, the desired angular velocity of the Lidar will only be the heading rate of the mobile robot as represented in Eq. (7.10). Subscript d in the angular velocity stands for *desired*.

$$\omega_{ST,d}^S = z\dot{\alpha}_B \quad (7.10)$$

Lastly, to match the current angular velocity to desired value, we get Eq. (7.11) from fusing current angular velocity (7.9) and desired angular velocity (7.10).

$$\begin{bmatrix} \dot{\theta}_4 \\ \dot{\theta}_5 \end{bmatrix} = (R_{SB} J_{BT}(\theta_4))^\dagger \begin{bmatrix} 0 \\ 0 \\ \dot{\alpha}_B \end{bmatrix} - R_{SB} \omega_{SB}^B \quad (7.11)$$

As stated in the beginning of Chapter, if the control algorithm uses only the mobile robot angular velocity without any other feedback data, the error factors such as the motor tracking error would intactly appear at the Lidar orientation output. In order to match the current orientation of the Lidar to meet the desired orientation, the above control algorithm is augmented with orientation compensating terms. For stable orientation control, the desired orientation matrix of Lidar is the rotation matrix along z -axis about heading angle α of the mobile robot.

$$R_{ST,d} = e^{\hat{z}\alpha_B} \quad (7.12)$$

With combining current Lidar orientation Eq. (7.3) and desired Lidar orientation Eq. (7.12), we get Eqs. (7.13) and (7.14). $\theta_{4,d}$ and $\theta_{5,d}$ in Eq. (7.14) are the desired angular positions of 2-dof module motors for matching the current orientation to the desired value. Note that the desired positions are very simple on account of the order of joints from the ZYX convention of Euler angles and RP-module structure: z , y , x , x , and $-y$. Two adjacent rotations along x -axis are cancelled each other, and next two rotations along y -axis are cancelled sequentially.

$$e^{\hat{\alpha}_1\theta_1} \left(e^{\hat{\alpha}_2\theta_2} e^{\hat{\alpha}_3\theta_3} e^{\hat{\alpha}_4\theta_4} e^{\hat{\alpha}_5\theta_5} \right) = e^{\hat{z}\alpha_B} \quad (7.13)$$

$$\begin{bmatrix} \theta_{4,d} \\ \theta_{5,d} \end{bmatrix} = \begin{bmatrix} -\gamma_B \\ \beta_B \end{bmatrix} \quad (7.14)$$

Let motor position errors $\theta_{i,e}$ be the difference between the desired and the actual motor positions fed from the encoders, as follows.

$$\begin{bmatrix} \theta_{4,e} \\ \theta_{5,e} \end{bmatrix} = \begin{bmatrix} \theta_{4,c} \\ \theta_{5,c} \end{bmatrix} - \begin{bmatrix} \theta_{4,d} \\ \theta_{5,d} \end{bmatrix} = \begin{bmatrix} \theta_{4,c} + \gamma_B \\ \theta_{5,c} - \beta_B \end{bmatrix} \quad (7.15)$$

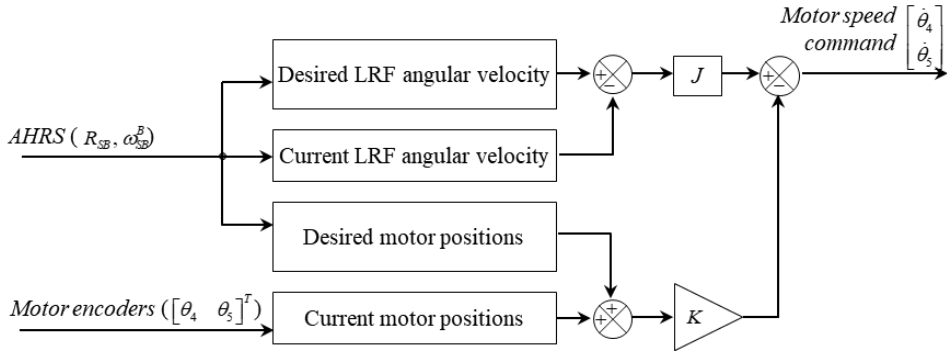


Fig. 7.5 Block diagram for the Lidar orientation control.

$$\begin{aligned} \begin{bmatrix} \dot{\theta}_4 \\ \dot{\theta}_5 \end{bmatrix} &= (R_{SB} J_{BT}(\theta_4))^{\dagger} \begin{bmatrix} 0 \\ 0 \\ \dot{\alpha}_B \end{bmatrix} - R_{SB} \omega_{SB}^B + K \begin{bmatrix} -\theta_{4,e} \\ -\theta_{5,e} \end{bmatrix} \\ &= (R_{SB} J_{BT}(\theta_4))^{\dagger} \begin{bmatrix} 0 \\ 0 \\ \dot{\alpha}_B \end{bmatrix} - R_{SB} \omega_{SB}^B + K \begin{bmatrix} -\theta_4 - \gamma_B \\ -\theta_5 + \beta_B \end{bmatrix} \end{aligned} \quad (7.16)$$

To compensate position errors in roll and pitch axes at every sampling time, the control algorithm becomes Eq. (7.16). K is the control gain. The overall control block diagram is depicted in Fig. 7.5. Please refer to the supplementary video [40] for the detailed results of the Lidar orientation control experiments.

7.1.2.2. PATRo localization algorithm

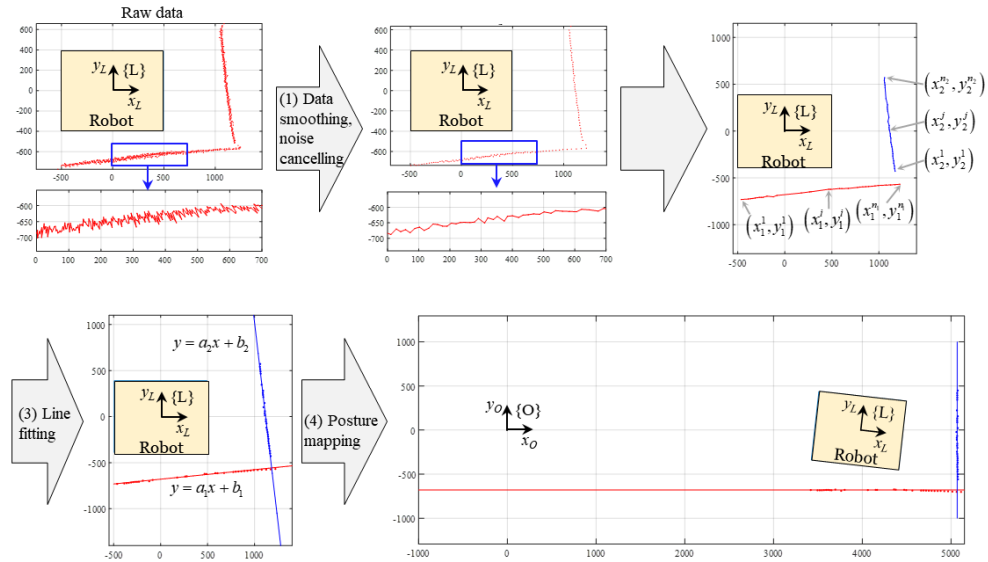


Fig. 7.6 Flow chart of the platform localization process

The localization algorithm in this study can be divided into four steps as follows.

1. Data smoothing: First, the raw data from the Lidar sensor is subjected to data smoothing and noise canceling. The five adjacent data are grouped together and their positions (x, y) are averaged. As a result, the number of data to be processed instantaneously is reduced at every moment, and the influence of the outliers whose positions are scattered due to sensor noise can be reduced.
2. Segment clustering: Plot the slope between adjacent points and detect the sections where the slope suddenly changes. That is, each interval section in which a similar slope is maintained is assumed to be a straight line. Under normal circumstances, two line segments should be detected: the front wall and the right wall. In Figure 7.6, these two segments are depicted as $(x_1^1, y_1^1) \dots (x_1^n, y_1^n)$, and $(x_2^1, y_2^1) \dots$

$(x_2^{n_2}, y_2^{n_2})$. (The number of points forming the first and second segments are n_1 and n_2 , respectively.)

3. Line fitting: Line fitting is performed based on the first order polynomial for each line segment. When the linear equation approximating two line segments is $y = a_k x + b_k$ ($k=1,2$), a_k and b_k can be obtained from the following equations.

$$a_k = \frac{n_k \sum_{i=1}^{n_k} x_i y_i - \sum_{i=1}^{n_k} x_i \sum_{i=1}^{n_k} y_i}{n_k \sum_{i=1}^{n_k} x_i^2 - \left(\sum_{i=1}^{n_k} x_i \right)^2} \quad (7.17)$$

$$b_k = \frac{\sum_{i=1}^{n_k} x_i^2 \sum_{i=1}^{n_k} y_i - \sum_{i=1}^{n_k} x_i \sum_{i=1}^{n_k} x_i y_i}{n_k \sum_{i=1}^{n_k} x_i^2 - \left(\sum_{i=1}^{n_k} x_i \right)^2} \quad (7.18)$$

4. Posture mapping: Find current posture $p_c = [x_c \ y_c \ \theta_c]^T$ of the platform that allows each line segment to be where it really should be. That is, through transformation that reflects the current posture, the first segment $y = a_1 x + b_1$ should become $y = 0 \cdot x - 680$ and the second segment $y = a_2 x + b_2$ should be $0 \cdot y = x - 5069$. (The front wall is 5069mm away from the origin of the inertial frame, and the right wall is 680mm away from

the origin.) Let $R = \begin{bmatrix} \cos \theta & -\sin \theta & x \\ \sin \theta & \cos \theta & y \\ 0 & 0 & 1 \end{bmatrix}$ be a matrix satisfying the above relation. Then, $[x \ y \ \theta]^T$ of the R becomes the current posture of the robot. x_c , y_c , and θ_c can be obtained from the following equation.

$$\theta_c = -\frac{1}{2} \left(\tan^{-1} a_1 + \tan^{-1} a_2 + \frac{\pi}{2} \right) \quad (7.19)$$

$$x_c = \frac{b_2}{\sin \theta_c + a_2 \cos \theta_c} \quad (7.20)$$

$$y_c = \frac{-b_1}{\cos \theta_c - a_1 \sin \theta_c} - 680 \quad (7.21)$$

Finally, when the robot and two walls are shown in an inertial frame as in Fig. 7.6, then the localization process is complete. The results of the localization on the rough terrain using this localization algorithm and the results of the posture tracking control experiment will be discussed in detail in Ch. 7.2.

7.2. Experimental results

7.2.1. Reference posture tracking control on the rough terrain

The reference posture tracking control experiment of the PATRo platform is conducted. Using the proposed Lidar module and localization algorithm, the robot is measuring its current posture in real time, and controls its track velocities to follow the straight trajectory. Fig. 7.7 is the snapshot of the experiment.

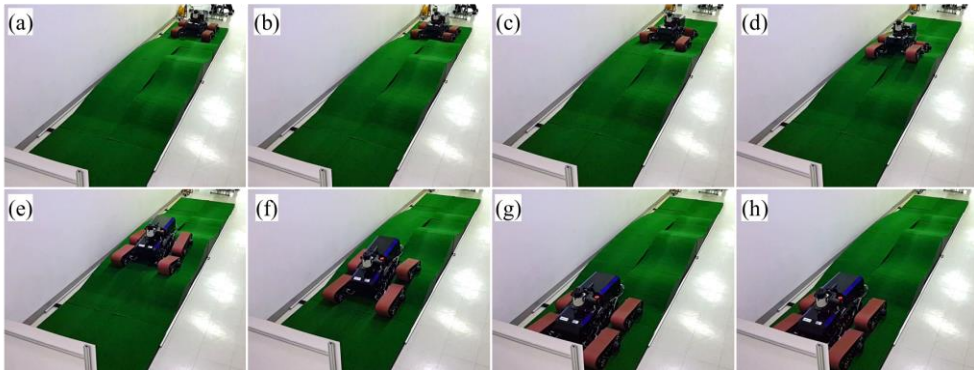


Fig. 7.7 Snapshot of reference posture tracking control experiment of PATRo.

The experimental results are shown in the following figure. Fig. 7.8(a) shows the magnitude of the current consumed during tracking control, Fig. 7.8(b) is the magnitude of the trajectory tracking error, and Fig. 7.8(c) shows the change of profiles of each angular position of the nine passive revolute joints.

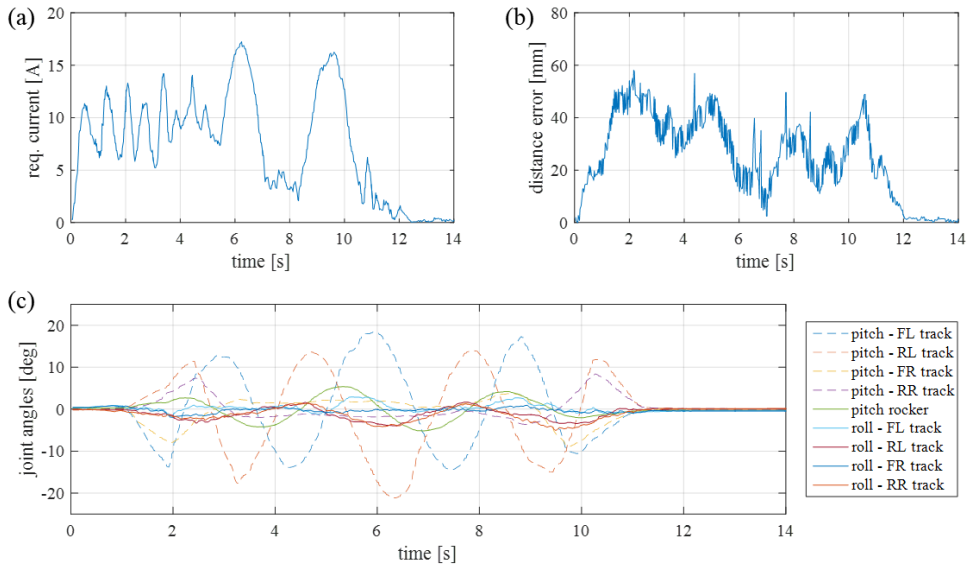


Fig. 7.8 Result of experiment: (a) terrainability, (b) maneuverability, (c) angular position of passive joints

The reproducibility of the experimental results was also confirmed. The results of three repeated experiments under the same conditions are as follows. As depicted in Fig. 7.9, it is shown that the same result is obtained in the repeated experiment.

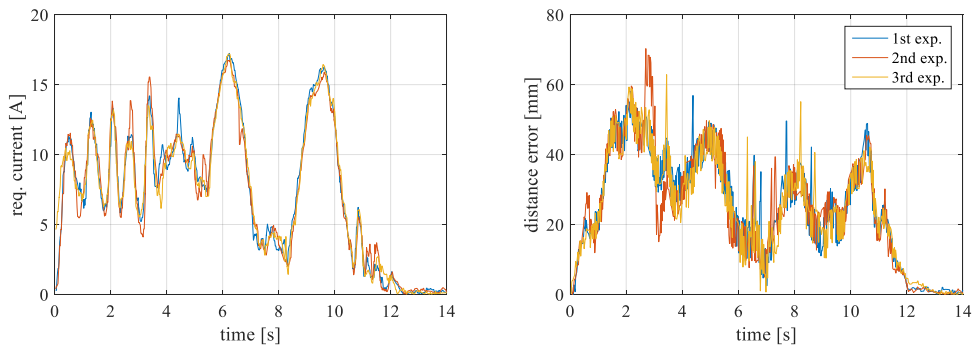


Fig. 7.9 Reproducibility of the terrainability and maneuverability

In addition, the experimental results were compared with the simulation results under the same conditions. Fig. 7.10(a) shows the terrainability in simulations and experiments, and Fig. 7.10(b) shows maneuverability results. As shown in the figure, the

tendency of the two performance indices coincide with each other, which supports the significance of the simulation results.

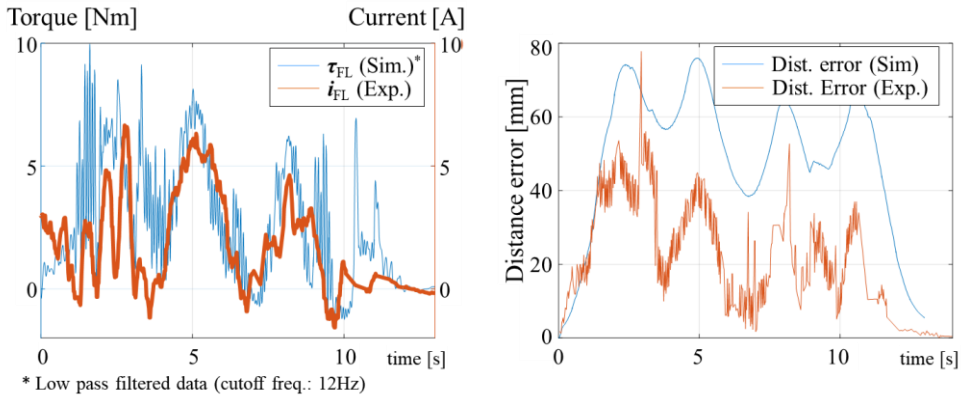


Fig. 7.10 Comparison of experimental result and simulation result in the same condition

7.2.2. Effect of passive joints: PATRo vs partially locked PATRo

Among the simulation results summarized in Section III, we compared the performance of PATRo, PATRo-A, PATRo-B, and PATRo-C. PATRo-A, B, and C are other versions of PATRo. Some of the nine passive joints that make up the PATRo's articulation structure are fixed in different ways. The performance comparison between these platforms confirms the significance of PATRo's passive joints. The difference between the four platforms is shown in the Table 7.1.

Table 7.1 Articulation structure of the four platforms

	PATRo	PATRo-A	PATRo-B	PATRo-C
Track passive DOFs	-	Locked	Locked	-
Rocker DOF	-	Locked	-	Locked
Number of passive DOFs	9	0	1	8

Fig. 7.11 and 7.12, and Table 7.2 compare the terrainability and maneuverability values of the four platforms.

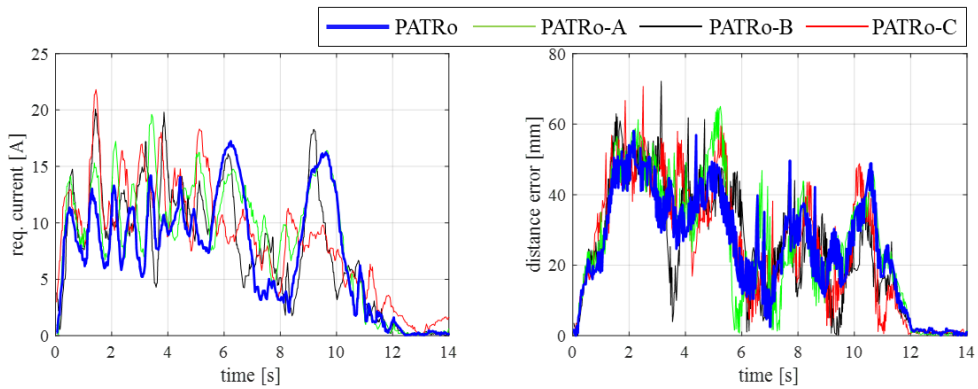


Fig. 7.11 Raw data of experiments for validation of effect of PATRo articulation

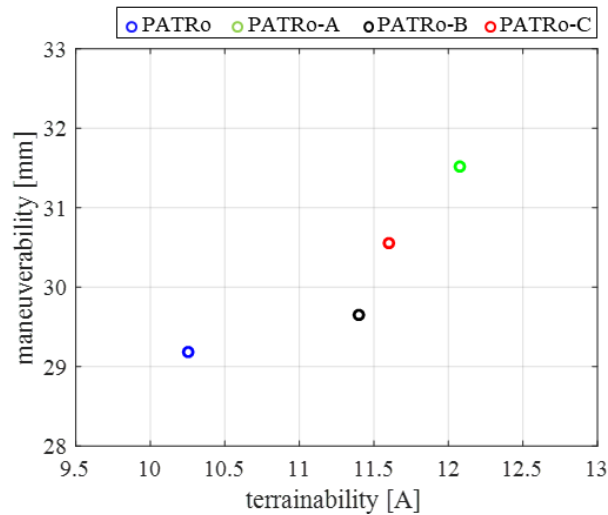


Fig. 7.12 Terrainability–maneuverability 2D plot: effect of PATRo articulation

Table 7.2 Terrainability and maneuverability values of the four platforms

	PATRo	PATRo-A	PATRo-B	PATRo-C
Terrainability [A]	10.3	11.6 (113%)	11.4 (111%)	12.1 (117%)
Maneuverability [mm]	29.2	30.5 (104%)	29.7 (102%)	31.5 (108%)

As shown in the simulation results in Section III, it can be seen that the performance of PATRo among the various platforms compared with each other is the best in terms of both terrainability and maneuverability. In addition, the performance of 8 platforms was compared in simulation, but it was difficult to make all 8 platforms, so four comparison results were not verified. However, as shown in Ch. 7.2.1, similarity between the experimental results and the simulation results is confirmed, so the remaining simulation results are also valid.

7.2.3. Effect of passive joints: applying PATRo kinematics vs applying planar kinematics

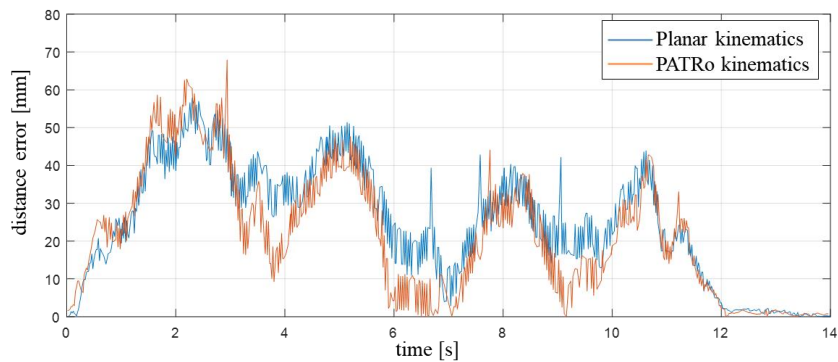


Fig. 7.13 Comparison of maneuverability: using planar kinematics vs PATRo kinematics

Fig. 7.13 compares the maneuverability results of PATRo with and without PATRo kinematics to verify the performance of the PATRo kinematics presented in Ch. 4. The maneuverability value was 29.0mm when general planar kinematics was applied, but the maneuverability value was 26.9mm when PATRo kinematics was applied. This is a 7.4% decrease, meaning that the PATRo kinematics presented in this study is valid.

7.2.4. Effect of design parameter optimization: initial design vs optimal design of PATRo

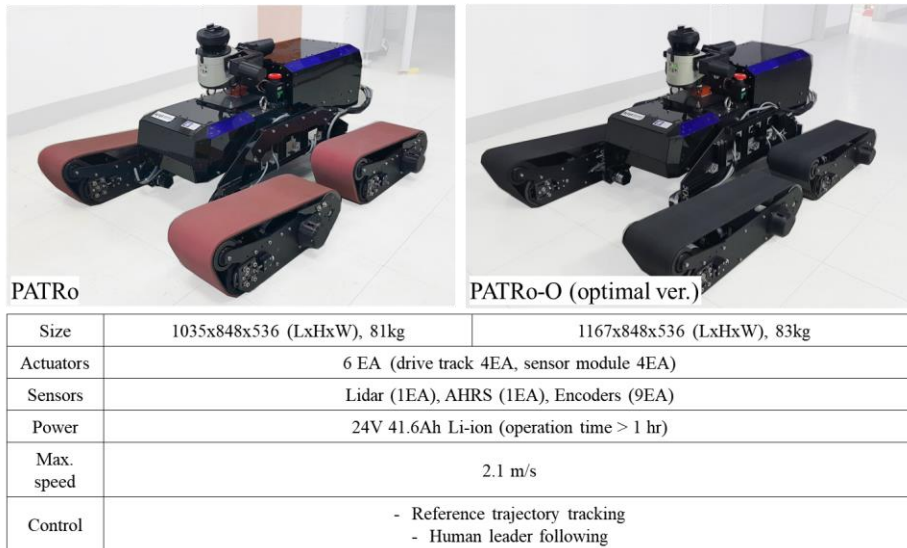


Fig. 7.14 Specification of PATRo platforms: initial design and optimal design

Fig. 7.14 shows the initial design of the PATRo and the optimal version of the PATRo (PATRo-O). PATRo-O is developed based the design parameter optimization in Ch. 5. The results of terrainability and maneuverability of PATRo and PATRo-O are compared in Fig. 7.15 and Table 7.3. Experimental results show that the terrainability and maneuverability are reduced by 10.1% and 26.8%, respectively, through kinetostatic analysis and Taguchi method.

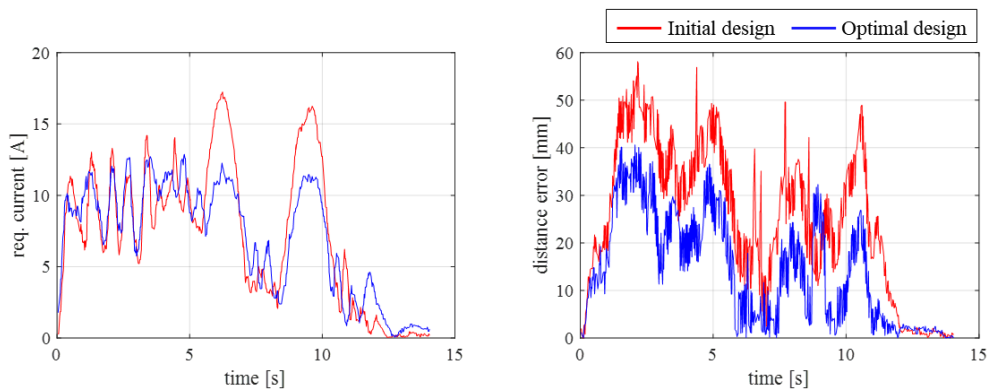


Fig. 7.15 Raw data of experiments for validation of effect of design optimization

Table 7.3 Terrainability and maneuverability values of the PATRo and PATRo-O

	Initial design	Optimal design
Terrainability [A]	10.25	9.21 (10.1% ▼)
Maneuverability [mm]	29.18	21.36 (26.8% ▼)

7.2.5. Field test on mountainous rough terrain

In order to confirm the mobility of PATRo in the actual rough terrain for the more practical aspect, field tests were performed on various terrain in mountainous terrain as shown in Fig. 7.16. During the field test, the user looked at the terrain and manually controlled the speed of the robot in jog mode. As shown in figure, there were various obstacles such as 200mm step of a large rock, a dry valley (heaps of rubbles), a ditch of 320mm width, and a ramp of about 15 degrees for climbers.



Fig. 7.16 Various rough terrain features in the experiment site

As a result, the PATRo platform was able to overcome various obstacles and ran rough terrain, which was difficult to overcome with a general track type mobile robot. Fig. 7.17 shows a snapshot of the experiment.



Fig. 7.17 PATRo overcoming various obstacles during rough terrain driving.

Chapter 8. Conclusion

A new tracked mobile robot mechanism was proposed for enhanced rough terrain driving based on the passively articulated suspension structure. The driving performances were improved in terms of terrainability and maneuverability by securing large contact area between the ground and the driving track.

The hypothesis that a large contact area leads to enhanced driving performance is verified through results of the study. According to the simulation results of performance evaluation and comparison to other mechanisms by dynamics simulation, we confirmed the structural validity of the proposed mechanism. First, the proposed 2-DOF passive joints provide a more equal load distribution to each of the four tracks, which reduced the required torque and reduced the trajectory tracking error. Second, although the 2-DOF passive joints are sufficient to ensure a full contact between the four tracks and the given terrain at each instant of discrete time, a pitch DOF in rocker links is essential to maintain the continuous full contact while running. Third, the PATRO shows better performance than the rocker-bogie and other wheeled mechanisms in terms of TA and MA, due to the improved contact condition by the passive articulation of the structure. As results, compared to the non-articulated tracked mechanism, TA and MA are reduced on average by 19.45% and 64.05%, respectively. Compared to the rocker-bogie mechanism, TA and MA are reduced on average by 39.33% and 51.93%, respectively. In the simulations, three different terrain models are applied to prevent the biased result due to the specific terrain features, and the same control algorithm is applied to all simulations to avoid the influence of control as much as possible. Simulation results are compared to the experimental results in the same condition, and the validity of the simulation results is confirmed.

Also, a mobile robot kinematics reflecting the specific articulation mechanism of PATRO. Using the instantaneous configuration of the PATRO, the platform is able to measure the

geometry of the terrain, and the posture control performance can be improved by using this information.

Design optimization of the developed mechanism was performed. The maximum required friction coefficient set as the cost function to be optimized, and the dynamics of the PATRo mechanism is analyzed via kinetostatic analysis. As a result of optimization by Taguchi method, the maximum required friction coefficient is reduced by 21.8%. The result of design optimization is validated through both dynamics simulation and experiments. Through design optimization, terrainability and maneuverability are decreased by 10.1% and 26.8% with respect to those of the initial design, respectively. Finally, the mobility test of PATRo in more real rough terrain is carried out.

Bibliography

- [1] J. Stücker, M. Schwarz, M. Schädler, A. Topalidou-Kyniazopoulou, and S. Behnke, Nimbro explorer: Semiautonomous exploration and mobile manipulation in rough terrain, *Journal of Field Robotics*, 33 (4) (2016) 411-430.
- [2] R. E. Arvidson, K. D. Iagnemma, M. Maimone, A. A. Fraeman, F. Zhou, M. C. Heverly, P. Bellutta, D. Rubin, N. T. Stein, J. P. Grotzinger, and A. R. Vasavada, Mars science laboratory curiosity rover megaripple crossings up to Sol 710 in Gale crater, *Journal of Field Robotics*, 34 (3) (2017) 495-518.
- [3] R. Gonzalez, D. Apostolopoulos, and K. Iagnemma, Slippage and immobilization detection for planetary exploration rovers via machine learning and proprioceptive sensing, *Journal of Field Robotics*, 35 (2) (2018) 231-247.
- [4] Y. Gu, N. Ohi, K. Lassak, J. Strader, L. Kogan, A. Hypes, S. Harper, B. Hu, M. Gramlich, R. Kavi, R. Watson, M. Cheng, and J. Gross, Cataglyphis: An autonomous sample return rover, *Journal of Field Robotics*, 35 (2) (2018) 248-274.
- [5] LS3 – Legged Squad Support System, <https://youtu.be/R7ezXBEBE6U> (retrieved Feb. 26, 2018)
- [6] Y. W. Park, and J. Kim, Status and technical challenges of military robots (in Korean), *Journal of Korea Robotics Society*, 12 (1) (2015) 25-33.
- [7] B. Yamauchi, PackBot: A versatile platform for military robotics, In *Unmanned Ground Vehicle Technology VI*, 5422 (2004) 228-238.
- [8] D. Choi, Y. Kim, S. Jung, H. S. Kim, and J. Kim, Improvement of step-climbing capability of a new mobile robot RHyMo via kineto-static analysis, *Mechanism and Machine Theory*, 114 (2017) 20-37.
- [9] S. Feng, E. Whitman, X. Xinjilefu, X., and C. G. Atkeson, Optimization-based full body control for the DARPA robotics challenge, *Journal of Field Robotics*, 32 (2) (2015) 293-312.
- [10] A. Kshirsagar and A. Guha, Design optimization of rocker bogie system and development of look-up table for reconfigurable wheels for a planetary rover, *International Journal of Vehicle Structures & Systems*, 8 (2) (2016) 58.
- [11] S. F. Toha and Z. Zainol, System modelling of rocker-bogie mechanism for disaster relief. *Procedia Computer Science*, 76 (2015) 243-249.
- [12] T. Thueer, P. Lamon, A. Krebs, and R. Siegwart, CRAB-Exploration rover with advanced obstacle negotiation capabilities, Swiss Federal Institute of Technology (ETHZ), Autonomous Systems Lab, (2006).
- [13] T. Thueer and R. Siegwart, Evaluation and optimization of rover locomotion performance, *ICRA, In Rome Workshop on Space Robotics*, (2007).
- [14] M. Neumann, T. Predki, L. Heckes, and P. Labenda, Snake-like, tracked, mobile robot with active flippers for urban search-and-rescue tasks, *Industrial Robot: An International Journal*, 40 (3) (2013) 246-250.
- [15] Y. Liu and G. Liu, Track-stair interaction analysis and online tipover prediction for a self-reconfigurable tracked mobile robot climbing stairs, *IEEE/ASME Transactions on Mechatronics*, 14 (5) (2009) 528-538.
- [16] Chaos, <http://www.asirobots.com/products/chaos/> (retrieved Feb. 26, 2018)
- [17] K. Ohno, S. Tadokoro, K. Nagatani, E. Koyanagi, and T. Yoshida, Trials of 3-D map construction using the tele-operated tracked vehicle Kenaf at Disaster City. In *Robotics and Automation (ICRA), 2010 IEEE International Conference on*, (2010) 2864-2870.
- [18] D. Apostolopoulos, Analytic configuration of wheeled robotic locomotion, Unpublished Ph.D. thesis, The Robotics Institute, Carnegie Mellon University, Pittsburgh, PA, (2001).
- [19] R. W. Brockett, *Robotic manipulators and the product of exponentials formula*. In *Mathematical theory of networks and systems*, Springer, Berlin, Germany, (1984).
- [20] M. G. Bekker, *Theory of land locomotion*, Ann Arbor, The University of Michigan Press, USA, (1956).
- [21] W. Li, Y. Huang, Y. Cui, S. Dong, and J. Wang, Trafficability analysis of lunar mare terrain by means of the discrete element method for wheeled rover locomotion, *Journal of Terramechanics*, 47

- (3) (2010) 161-172.
- [22] S. Chhaniyara, C. Brunskill, B. Yeomans, M. C. Matthews, C. Saaj, S. Ransom, and L. Richter, Terrain trafficability analysis and soil mechanical property identification for planetary rovers: A survey, *Journal of Terramechanics*, 49 (2) (2012) 115-128.
- [23] T. Thueer, and R. Siegwart, Mobility evaluation of wheeled all-terrain robots, *Robotics and Autonomous Systems*, 58 (5) (2010) 508-519.
- [24] A. Krebs, T. Thueer, E. Carrasco, R. Oung, and R. Siegwart, Towards torque control of the CRAB rover, In *9th International Symposium on Artificial Intelligence, Robotics and Automation in Space (iSAIRAS'08)*. Canadian Space Agency (CSA-ASC); German Aerospace Agency (DLR), ESA, the Japanese Aerospace Exploration Agency (JAXA); National Aerospace Administration (NASA), (2008)
- [25] A. Ellery, Environment–robot interaction—the basis for mobility in planetary micro-rovers, *Robotics and Autonomous Systems*, 51 (1) (2005) 29-39.
- [26] M. Tarokh and G. J. McDermott, Kinematics modeling and analyses of articulated rovers, *IEEE Transactions on Robotics*, 21 (4) (2005) 539-553.
- [27] W. Lee, S. Kang, M. Kim, and M. Park, ROBHAZ-DT3: teleoperated mobile platform with passively adaptive double-track for hazardous environment applications, In *Intelligent Robots and systems (IROS), 2004 IEEE/RSJ International Conference on*, (2004) 33-38.
- [28] Extreme Hagglands, https://youtu.be/yb9jt_du00Q (retrieved Oct. 30, 2017)
- [29] H. Komura, H. Yamada, and S. Hirose, Development of snake-like robot ACM-R8 with large and mono-tread wheel, *Advanced Robotics*, 29 (17) (2015) 1081-1094.
- [30] M. Tarokh and G. J. McDermott, Kinematics modeling and analyses of articulated rovers, *IEEE Transactions on Robotics*, 21 (4) (2005) 539-553.
- [31] Y. Kanayama, Y. Kimura, F. Miyazaki, F., and T. Noguchi, A stable tracking control method for an autonomous mobile robot, *Robotics and Automation (ICRA), 1990 IEEE International Conference on*, (1990) 384-389.
- [32] Supplementary video, <https://youtu.be/Za4MzeUZO-0> (retrieved Mar. 16, 2018)
- [33] A. Alamdari, V. Krovi, Design of articulated leg–wheel subsystem by kinetostatic optimization, *Mechanism and Machine Theory*, 100 (2016) 222-234.
- [34] A. Meghdari, H. Pishkenari, A. Gaskarimahalle, S. Mahboobi, and R. Karimi, A novel approach for optimal design of a rover mechanism, *Journal of Intelligent and Robotic Systems*, 44 (4) (2005) 291-312.
- [35] D. Kim, H. Hong, H. Kim, and J. Kim, Optimal design and kinetic analysis of a stair-climbing mobile robot with rocker-bogie mechanism, *Mechanism and Machine Theory*, 50 (2012) 90-108.
- [36] D. Choi, Y. Kim, S. Jung, H. Kim, and J. Kim, J, Improvement of step-climbing capability of a new mobile robot RHyMo via kineto-static analysis, *Mechanism and Machine Theory*, 114 (2017) 20-37.
- [37] P. Lamon, T. Thüer, R. Jordi, and R. Siegwart, Modeling and optimization of wheeled rovers, In *Proceedings of the 8th ESA Workshop on Advanced Space Technologies for Robotics and Automation (ASTRA)*, ETH Zürich, (2004)
- [38] H. Nia, S. Alemohammad, S. Bagheri, R. Khiabani, and A. Meghdari, Design, dynamic analysis and optimization of a rover for rescue operations, In *Robot Soccer World Cup* (pp. 290-300). Springer, Berlin, Heidelberg.
- [39] Xsens. MTi User Manual, Revision E., Enschede, Netherlands: 2014.
- [40] Supplementary video, https://youtu.be/U5HtuK3Q_H8 (retrieved Jul. 26, 2018)

Abstract

본 논문은 새로운 험지 주행 이동 로봇 플랫폼인 PATRo (Passively Articulated Tracked Mobile Robot)의 개발에 관한 연구이다. PATRo의 주행 메커니즘은 본체와 두 개의 라커(rocker) 링크, 네 개의 구동 트랙으로 구성되며, 좌우의 라커 링크는 차동 관절을 통해 본체에 연결되고 각 구동트랙은 2자유도 수동 관절을 통해 라커에 연결된다. 이렇게 총 9개의 자유도를 갖는 기구 메커니즘을 통해 임의의 지면 형상에서 네 개의 구동 트랙은 독립적으로 지면과의 접촉면적을 최대화하는 안정적인 자세를 취할 수 있고, 이를 통해서 얻을 수 있는 장점은 크게 두 가지이다. 첫째, 트랙-지면 간의 접지면적 확보를 통해 트랙-지면 간 불완전한 접촉으로 인한 구동력의 손실을 최소화한다. 둘째, 지형에 대한 사전 정보가 없이도 네 개의 각 구동트랙이 지면과 이루는 접촉각을 알 수 있고, 이를 통해 제한적이지만 로봇 주변의 지형을 관측할 수 있다. 그리고 이러한 주변 지형 정보는 로봇의 험지 주행 제어에 반영되어 기존 궤적 추종 성능을 향상시킬 수 있다.

따라서 PATRo는 기존의 트랙형 이동 로봇의 단점이었던 조종성(manueverability)을, 그리고 바퀴형 이동 로봇의 단점인 험지 극복 성능(terrainability)를 모두 향상시킬 수 있는 새로운 개념의 이동 로봇 플랫폼이며, 본 연구에서는 시뮬레이션과 실험을 통해 PATRo의 험지 주행 성능을 확인하였다. 먼저 3차원 동역학 시뮬레이션을 통하여, PATRo 플랫폼과 7개의 기존 험지 주행 메커니즘의 주행 성능을 비교하였다. 주행 성능 비교 시 순수하게 각 플랫폼의 기구적 특성의 영향만을 확인하기 위해 모두 동일한 제어 알고리즘을 적용하였고, 주행 환경 선정에 의한 결과의 편향을 방지하기 위해 세 개의 주행 환경에서 비교 시험을 반복하였다. 그 결과 PATRo 플랫폼은 총 8개의 주행 플랫폼 중 가장 우수한 장애물 극복 성능과 조종성을 보였으며, 7개의 타 플랫폼 대비, 전체 평균 25.5% 향상된 험지 극복 성능, 그리고 44.7% 향상된 조종성을 보이는 것을 확인하였다.

또한 PATRo 플랫폼은 험지 주행 시 주변 지형의 경사를 제한적으로 추정할 수 있다는 장점이 있다. 일반적인 평면 기구학 모델을 사용하는 경우와는 달리, PATRo는 사전 정보가 없는 임의의 지형에서도 지면 기울기를 고려하여, 최종적으로 더욱 향상된 조종성을 보일 수 있음을 시뮬레이션과 실험을 통해 검증하였다.

또한 PATRo 플랫폼의 기구부 최적화가 수행되었다. 장애물 극복 성능과 조종성을 동시에 향상시키기 위하여 최적화의 목적함수는 최대 필요 마찰계수(max. required friction coefficient)로 선정하였다. 수직행렬과 수준 평균 분석법을 이용한 설계변수 민감도 분석을 통해 최적화 설계변수로 라커의 길이와 구동트랙의 길이를 선정하였으며, 기구-정역학적 해석(kinetostatic analysis)에 기반한 최적 토크 분배(optimal torque distribution)를 통해 최적화의 과정에서 최대 필요 마찰계수 값을 계산하였다. 기구부 최적화는 다구찌 방법론(Taguchi methodology)를 통해 이루어졌으며, 설계변수 초기값과 최적값에 따라 PATRo 시제품의 라커 링크와 구동트랙은 각각 두 가지 버전으로 제작되었다.

PATRo 시제품의 험지 주행 실험을 통해 중점적으로 확인한 것은 세 가지이다. 첫째는 시뮬레이션을 통해 확인하였던, 기존 험지 주행 로봇들 대비 상대적인 우수성이다. 실험에서는, 이는 PATRo 시제품의 라커 관절, 트랙의 피치(pitch)와 롤(roll) 관절를 각각 고정하였을 때와 그렇지 않았을 때의 주행 성능을 비교함으로써 확인할 수 있었다. 둘째는 기구-정역학적 해석과 다구찌 방법론 기반의 기구부 최적화 결과의 검증이다. 실험 결과, 기구부 최적화를 통해 험지 극복 성능과 조종성이 각각 13.3%, 5.9% 향상되는 것을 확인하였다. 마지막으로 개발된 PATRo 플랫폼의 보다 실용적인 적용을 고려하여, 실제 산악 지형에서 PATRo의 험지 주행 성능 실험을 수행하였다.